Exfoliation of Non-van der Waals Materials and Investigations on the Magnetic Bistability of 2D Nanostructures on Curved Surfaces

Thesis submitted to

Cochin University of Science and Technology

in partial fulfilment of the requirements

for the award of the degree of

Doctor of Philosophy

By

Aravind P. B.

Department of Physics
Cochin University of Science and Technology
Cochin-682 022, Kerala, India

March 2019

Ph.D. Thesis

Entitled

Exfoliation of Non-van der Waals Materials and Investigations on the Magnetic Bistability of 2D Nanostructures on Curved Surfaces

Author
Aravind P. B.
Magnetics Laboratory
Department of Physics
Cochin University of Science and Technology
Cochin-682 022, Kerala, India
E-mail: aravindputhirath@gmail.com

Supervising Guide
Dr. M. R. Anantharaman
UGC BSR Professor
Magnetics Laboratory
Department of Physics
Cochin University of Science and Technology
Cochin-682 022, Kerala, India
E-mail: mraiyer@yahoo.com

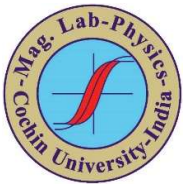

March 2019

Cover Page Illustration:

High-resolution STEM HAADF image of 'Hematene' in which oxygen atoms (**RED**) are arranged hexagonally and iron atoms (**YELLOW**) are at the octahedral voids.

Image Credits - Dr. Shyam K. Sinha & Prof. Peter A. van Aken
Stuttgart Center for Electron Microscopy, Max Planck Institute for Solid State Research, Stuttgart, Germany

DEPARTMENT OF PHYSICS
COCHIN UNIVERSITY OF SCIENCE AND TECHNOLOGY
KOCHI - 682022, INDIA

Dr. M. R. Anantharaman
UGC BSR Professor

Certificate

Certified that the thesis entitled **"Exfoliation of Non-van der Waals Materials and Investigations on the Magnetic Bistability of 2D Nanostructures on Curved Surfaces"** submitted by **Mr. Aravind P. B.** in partial fulfilment of the requirements for the award of degree of Doctor of Philosophy to Cochin University of Science and Technology, is an authentic and bonafide record of the original research work carried out by him under my supervision at the Department of Physics. Further, the results embodied in this thesis, in full or part, have never been included in any other thesis submitted previously for the award of any degree. All the modifications recommended by the Doctoral Committee during the pre-synopsis seminar have been incorporated in the thesis.

Cochin - 22
Date: 27.03.2019

Dr. M. R. Anantharaman
(Supervising Guide)

Declaration

I hereby declare that the work presented in the thesis entitled "**Exfoliation of Non-van der Waals Materials and Investigations on the Magnetic Bistability of 2D Nanostructures on Curved Surfaces**" is based on the original research work done by me under the guidance of Dr. M. R. Anantharaman, UGC BSR Professor, Department of Physics, Cochin University of Science and Technology, Cochin-682022, India, and has never been included in any other thesis submitted previously for the award of any degree.

Cochin - 22
27.03.2019

Aravind P. B.

All along my journey as a student, I have been fortunate to have associated with a lot of people who have shaped my character and sharpened my logical thinking. From classrooms to research laboratories, it has been a long voyage and constant encouragement of teachers, family and friends helped me to overcome the hurdles. They have been instrumental in inspiring my desire to learn and the courage to pursue my dreams. A few words cannot express my gratitude to them for having stood by my side during both my achievements and hardships.

First and foremost, I would like to express my deep sense of gratitude to my supervising guide Prof. M. R. Anantharaman. His guidance and advice have been pivotal in moulding me as a researcher and as an individual of values. His persistent motivation, benevolent support and professional training helped me in a great deal and took me along smoothly throughout my PhD program. He has appreciated my suggestions and boosted my confidence to take up challenging tasks. In all my walks through the dark pathways of self-doubts and uncertainties, he has been the torchbearer. I oblige him profusely with the realization that no words can properly express my gratitude.

I consider myself fortunate to have got an opportunity to work with Prof. Pulickel M. Ajayan, Benjamin M. and Mary Greenwood Anderson Professor of Engineering and Chair of Department of Materials Science and NanoEngineering (MSNE), Rice University, Houston, Texas, USA. I have been fascinated by his vision, depth of knowledge and polite behaviour. I always enjoyed the time I spent with him and the discussions we had during our trips together is something I would be again looking forward to. I acknowledge with gratitude the cooperation extended to me by Dr. Robert Vajtai, Dr. Chandrasekhar Tiwary, Dr. Sruthi Radhakrishnan, Dr. Vidya Kochat, Amey Apte and other co-workers of MSNE allowing me to carry out productive research during a short period of time.

I am extremely thankful to Prof. Junaid M. Bushiri, current Head of the Department, Prof. B. Pradeep and Prof. S. Jayalekshmi, former Heads of the Department of Physics, CUSAT for providing all the necessary facilities and appropriate environment to carry out research with ease. I take this opportunity to thank Dr. Senoy Thomas, my doctoral committee member and all the faculty members of the Department of Physics especially Prof. M. Sabir, Prof. Ramesh

Babu T., Prof. K. P. Vijayakumar, Prof. C. Sudha Kartha, Prof. (Late) V. C. Kuriakose, Prof. Godfrey Luis, Prof. M. K. Jayaraj and Prof. Titus K. Mathew for their encouragement and timely advice.

I convey my sincere thanks to the employees of office, library and laboratory of the Physics Department and administrative office for their help and assistance.

It gives me great pleasure to express my sincere gratitude towards other collaborators – Prof. Oomman Varghese, Dr. Manmadha Rao, Ram Neupane and Maggi Poulose of Department of Physics, University of Houston, Texas, USA; Dr. Cristiano F. Woellner and Prof. Douglas S. Galvao of University of Campinas, Brazil; Dr. Shyam K Sinha and Prof. Peter A. van Aken of Stuttgart Center for Electron Microscopy, Max Planck Institute for Solid State Research, Stuttgart, Germany; Dr. Liangzi Deng and Prof. Ching-Wu Chu of Texas Center for Superconductivity, University of Houston, Houston, Texas, USA; Dr. Gelu Costin of Department of Earth, Environmental and Planetary Sciences, Rice University, Houston, Texas, USA; Carlos de los Reyes and Prof. Angel A. Martí of Department of Chemistry, Rice University, Houston, Texas, USA; Dr. Avetik R. Harutyunyan of Honda Research Institute USA Inc., Columbus, Ohio, USA; Ritesh Kumar and Dr. Abhishek K. Singh of Materials Research Centre, Indian Institute of Science, Bangalore, India for their immense support at various stages of my work.

I would like to extend thanks to Prof. Manfred Albrecht, Chair of Experimental Physics IV, Institute of Physics, University of Augsburg, Germany and his group especially Michael Heigl, Felix Timmermann, Mario Fix for their immense support while I was at University of Augsburg on exchange visit under DST-DAAD PPP collaborative research project.

Special thanks are due to Dr. M. P. Vasudevan Nambudiry, Dr. Sudeep P. M., Dr. Hysen Thomas, Dr. Geetha P, Dr. Sethulakshmi N, Dr. Lija K. Joy, Dr. Lisha Raghavan, Mrs. Vinayasree S., Mr. Sivaraj K. S., Mr. Sreeram P. R., Mrs. Archana V. N., Mr. Thoufeeq S., Miss. Anjitha Biju, Miss. Navya Joseph, Miss. Anija Mary, Mr. Shan Abraham Sam and all the alumni of Magnetics Laboratory especially Dr. K. A. Malini, Dr. Swapna S. Nair, Dr. Veena Gopalan E., Dr. T. N. Narayanan and Dr. Reena Mary A. P. who have made the research atmosphere of the Magnetics Laboratory fruitful and splendid. Their affection, support and encouragement have made my research life very happy and comfortable.

And I am pretty sure that I won't ever forget all the special people who made my six years at CUSAT pleasant and cheerful. Navaneeth, Manoj, Sreejith, Aswathy, Anshad, Titu and many others. I thank them all for all the nice time I had especially interesting discussions, trips, dinner night outs, parties and games. I would also like to thank my dear friends Shanas, Rohith, Harikrishnan, Navaneeth, Smitha, Raiju, Jubeesh and Prasad for their constant encouragement and love. Special thanks to my teacher Ambily Krishnan, Govt. Victoria College Palakkad and her family for their affection.

The financial assistance provided by the University Grants Commission (UGC), Govt. of India in the form of BSR Fellowship and by the Department of Science and Technology (DST) – Nanomission in the form of project assistant fellowship are gratefully acknowledged. I would also like to acknowledge Department of Science and Technology (DST), Govt. of India for financial assistance in the form of DST-DAAD exchange visitor financial assistance as the part of DST-DAAD PPP collaborative project.

Words fail to express my love, respect and eternal gratitude to my family – Sarasu, Balan, Anand, Nithya, Arathi and Rajesh for their unconditional support. A doctorate would have been a distant dream without their immense motivation support and care.

And Arya, thanks for being a bliss in my life.

I bow in reverence before the Almighty for everything…

Aravind

"We are kept from our goal not by obstacles but by a clear path to a lesser goal."

~ Bhagavat Gita

Preface

With the advent of nanotechnology, graphene occupies an important position in the realm of carbon nanostructures along with one-dimensional carbon nanotubes and zero-dimensional buckyballs. The successful exfoliation of a monolayer of graphene from graphite by Andre Geim and Konstantin Novoselov is widely considered to be a milestone as far as two-dimensional (2D) materials are concerned. This discovery has opened up the floodgates of research on many other 2D materials. A monolayer of graphene exhibits superlative physical and chemical properties as compared to its bulk counterpart graphite. From a fundamental perspective, the conduction in graphene is due to the ballistic transport of charge carriers which attains a velocity of almost 10^6 ms^{-1} which is often referred to as Fermi velocity. The charge carriers which give rise to conduction originates from the unique sp^2 hybridization in graphene. The charge carriers resemble Dirac's fermions obeying Dirac's equation. The tight binding approach of which predicts a semi-metallic behaviour with a tiny overlap between valence and conduction bands for graphene. Graphene exhibits ambipolar electric field effect meaning both electrons and holes of very high density could be mobilized by applying a small gate voltage. Graphene also serves as an ideal template for experimental validation of several quantum mechanical phenomena such as anomalous quantum Hall effect (AQHE) and conduction without charge carriers.

Though techniques like functionalization are often exploited to enhance the employability of graphene in device applications but with limited success. The inability of opening up the bandgap in graphene necessitated scientists and engineers to scout for new alternatives. This has resulted in the exploration of a variety of other layered (van der Waals) materials and their successful exfoliation to their 2D counterparts. New and novel 2D materials namely silicene, germanene and stanene were grown on suitable substrates which resemble graphene in many aspects. Further, more 2D materials like 2D hexagonal boron nitride (h-BN), transition metal dichalcogenides (TMDs), phosphorene were successfully exfoliated from their bulk layered precursors and also grown on suitable substrates. Thus a new class of materials called 'van der Waals (vdW) solids' was born. A monolayer of h-BN is an insulator with a bandgap of around 5.2 eV while a monolayer of MoS_2 belonging to TMDs has a bandgap of 1.9 eV. 2D

MoS_2 is a direct bandgap semiconductor whereas its parent form is an indirect bandgap material. Moreover, extracting monolayers from their layered bulk counterparts was considered to be easier due to the very weak interlayer van der Waals bonding and hence energetically favourable to exfoliate.

A thorough survey of literature reveals that the extraction of a 2D material from non-layered (non-van der Waals) bulk precursors have met with limited success. The idea of extracting 2D layers from non-layered materials is a novel concept and successful exfoliation by simple techniques like liquid phase exfoliation augurs well for that purpose. This is primarily because it will be a proof of concept experiment to understand the mechanism of exfoliation from a fundamental perspective and will lead to new and novel 2D materials for various applications. Naturally occurring ores are ideal starting materials for exfoliation. Thus extracting new and novel 2D materials from non-layered naturally occurring oxides, as well as tellurides, is one of the motives of this investigation.

Extraction of a monolayer or few layers from non-layered bulk precursors involves identification of preferentially exposed monolayers which are energetically favourable for exfoliation. Their thermal stability is also of prime importance. A prediction of a prospective non-layered material or for that matter, a validation after successful exfoliation needs theoretical backing. In this context, techniques like molecular dynamics and phonon dispersion become very useful. So it will be our endeavour to employ molecular dynamics and phonon dispersion to predict the preferential exfoliation of atomic planes. This is yet another motive for the present study.

2D magnetism is a hot area of research which is evident from the importance that is devoted to this research by leading journals like Nature and Science. Though research in 2D magnetism is in its infancy, great importance is being attached to this area recently. This is because a vdW bulk material which normally exhibits ferro(ferri)magnetism is not expected to retain its magnetic groundstate down to monolayers as per the implications of Mermin-Wagner theorem. However, recent theoretical and experimental investigations on certain vdW 2D materials are on the contrary. Thus it was thought that exfoliation of a monolayer/few layers and studying the magnetic ordering in such low dimensional systems by

using these templates will be a good proposition from a fundamental perspective. For this, inherently non-layered precursors namely hematite and ilmenite are considered ideal templates because they are having hexagonal crystal symmetry and exhibit antiferromagnetic ordering. These resulting 2D systems after exfoliation will be christened 'Hematene' and 'Ilmenene' akin to graphene or phosphorene. The only difference being the former is from non-layered oxide precursors while the latter is from layered materials. Probing the magnetic ordering in these 2D systems of hematene and ilmenene both experimentally and theoretically by employing density functional theory (DFT) is yet another objective of the present study. Magnetism in 2D systems, in general, is also interesting from an application point of view since they are candidate materials for low-power spintronic applications.

Photocatalytic splitting of water without an applied voltage is promising. Low dimensional materials have the added advantage of modification of optical bandgaps because of the quantum confinement effects. As far as the choice of electrode materials for water splitting goes, energy bandgaps and band edge positions are decisive. Making a 2D monolayer is nothing but bandgap and band edge engineering. A 2D hematene or ilmenene is expected to enhance the bandwidth for absorption and improve the overall performance when employed as a standalone electrode or as a heterojunction formed with a titania nanotube array electrode. When these 2D materials are used in combination with titania nanotubes, it is expected that the carrier injection into the titania will be augmented while reducing the recombination. Moreover, forming a heterojunction of hematene/ilmenene with titania (TiO_2) nanotube array electrodes is expected to enhance the overall quantum efficiency by sensitizing the ultraviolet active titania in the visible region of the solar spectrum. Testing and evaluating the efficiency of hematene and ilmenene for photocatalytic hydrogen generation is yet another motive of the present study.

Magnetic vortices are increasingly being investigated by scientists the world over because of its potential applications in memory devices, spin wave generators and quantum information processing. Magnetic vortices are spiral kind of magnetic entities observed in ferromagnetic dots and rectangular patterns of micron or sub-micron size. In such patterns with circular or rectangular geometries, domain formation is not energetically favourable. When the thickness becomes much smaller than the diameter

of these patterns, all the magnetic moments/spins tend to orient in the plane, gradually changing direction so as to nullify dipole energy and to reduce the expense of exchange energy. The angle between adjacent spins becomes increasingly larger such that at the centre known as vortex core, the magnetization will point out of the plane. Magnetic vortices can be generated in 2D nanostructures of certain soft magnetic alloys like FeNi, FePd and FePt. From an application point of view, understanding the dynamics of the vortex core in an external field is of utmost importance. The M-H curve of magnetic vortices is characterized by two characteristic fields known as annihilation (Ha) and nucleation (Hn) fields at which the magnetic vortex switches into a single domain state and vice versa. These switching fields are functions of magnetization (M) as well as temperature (T). One can suitably optimize these parameters such that Ha and Hn coincide and results in a loss-less switching between vortex and collinear states. The particular temperature at which this loss-less switching occurs is known as bifurcation temperature (T_e). Generally, soft magnetic alloys are preferred considering the minimization of magnetocrystalline anisotropy energy. Fe_xPd_{1-x} is proved to be an ideal system wherein it is possible to vary the bifurcation temperature with Fe composition, x. For this Fe_xPd_{100-x} 2D nanocaps will be deposited on curved polystyrene surfaces for various concentrations of 'x'. A detailed investigation of such systems with regard to tailoring the bifurcation temperature (T_e) also forms part of the present thesis.

Probing magnetism using conventional methods such as vibrating sample magnetometry (VSM), SQUID magnetometry at low dimensions has met with only limited success and interpretation of results often become speculative since these measurements are meant for bulk specimens. Study of surface magnetism, especially in 2D systems like 2D materials and thin films, requires sophisticated measurement techniques like scanning nitrogen vacancy (NV) magnetometers and fluorescence based techniques. Measurements based on the magneto-optic Kerr effect (MOKE) is also ideal to investigate the surface magnetism as it is sensitive even to a single atomic layer of materials. Magneto-optic Kerr effect is the rotation of the polarization of a linearly polarized light (laser) upon reflection from a magnetized surface and the magnitude of rotation is proportional to the magnetization of the surface. Limited availability of surface sensitive measurement facilities such as scanning NV magnetometer has motivated us to fabricate a complete magnetic

measurement set up based on magneto-optic Kerr effect (MOKE Set up) indigenously with provision for measurement at cryogenic temperatures. Automation and data acquisition is being performed using National Instruments LabVIEW graphical user interface (GUI). This is another objective of the present investigation.

Thus the objectives of the present investigations can be summarized as follows.

1. Exfoliation of a 2D material from a non-layered naturally occurring iron ore hematite for the first time and investigations on the magnetic and photocatalytic water-splitting properties.
2. Extracting yet another novel 2D material from a non-layered naturally occurring titania ore ilmenite and to study the magnetic properties as well as photocatalytic hydrogen evolution.
3. To exfoliate a 2D material from non-layered bulk precursor manganese telluride (MnTe) and to investigate the change in magnetic properties due to exfoliation.
4. Creation of magnetic vortices on 2D nanocaps of soft magnetic alloy of the form Fe_xPd_{100-x} on curved surfaces of polystyrene and to tune the bifurcation temperature (Te) of magnetic vortices with varying x, being the Fe concentration.
5. To fabricate an in-house fully automated magneto-optic Kerr effect (MOKE) set up for the investigation of surface magnetism and to check the validity of the initial measurements using the Stoner-Wohlfarth model.

The thesis is entitled **"Exfoliation of Non-van der Waals Materials and Investigations on the Magnetic Bistability of 2D Nanostructures on Curved Surfaces"** and is divided into eight chapters.

The first chapter provides a general introduction to 2D materials with special emphasis to graphene and the emerging regime of van der Waals solids. A general introduction to magnetism, photocatalytic water splitting, magnetic vortices and magneto-optic Kerr effect is also provided in this chapter.

Chapter two is the experimental chapter which discusses the various experimental techniques employed for synthesis as well as characterization of prepared samples in this investigation.

The third chapter is on the exfoliation of a 2D material 'hematene' from a non-layered naturally occurring iron ore hematite and investigations on the magnetism exhibited by these 2D nanostructures. Hematene as a candidate material for studying ferromagnetic ordering is also dealt with in this chapter. The photocatalytic water splitting employing hematene is described as well in this chapter.

The fourth chapter is on the exfoliation of another 2D material 'Ilmenene' from a naturally occurring non-layered titania ore ilmenite. Investigation of its magnetism and demonstration of photocatalytic water splitting by forming a heterojunction of ilmenene with titania nanotube array electrodes form part of this chapter.

The fifth chapter deals with the exfoliation of yet another 2D material from manganese (II) telluride (MnTe) and investigations on the magnetic properties.

The sixth chapter describes the fabrication of magnetic vortices on cap like 2D nanostructures of soft magnetic alloys of the form Fe_xPd_{100-x} where x = 13, 15, 17 and 20, on closely packed hemispherical polystyrene structures by employing co-sputtering technique. The tuning of bifurcation temperature (T_e) in this system by compositional variance is mainly dealt with in this chapter along with magnetic properties.

Chapter seven is about the fabrication of a magneto-optic Kerr effect magnetometer, its description, automation, calibration and validation of the performance using the Stoner-Wohlfarth model.

Chapter eight contains the general conclusions drawn from these investigations and future prospects.

Publications

In Peer Reviewed Journals

1. ***Puthirath Balan, A.***; Radhakrishnan, S.; Woellner, C. F.; Sinha, S. K.; Deng, L.; Reyes, C. d. l.; Rao, B. M.; Paulose, M.; Neupane, R.; Apte, A.; Kochat, V.; Vajtai, R.; Harutyunyan, A. R.; Chu, C.-W.; Costin, G.; Galvao, D. S.; Martí, A. A.; van Aken, P. A.; Varghese, O. K.; Tiwary, C. S.; Malie Madom Ramaswamy Iyer, A.; Ajayan, P. M., Exfoliation of a non-van der Waals material from iron ore hematite. *Nature Nanotechnology* **2018,** *13* (7), 602-609.
2. ***Puthirath Balan, A.***; Radhakrishnan, S.; Kumar, R.; Neupane, R.; Sinha, S. K.; Deng, L.; de los Reyes, C. A.; Apte, A.; Rao, B. M.; Paulose, M.; Vajtai, R.; Chu, C. W.; Costin, G.; Martí, A. A.; Varghese, O. K.; Singh, A. K.; Tiwary, C. S.; Anantharaman, M. R.; Ajayan, P. M., A Non-van der Waals Two-Dimensional Material from Natural Titanium Mineral Ore Ilmenite. *ACS Chemistry of Materials* **2018,** *30* (17), 5923-5931.
3. ***Puthirath Balan, A.***; Radhakrishnan, S.; Neupane, R.; Yazdi, S.; Deng, L.; A. de los Reyes, C.; Apte, A.; B. Puthirath, A.; Rao, B. M.; Paulose, M.; Vajtai, R.; Chu, C.-W.; Martí, A. A.; Varghese, O. K.; Tiwary, C. S.; Anantharaman, M. R.; Ajayan, P. M., Magnetic Properties and Photocatalytic Applications of 2D Sheets of Nonlayered Manganese Telluride by Liquid Exfoliation. *ACS Applied Nano Materials* **2018,** *1* (11), 6427-6434.
4. ***Aravind, P. B***.; Heigl, M.; Fix, M.; Groß, F.; Gräfe, J.; Mary, A.; Rajgowrav, C. R.; Krupiński, M.; Marszałek, M.; Thomas, S.; Anantharaman, M. R.; Albrecht, M., Bistability of magnetic states in Fe-Pd nanocap arrays. *Nanotechnology* **2019**, 30 (40), 405705.
5. B. Puthirath, A.; Patra, S.; Pal, S.; Muralidharan, M.; ***Puthirath Balan, A.***; S, J.; Tharangattu N, N., Transparent flexible lithium ion conducting solid polymer electrolyte. *Journal of Materials Chemistry A* **2017,** *5* (22), 11152-11162.
6. Lisha, R.; Hysen, T.; Geetha, P.; ***Aravind, P. B.***; Shareef, M.; Shamlath, A.; Ojha, S.; Ramanujan, R. V.; Anantharaman, M. R., Defect induced enhancement of exchange bias by swift heavy ion irradiation in zinc ferrite-FeNiMoB alloy based bilayer films. *Nuclear Instruments & Methods in Physics Research Section B-Beam Interactions with Materials and Atoms* **2015,** *360*, 68-74.
7. Narayanan, S. P.; Thakur, P.; ***Balan, A. P.***; Abraham, A. A.; Mathew, F.; Yeddala, M.; Subair, T.; Tiwary, C.; Thomas, S.; Narayanan, T. N.; Ajayan, P. M.; Anantharaman, M. R., Two-Dimensional Amorphous Cr_2O_3 Modified Metallic Electrodes for Hydrogen Evolution Reaction. *physica status solidi (RRL) – Rapid Research Letters* **2019,** *0* (0), 1900025.

Conference Proceedings

1. (2015). "Exchange bias in zinc ferrite-FeNiMoB based metallic glass composite thin films." AIP Conference Proceedings **1665**(1): 130045.
2. (2015). "Tailoring growth conditions for efficient tuning of band edge of CdS nanoparticles." AIP Conference Proceedings **1665**(1): 050128.
3. (2015). "Synthesis of coaxial CoFe2O4 - K0.5Na0.5NbO3 nanotubes by sol-gel technique using inexpensive templates." AIP Conference Proceedings **1665**(1): 140048.
4. (2015). "Structural, morphological and optical properties of chromium oxide nanoparticles." AIP Conference Proceedings **1665**(1): 050148.
5. (2016). “Surface and Bulk Magnetization in Fe thin films: A comparative study.” Fourth International Conference on Frontiers in Nanoscience and Technology (COCHIN NANO 2016).
6. (2018). “Hysteresis free switching between collinear and vortex states in closely packed FePd cap arrays” The Joint European Magnetic Symposia (JEMS 2018)
7. (2018). “ Hematene –A new non-van der Waals 2D material” MRS Fall Meeting and Exhibit 2018.

Contents

Chapter 1

Introduction

This chapter provides a brief introduction to two-dimensional materials in general with emphasis on 2D magnetism, photocatalysis together with the motivation of the present study.

The advent of nanotechnology is considered to be a harbinger for all developments in the realm of science and technology making life more humane and contributing to the removal of obsolescence. Nanotechnology is a game changer and is a common denominator of all other emerging technologies of the 21st century, namely, biotechnology, information technology, biomedical and photonics. Any incremental advances made in the regime of nanotechnology is bound to impact all other areas of science and technology.

It is well known that size matters a lot in nanotechnology and as we reduce size or dimensionalities, materials exhibit superlative properties with respect to their micron-sized bulk counterparts.[1] Most of the phenomena at reduced dimensions have been explained by quantum mechanics. Mostly, modifications in the physical and chemical properties are attributed to quantum confinement of electrons/phonons or excitons. Quantum confinement with respect to the orthogonal axes XYZ gives us the possibility of 3D, 2D, 1D and 0D nanostructures.

Carbon nanostructures[2] have been one of the first and foremost in the area of nanotechnology and in that C60: Buckminsterfullerenes[3] is considered to be the first sibling. Then came carbon nanotubes (CNTs)[4] and graphene.[5] The successful exfoliation of graphene[6] by Andre Geim and Konstantin Novoselov is an important discovery which has paved way for new two-dimensional materials namely hexagonal boron nitride (hBN)[7], transition metal dichalcogenides (TMDs)[8], silicene, germanene[9], phosphorene[10], 2D layered transition metal oxides[11], and hydroxides.[12] One characteristic feature of these 2D materials is that their bulk

counterparts are mostly layered and it is easy to extract a monolayer or few layers by mechanical means. However, extracting a monolayer or few layers from non-layered precursors is not seen attempted by many and is a new area by itself in the regime of 2D materials.[13]

Magnetism is a cooperative phenomenon and the origin is quantum mechanical in nature.[14] The magnetic industry is as big as the electronic industry or has overgrown other industries! Very recently new magnetic phenomena like giant magnetoresistance (GMR)[15], colossal magnetoresistance (CMR)[16] and tunnelling magnetoresistance (TMR)[17] have been discovered which has given birth to a new area of spin-based electronics widely known as 'spintronics'.[18] Of late scientists and engineers are focusing on 2D materials which exhibits considerable ferromagnetic ordering.[19] Thus 2D magnetism is an emerging area of research and is expected to impact both the storage industry as well as the area of spintronics. However, 2D magnetism is still in its infancy and needs to be understood more from a fundamental perspective.

Many oxidic non-layered materials like hematite and ilmenite are antiferromagnetic in their bulk and also serve as good photocatalyst materials for water splitting applications. It is anticipated that a monolayer or few layers of these materials could be an ideal template for studying 2D magnetism. Moreover, quantum confinement in the 2D regime leads to modification of optical bandgap and band edges and could be useful materials for water splitting.

Magnetic vortices[20] is a new area of research and are being hotly pursued the world over. Creation of a stable vortex at room temperature could be a game changer in the area of spintronics.

Magnetism at two-dimension is often explored by using scanning nitrogen vacancy magnetometer or by employing fluorescence based techniques and are having limited access. SQUID magnetometer is widely used to study the magnetic properties of a specimen, however, is a bulk characterization techniques and is not sensitive to a local area or to the surface (< 20 nm) of the specimen. Thus, it is felt that surface magnetism or magnetism at two-dimensions can be studied by using simple techniques like magneto-optic Kerr effect magnetometers[21] in which a polarized laser beam is used for probing magnetism of the specimen.

This thesis takes a look at the possibilities of extraction of 2D materials from their non-layered bulk precursors hematite, ilmenite, and manganese telluride. The resulting magnetic ordering is studied with a view to employing it for applications. Generation of hydrogen employing these materials via photocatalysis is probed. The latter part of the thesis describes the investigation on the bifurcation temperature of magnetic vortices and fabrication of a table-top magneto-optic Kerr effect magnetometer for studying surface magnetism.

The subsequent sections in this chapter will discuss fundamental aspects of 2D materials, magnetism, photocatalytic water splitting, and motivation of the present study.

1.1 Introduction to 2D Materials

The extraction of an atomic layer of graphite by mechanical means has been a trendsetter as far as research in two dimensional (2D) materials are concerned.[5] To date, most of the research on 2D materials addresses the fundamental properties rather than applications. Efforts are on to fulfil the promises and expectations of society. The popularity of this research area is due to the relative ease with which high purity samples can be obtained by means of mechanical exfoliation.[6] A trained experimentalist and small quantity of bulk precursors will be good enough to exfoliate its 2D counterparts.

A major class of materials called inorganic graphene analogues (IGAs) made its foray into the family of 'graphene and beyond'.[22] They include Transition Metal Dichalcogenides (TMDs)[23], Boron Nitrides (BN)[7] and Transition Metal Oxides.[11] Among them, MoS_2 is the most explored material owing to its excellent properties and applications in diverse fields such as nanophotonics and optoelectronics.[8, 24] Other TMDs such as WS_2, $MoSe_2$, $MoTe_2$, $TaSe_2$, $NbSe_2$, and $NiTe_2$ are also increasingly becoming popular due to their MoS_2 like structure and morphology.[25] These materials were already demonstrated to have excellent properties comparable to that of MoS_2. Unlike semiconducting or metallic TMDs, Boron Nitride (BN) is an insulator and its structure is analogous to graphene.

2D metal oxides are an important sub-class of the IGAs. They exhibit exceptional electronic and optical properties and are due to strongly correlated d electrons of the metallic cations.[26] Their properties are

tunable with ease owing to their diversity in chemical compositions, crystal structure, and oxygen defects. Some of the important 2D metal oxides are MoO_3, WO_3, Ga_2O_3, and V_2O_5 which are naturally occurring as layered materials in bulk form. Their respective 2D analogues can be exfoliated from these naturally occurring layered crystals using liquid or gas phase techniques. Layered perovskite oxides are also good precursors for extracting 2D metal oxides and could be building blocks for high-κ-dielectrics.[27]

1.2 Graphene and Graphene Derivatives

The discovery of Graphene in 2004 by Geim and Novoselov laid the foundation for extensive research in 2D materials and beyond, and lead to their eventual applications ranging from electronics to medicine. Graphene, a monolayer of carbon atoms packed into a honeycomb lattice (***Figure 1.1***), is found to be exhibiting exotic properties in comparison to conventional nano-systems.[28]

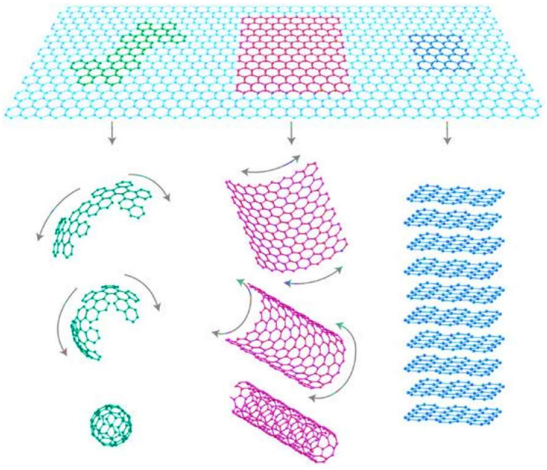

Figure 1.1 The fundamental building block. Graphene is the fundamental building block for other carbon materials like 1D carbon nanotubes (CNTs) and 0D buckyballs (Adapted from *Nature Materials volume 6, pages 183–191 (2007)*)[5]

The charge carriers in graphene behave like relativistic particles with zero rest mass, obeying massless Dirac equation. The electron energy

dispersion in a honeycomb lattice of graphene is shown in ***Figure 1.2***. The governing equation employing the tight binding approach (Hamiltonian) is (equation 1.1.) given by,

$$E_{\pm}(\boldsymbol{k}) = \pm t\sqrt{3 + f(\boldsymbol{k})} - t' f(\boldsymbol{k}) \qquad (1.1)$$

where t is the nearest neighbour electron hopping energy and t' is the next nearest neighbour hopping energy. An immediate consequence of massless Dirac fermions is the cyclotron mass m* that varies as the square root of electronic density (n) (refer equation 1.2). The estimated value of Fermi velocity is $v_F \approx 10^6 \text{ms}^{-1}$.

$$m^* = \frac{\sqrt{\pi}}{v_F}\sqrt{n} \qquad (1.2)$$

Graphene's conductivity never falls below G_0, the quantum unit of conductance, even if it has zero concentration of charge carriers. It also exhibits anomalous quantum Hall effect. The mass of Dirac fermions in graphene m^* is given by $E = m^* {v_F}^2$. All these fundamental aspects can be understood within the principles of quantum electrodynamics.[29]

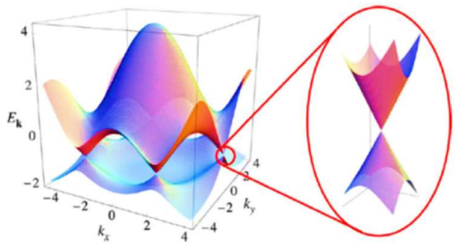

Figure 1.2: Dirac cones in graphene. The electron dispersion in a graphene honeycomb lattice (left-hand side) and a zoomed in image of a Dirac point on the right. (Adapted from *Rev. Mod. Phys., Vol. 81, No. 1, January–March 2009*)[28]

Graphene is an exciting material having large theoretical specific area, high intrinsic mobility, high electrical and thermal conductivity and high transmittance which enables it to be suitable for various applications.[30-34]

The possibility of functionalization or modification of graphene opens up new avenues in research related to graphene derivatives.[35] It must be noted that Graphite Oxide is the best precursor material for large scale synthesis of Chemically Modified Graphene (CMG) and other graphene derivatives.[36]

1.3 Graphite Oxide and Graphene Oxide (GO)

Chemically modified graphene possesses excellent electrical, mechanical and thermal properties. They find applications in polymer composites, energy-related materials, field-effect transistors (FET), and biomedical applications. Graphene Oxide (GO) can be derived from Graphite Oxide and its chemical modification has been a promising route to achieve mass production of chemically modified graphene platelets. GO consists of a number of reactive oxygen functional groups, which makes it a suitable material for various applications mentioned above.[37]

Graphite Oxide and GO are electrically insulating due to their disrupted sp^2 hybridized molecular bonding network. A widely accepted method to induce conductivity is by restoring the π-bonding network through the reduction of GO. The resultant product is termed 'reduced graphene oxide' (rGO). GO and graphite oxide looks similar but not structurally identical. ***Figure 1.3*** shows the Lerf-Klinowski model of GO structure.[38]

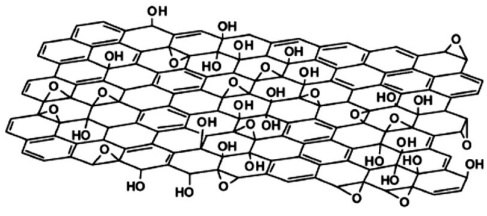

Figure 1.3. Structural model of GO: The Lerf-Klinowski model of GO. (Adapted from *Chemical Physics Letters 287 1998 53–56*)[38]

Graphite oxide can be exfoliated to obtain stacked few layers or monolayer GO sheets. Liquid phase exfoliation (stirring and/or sonicating) is the most reliable method to obtain GO from graphite oxide. Exfoliation followed by reduction by means of chemical, thermal or electrochemical methods results in rGO sheets which resemble pristine graphene to varying extents (some resemble very closely), especially in terms of their physical properties, as well as surface morphology. GO and graphite oxides can be functionalized using various chemical reactions to obtain chemically modified graphene. The ease at which we could add functionalities to the already existing groups in GO/graphite oxide makes them versatile precursor materials for various applications.

1.4 Inorganic Graphene Analogues (IGA)

Pristine graphene has no bandgap (Eg) which limits its applications in electronic logic devices and optoelectronics. In this context, new 2D layered materials such as metal chalcogenides, transition metal oxides, and other 2D compounds have attained renewed interest and are collectively known as inorganic graphene analogues (IGAs).[39]

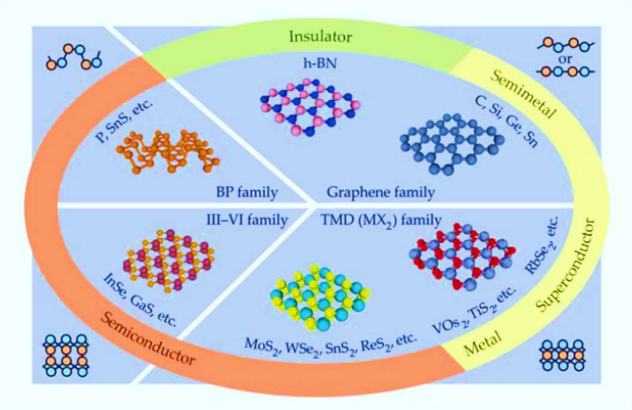

Figure 1.4: The world of 2D materials together span the entire electronic properties: Graphene and other inorganic graphene analogues (IGAs) are shown which are categorized based on electronic bandgaps. (Adapted from *Physics Today 69(9), 38 (2016)*)[40]

Transition metal dichalcogenides (TMDs) consists of hexagonal arrays of metal atoms (M) sandwiched between two layers of chalcogen atoms (X) having MX_2 stoichiometry.[41] There are more than 40 varieties of TMDs depending upon the combination of metal atoms (Mo, W, Nb, Re, Ni, or V) and chalcogen atoms (S, Se, or Te). Other important classes of materials are layered metal oxides MoO_3, and La_2CuO_4, insulator hexagonal boron nitride (h-BN) and topological insulators such as Bi_2Te_3, Sb_2Se_3, and Bi_2Se_3. Such materials span the entire range of electronic bandgap, from insulators to superconductors (see ***Figure 1.4***), and exhibits interesting properties. Silicene and germanene, the silicon- or germanium-based counterparts of graphene are also excellent 2D materials having electronic properties analogous to graphene.

1.4.1 Hexagonal Boron Nitrides

Hexagonal boron nitride (h-BN) is a wide bandgap semiconductor with exceptional physical properties and chemical stability. It consists of sp^2 hybridized honeycomb 2D layers of alternating boron and nitrogen atoms. In 3D crystals, boron and nitrogen atoms within each layer are bound by strong covalent bonding, whereas interlayer bonding is weak and van der Waals type, analogous to graphite (see ***Figure 1.5***).

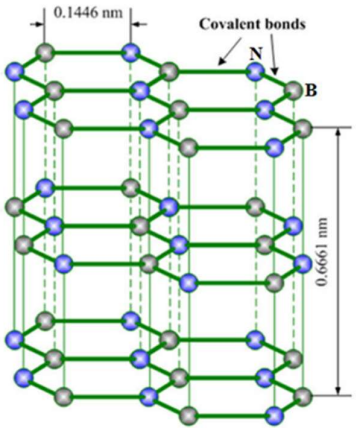

Figure 1.5. Structure of h-BN: Honeycomb lattice of alternating H and N with strong covalent bonding within the plane and weak van der-Waals bonds between the planes. (Adapted from *Chem. Rev. 2013, 113, 3766−3798*)[42]

Therefore, monolayer and few layers of h-BN could be extracted by means of micromechanical exfoliation, liquid exfoliation, or by means of chemical decomposition reactions from various precursors. High-quality h-BN 2D layers provided umpteen opportunities to exploit its robust physical and chemical properties for various applications even though it is a challenging process.

Hexagonal BN can be functionalized by hydrogenation or by substituting either boron or nitrogen or by other suitable atoms.[43, 44] For example, density functional theory (DFT) calculations show that fully hydrogenated h-BN has a lower bandgap of 3.05 eV which is much smaller than pure CVD deposited h-BN sheet (~6.07eV).[45, 46] Furthermore, first principles plane wave calculations indicate modification of electronic, and magnetic properties of h-BN sheets by add atom adsorption, or substitution for either B, or N by suitable atoms (viz. Sc, Ti, V, Cr, Fe, Pt, C, Si, B, O, Cu, Pd, and Ni).[47] Theoretical calculations predict that the incorporation of specific adatoms in the insulating h-BN monolayer modifies its ground state to magnetic metallic or half-metallic.[48]

1.4.2 Two-dimensional Transition Metal Dichalcogenides

Two-dimensional transition metal dichalcogenides (TMDs) are an important category of materials in IGAs. They are layered materials with strong in-plane bonding and very weak interlayer interactions. 2D layers having a thickness of unit cell orders can be exfoliated easily from their respective bulk precursors. Sheets of TMDs having tunable bandgaps (1-2 eV) could be employed for fabrication of field effect transistors and optoelectronic devices.[24] TMDs can be represented with the general

formula MX_2, where M corresponds to the transition metal atom from group IV (Ti, Hf, Zr etc.), group V (V, Ta, Nb etc.) or group VI (W, Mo etc.) and X is a chalcogen (S, Se, or Te). They form layered structures of the form X-M-X, with a plane of metal atoms sandwiched in between two hexagonal chalcogen planes. TMDs arrange themselves in hexagonal or rhombohedral geometry in general with the metal atoms coordinated octahedrally or trigonal prismatic to chalcogen atoms (see ***Figure 1.6***). Depending upon the coordination and oxidation state of metal atoms, TMDs show electronic properties ranging from metallic to semiconducting.

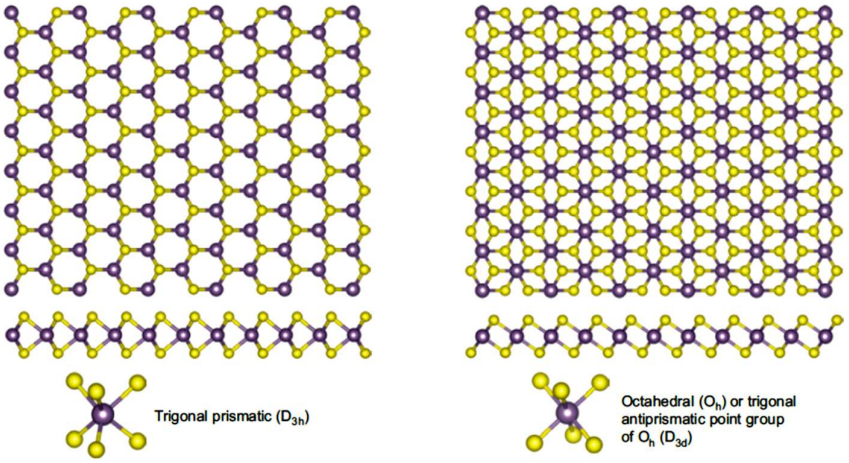

Figure 1.6 Structure of monolayer TMDs: c-Axis and section view of single-layer TMD with trigonal prismatic and octahedral coordination. Atom colour codes: purple, Metal; yellow, Chalcogen. (Adapted from *Nature Chemistry* 5(4): 263-275)[49]

Layer-dependent electronic properties of TMDs are of great interest since the optical bandgap of most of the TMD semiconductors undergoes a transition from indirect in bulk to direct bandgap in the monolayer.[49] For instance, the bulk indirect bandgap (1.3 eV) of MoS_2 increases to a direct

bandgap (1.8 eV) in monolayer. Valleytronic devices are yet another emerging applications of TMDs. The lack of inversion symmetry combined with spin-orbit coupling leads to a new branch of study known as 'spin and valley physics'. Evidence for valley confinement is already obtained in monolayer MoS_2.[50] In general, there are a number of impressive layer dependent properties in TMDs compared to their bulk counterparts which can be exploited for various applications.

1.4.3 Transition Metal Oxides

Atomically thin oxides of metals (pre-transition, transition, and post-transition), Transition Metal Oxides (TMOs) in general, possess improved properties compared to their bulk forms. Strongly polarizable O^{2-} ions contributes to the remarkable properties of TMOs.[51, 52] Polarization-induced non-uniform distribution of charges leads to electrostatic screening in nanoscales (typically 1-100nm) resulting in good local, surface and interfacial properties. Polarization-induced surface charges along with reduced symmetry of the surface in comparison to bulk materials enhance Coulombic interactions at the surface with the adjacent ions.[53] Such interactions result in the evolution of an interface potential which eventually shifts the Fermi level of the interacting species thereby changing the electronic properties. Other remarkable peculiarities are the hybridization of ionic orbitals contributing to electronically activated surfaces, normally aligned (to the surface) d orbitals of 2D TMOs generating spin and orbital frustrations, leading to unusual semiconducting properties.[54]

Many of the fundamental properties of TMOs are controlled by the ability of cations to have multiple oxidation states.[55] It is responsible for the rich electronic properties ranging from metallic to wide-gap insulating behaviour for the same TMO layer at different stoichiometry. They are also chemically and thermally very stable.[56]

1.4.4 Silicene, Germanene and Phosphorene

Graphene-like 2D analogues from Silicon and Germanium are called silicene[57] and germanene[58] respectively and are of interest owing to their impressive physical and chemical properties.[9, 59] The performance and scalability of the present day silicon-based electronics could be enhanced by using 2D sheets of silicene and germanene in electronic circuits. Both silicene and germanene have a hexagonal lattice (see ***Figure. 1.7***).

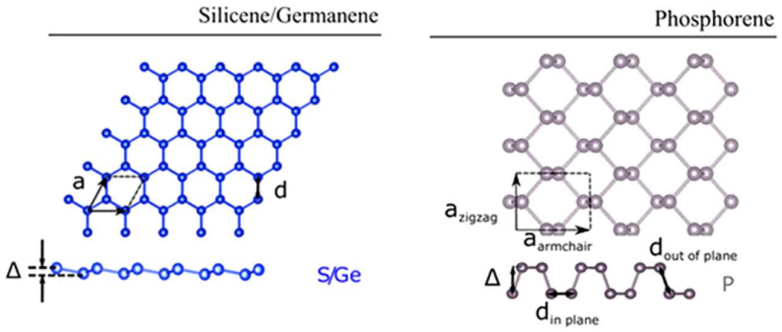

Figure 1.7. Structure of Germanene/Silicene and Phosphorene: c-Axis and section view of single-layer Silicene/Germanene and Phosphorene. (Adapted from *Scientific Reports volume 7, Article number: 44766 (2017)*)[60]

The possible existence of silicene and germanene has been predicted by Density Functional Theory (DFT) calculations, even before the successful isolation of graphene.[61] Much later, phosphorene, the 2D counterpart of black phosphorus, a stable allotrope of phosphorus at room-temperature,

was discovered.[10] Phosphorene, being a p-type 2D semiconductor is suitable for 2D p-type high-mobility complementary metal-oxide-semiconductor (CMOS) applications.

1.5 Synthesis of 2D materials

There exist a large number of methods that can be employed for the synthesis of 2D materials. They can be classified into two; bottom-up and top-down. In general, as in the case of other nanostructures, the former approach uses the ability of certain chemical reactions to form covalently linked 2D networks, whereas the latter relies on the exfoliation of their respective 3D counterparts to 2D sheets. Bottom-up processes such as chemical vapour deposition (CVD), molecular beam epitaxy (MBE) and other epitaxial growth techniques are employed to produce high-quality 2D layers having a uniform thickness and with minimum defects, however, these methods are not cost effective. Some of these important methods are briefly discussed below.

1.5.1 Micromechanical cleavage

In 2004, graphene was exfoliated by means of micromechanical cleavage of HOPG (highly ordered pyrolytic graphite) using a scotch-tape. This process involves the peeling of 2D sheets, layer by layer, from the bulk material using a scotch-tape. There are two types of micromechanical routes to effect exfoliation by overcoming the weak van der Waals forces between the layers – the normal force and the lateral force. One can exert normal pressure to peel off the layers or can make use of relative motion of weakly bounded adjacent layers by applying lateral force. The schematic is shown in ***Figure 1.8***.

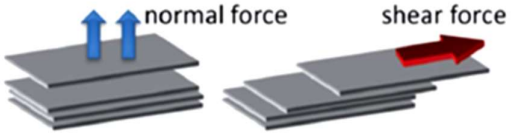

Figure 1.8. Micromechanical exfoliation: Schematic illustration of micromechanical exfoliation by scotch-tape method (Adapted from *J. Mater. Chem. A, 2015, 3, 11700–11715*)[62]

1.5.2 Liquid phase exfoliation

Yield from micromechanical exfoliation is very low and the process is time-consuming as well as labour-intensive. Liquid phase exfoliation could be one of the best alternatives to micromechanical exfoliation for increasing the yield. This method involves dispersion of the bulk material into a suitable solvent followed by ultrasonic bath sonication and subsequent centrifugation to obtain a suspension of corresponding 2D sheets. These 2D sheets can be separated from the suspension by suitable methods in order to use them for various applications. ***Figure 1.9*** summarizes different liquid exfoliation methods.

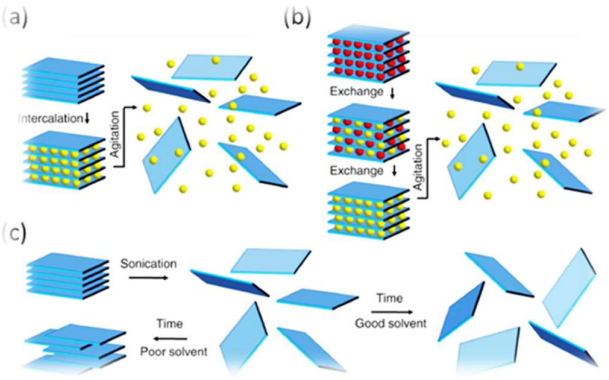

Figure 1.9. Schematic of liquid phase exfoliation: ***(a)*** Ion intercalation, ***(b)*** Ion exchange method, and ***(c)*** sonication. (Adapted from *Science 340,1226419 (2013)*)[63]

One of the oldest strategies for exfoliation of crystals with lowest reduction potential was by oxidation followed by dispersion into suitable solvents. The best-known example is the exfoliation of graphite into graphene which involves oxidation of

graphene using sulphuric acid and potassium permanganate to add hydroxyl and epoxide group to obtain GO. Hydrophilic GO allows water intercalation thereby obtaining monolayers of graphene oxide on ultrasonication. These graphene oxides could be reduced by means of chemical routes to obtain reduced graphene oxide which is analogous to graphene except having a few defects.[37]

Ion intercalation is another widely applied method taking advantage of the ability of layered materials to adsorb guest molecules in between their layers. Ion intercalation weakens the inter-layer van der Waals attraction and lowers the energy barrier for exfoliation. Intercalants like n-butyllithium or IBr can transfer charge to the layers, helps in further reduction in interlayer binding. Intercalation followed by thermal shock or ultrasonication in suitable solvents completes the exfoliation process. Stabilization of exfoliated sheets is possible electrostatically by introducing surface charge or by adding surfactants. However, ion intercalation methods are sensitive to ambient conditions and are considered to be a major drawback.

Another strategy is the ion exchange method. This method utilizes the property of layered double hydroxides, clays and some metal oxides having an exchangeable interlayer of cationic counterions. Soaking in acidic solution enables interchanging of such counterions with protons. These protons can be later replaced by large organic ions thereby effecting substantial swelling. This kind of swelling facilitates effective exfoliation by ultrasonication or by shear mixing to obtain negatively charged nanosheets.

A more recent strategy of liquid phase exfoliation is to apply ultrasonic energy to layered materials in a suitable solvent. Cavitation bubbles generated by ultrasonic waves collapse into high-energy jets, breaking up and separating the layered crystallites and effecting exfoliation. Modelling suggests that the surface energy of the solvent has to be similar to that of the layered materials to ensure the energy difference between the exfoliated and reaggregated states are very small, eventually removing the driving force for reaggregation.[64] Graphene, h-BN, TMDs, and some TMOs have been exfoliated in this way by using solvents such as N-methyl-pyrrolidone and dimethylformamide. Exfoliation can also be performed in surfactant or polymer solutions giving electrostatically or sterically stabilized nanosheets.

From the above discussions, it is very clear that the liquid exfoliation represents a versatile, scalable, and sustainable route for the synthesis of 2D nanosheets from their bulk counterpart. In addition, suspensions of nanosheets permit further processing in various ways that would otherwise be a tedious process. Suspensions allow the deposition of individual nanosheets on surfaces and the formation of thin as well as free-standing films, facilitates a simple way of mixing with other nanomaterials to form heterostructured solids, and enables insertion, as fillers, into polymer matrices.

The ability to isolate different phases of 2D materials via tuning the exfoliation chemistry opens up an exciting range of possibilities. For example, exfoliation via electrochemical ion intercalation leads to realization of the metallic (1T) phase in layered transition metal

chalcogenides, which cannot be accessed through other synthesis techniques.[65] This particular phase of MoS_2 has potential applications as a catalyst in hydrogen evolution reactions (HER).

Liquid exfoliated 2D materials could be easily integrated to large area electronic circuits through inkjet printing.[66] Since liquid phase exfoliation preserves the electronic structure, the properties of the bulk could be there in their respective 2D sheets as well, facilitating its usage for the same application with implemented miniaturization. For instance, liquid exfoliated 2D oxides and perovskites could be potential materials for high-κ dielectrics and multiferroics respectively.[67]

Due to the simplicity and ability of large scale production of 2D materials, liquid phase exfoliation is considered to be an ideal method to extend the top-down approach to a galaxy of other materials, having a rich set of distinct features that have not yet been exfoliated.

Another two important synthesis methods for layered 2D materials are chemical vapour deposition (CVD)[68] and hydrothermal method. CVD is considered to be the most promising route to grow 2D layered materials with a uniform thickness and having high purity as well as high yield, by precisely adjusting the precursor stoichiometry and growth conditions. In the hydrothermal method, a homogeneous solution of precursors is transferred to a Teflon-lined stainless steel autoclave and maintained at different temperatures for a given time. The dispersions of 2D nanomaterials synthesized via this method are usually utilized as catalysts for H_2 generation. So many other bottom-up methods such as self-assembly, template-assisted methods, solvothermal methods are also

employed for synthesis of different non-layered 2D materials.[13] Very recently, scientists employed a simple method in which 2D sheets of various oxides are exfoliated by rapid heating of their hydrous chlorides.[69]

1.6 Beyond Layered Materials

The area of 2D materials research mainly revolves around layered materials in which the intra-layer bonding is strong covalent whereas the inter-layer bonding is weak van der Waals type. A detailed description of this class of materials was provided in the previous sections. There are a large number of functional materials other than layered materials having three-dimensional bonding network. Taking into account the advantages of 2D geometry, it would be quite fascinating to synthesize 2D materials based on non-layered precursors. The enhanced properties owing to 2D morphology along with other important inherent material properties can emulate the existing layered 2D materials.

The most important peculiarity of non-layered 2D materials are the dangling bonds, which are absent in layered 2D materials, thereby enhancing the surface reactivity which enables them suitable for catalyst and sensing applications. However, breaking the 3D bonding network, sometimes across the unit cell axes, without disturbing the crystalline arrangement of atoms is a challenge. Most of the synthesis methods employed to obtain 2D non-layered materials are bottom-up approaches involving both wet chemical and dry routes.[13] The process involves perturbation of thermodynamic equilibrium and kinetics of molecules/atoms should be artificially controlled in order to attain required anisotropic growth. Controllable growth is pivotal to synthesize

new materials. So far, dry methods like CVD were employed in order to get highly crystalline and pure 2D non-layered materials.[70] Wet chemical methods such as surface-energy-controlled synthesis (SECS),[71] template-directed synthesis (TDS),[72] confined space synthesis (CSS),[73] colloidal synthesis (CS)[74] and solvothermal methods[75] were also employed for large scale production.

1.7 Natural Minerals: Good precursors for exotic 2D materials

Earth-abundant transition metal oxides (TMOs) are considered to be ideal precursors for 2D materials due to their robust physical and chemical properties.[11] It is well-known that the electronic and magnetic properties of the TMOs are really sensitive to their dimensionality enabling scientists and engineers to manipulate their electronic and magnetic ground state by thickness confinement to single or few atomic layers.[73] However, exfoliation methods are not reliable due to the inability of breaking strong chemical bonding network in all three dimensions. Recently many efforts have been devoted to the liquid phase exfoliation of TMO 2D sheets. Co_3O_4[76] nanosheets from $Co(OH)_2$, VO_2[77]nanosheets, ZnSe[78]nanosheets and $CoSe_2$[79]nanosheets are some of the recent instances of non-layered 2D materials synthesized by using liquid exfoliation.

Naturally occurring mineral ores, hematite (Fe_2O_3) and ilmenite ($FeTiO_3$) are considered to be candidate materials with high magnetization compared to pure hematite. In the case of hematite ore having robust lamellar magnetism, the magnetization is found to be 22 times greater than pure spin canted antiferromagnetic hematite.[80] Magnetite (Fe_3O_4), maghemite (γ-Fe_2O_3) and pyrite (FeS_2) are other iron-containing mineral

ores having excellent properties compared to their pure form, and can be good precursor materials too. Similarly, there is a galaxy of earth-abundant naturally occurring mineral ores, each one of them might have multiple superior properties compared to their pure forms. Hence naturally occurring mineral ores are thought to have tremendous potential in taking the non-layered 2D materials research to new dimensions.

1.8 Photocatalytic Water Splitting

Ever since the photoelectric effect was discovered by French scientist Edmond Becquerel researchers and scientists around the world are scouting for methods to successfully convert solar energy into some useful form such as electrical energy or chemical fuel. The former is achieved using solar cells whereas the latter could be possible by photoelectrochemical cells in which freely available sunlight is utilized to split water to generate hydrogen fuel. In a photoelectrochemical cell, water gets oxidized to oxygen at the semiconductor photoanode and reduced at the cathode. The schematic of a photoelectrochemical cell is given in ***Figure. 1.10***.

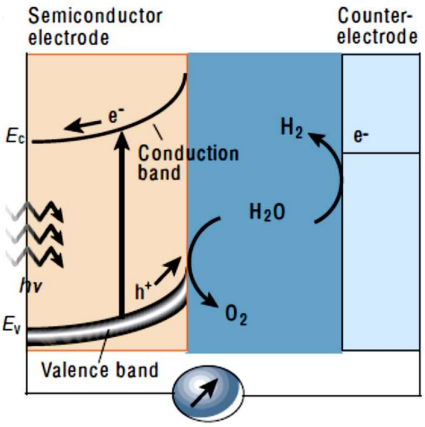

Figure 1.10. Photocleavage of water by a photoelectrochemical cell (From Photoelectrochemical Cells, *Gratzel*)[81]

The overall process is the splitting of water by utilizing sunlight in which oxidation and reduction occur at the semiconductor electrode and counter electrode respectively. For a semiconductor

to have photocatalytic activity, it must possess a favourable bandgap and band edge positions with respect to the water redox potential (see ***Figure 1.11***).

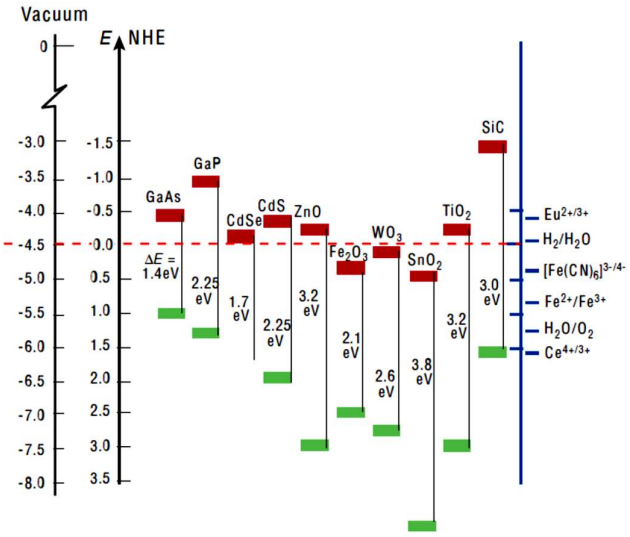

Figure 1.11. Band positions of several semiconductors with respect to water reduction potential (the energy scales are in electron volts; Water redox Potential = 1.23 eV). (From Photoelectrochemical Cells, *Gratzel*)[81]

Titanium dioxide has been an ideal choice for these applications following its first successful demonstration of water photolysis by Fujishima and Honda.[82] However, the large bandgap of TiO_2 (3.2 eV, see ***Figure. 1.11*** for band position of various semiconductors suitable for photolysis of water) absorbs only ultraviolet part of the solar spectrum thereby having a lower efficiency.[83]

Various attempts have been made to shift the spectral response of TiO_2 into the visible region of the solar spectrum or to discover new oxide materials having low bandgap energy to capture visible portion of solar light and are not succeeded.[84] Most of the oxide materials other than titania are unstable against photo-corrosion. A heterojunction of two semiconductors of low bandgap and wide bandgap (TiO_2) could well be a viable solution. It must be noted that the material with lower bandgap

could sensitize the wide bandgap material by absorbing visible light and injecting charge carriers to the latter.[85]

1.9 2D Materials in Catalytic Applications

Graphene and its derivatives are widely employed in catalytic applications.[86] Graphene's excellent catalytic properties are due to the following: large surface area leading to enhanced density of active sites, highly stable and durable as a catalyst or catalytic support due to excellent mechanical strength, high thermal conductivity makes them suitable for exothermic catalytic reactions, and high electrical conductivity enables them as an ideal candidate for electrocatalysis or as electrocatalytic supports. Despite these numerous opportunities, there exist challenges too. Zero bandgap is a notable challenge which makes pure graphene inert to catalysis. However, excellent tunability of electronic properties by slight perturbations enables graphene catalytically active.

The electronic properties of graphene can be tuned by means of the following strategies in order to make it catalytically active. They are size confinement, number of layers, edge and defects, the curvature of layers and introduction of dopants or functional groups.[87, 88] The electronic bandgap of graphene strongly depends on the size of graphene sheets and the number of layers.[28] The density of states (DOS) is different at the plane and edges of graphene. Edges could be either zigzag or armchair, both of them having different DOS.[89] Also, defects such as vacancies or dislocation may result in new electronic states thereby affecting the electronic transfer rate in graphene. Bending or folding of ultrathin graphene sheets, having different electronic states to planar graphene

sheets.[90] Introduction of dopants such as fluorine, nitrogen, phosphorus, boron, sulfur, some of the metal atoms and modification of graphene by oxygen, hydrogen or halogen (Fl, Cl, Br, I) containing functional groups may also modify DOS at the Fermi level which in turn enhances the catalytic properties.[91, 92]

The effectiveness of graphene and its derivatives in catalysis eventually spread into other members of the 2D family. Like graphene, most of the 2D materials are stable in ambient conditions and their robust electronic properties in the 2D form makes them excellent candidates for catalytic applications. Much recently, transition metal dichalcogenides (TMDs) such as MoS_2 and WS_2 are increasingly being explored owing to their superlative properties for catalytic applications.[93-95] For example, MoS_2, an indirect bandgap semiconductor in bulk transforms into a direct bandgap semiconductor in two dimensions.

The catalytic activity of TMDs is attributed to the S sites at the edges.[93] Hence, the greater the edge length of a TMD, the greater will be the catalytic activity. One more interesting observation is that reducing the number of layers is found to be increasing the catalytic activity as well.[96] Hence, one of the possible ways to boost the catalytic activity is to increase the edge length by restricting the number of layers during synthesis. Another reason could be the increase in hopping of electrons from the electrodes to the monolayer TMDs. Just like graphene, MoS_2 is also inert in catalysis in general. However, the catalytic activity may originate by introducing heteroatoms in the layers. S could be replaced by N, O, B and some others and Mo could be replaced by transition metal

atoms such as Ni, Co or Pt.[97] Density functional theory calculations confirms the possible enhancement in electronic properties of S sites in the MoS_2 surface which in turn enhances the catalytic property enormously.[98]

Other TMDs such as SnS_2 and SnS are also found to be catalytically active especially in photocatalysis.[99, 100] Unlike MoS_2 and WS_2, structural reconstructions are inherent in these TMDs which increases the DOS of the valance band edge as compared to the bulk. Increase in DOS leads to enhanced absorption and mobility of photogenerated charge carriers. Also, the ultrathin nature of the nanosheets reduces the diffusion length of photogenerated charge carriers thereby reducing the recombination before reaching the active sites to carry out the desired chemical reaction. Due to these factors, semiconductor nanosheets are expected to have excellent photocatalytic abilities such as photoelectrochemical water splitting.

In conclusion, the successful synthesis of ultrathin semiconductor nanosheets, not essentially from layered bulk materials, such as metal oxides, metal tellurides etc. as explained in the previous sections, may result in the excellent photo and electrocatalytic active materials with decent economic viability.

1.10 Magnetism

The first scientific investigation of magnetism dates back to 1600 when Englishman William Gilbert published his book ‘On the Magnet’ in which he mentioned the results of his experiments with lodestones and iron magnets. He could establish an exact picture of earth’s magnetism which cleared away many other persisting superstitions about earth’s

magnetism. It was in 1825, the first electromagnet was made following the discovery by Hans Christian Oersted that an electric current produces a magnetic field. This invention revolutionized the field of magnetism which enabled the researcher's access to powerful fields that could not be achievable by conventional permanent magnets.

With regard to the origin of magnetism in materials, the magnetic moment of a free atom in the absence of a magnetic field has two contributions; first is the orbital angular momenta (L) of electrons and secondly the contribution to its magnetic moment due to the spin of the electron about its own axis known as spin angular moment (S). Hence the observed magnetic moment of an atom is due to the combined effect of the spin and orbital angular momenta of its electrons. Moreover, magnetism is a cooperative phenomenon and takes many shapes depending upon the degree of cooperation, and such cooperation is known as spin-orbit (L-S) coupling. The L-S coupling is also a contributing factor to the observed magnetic moment of an atom. The subsequent sections take a look at different magnetic forms.

1.11 Types of Magnetism

1.11.1 Diamagnetism

In addition to electron spin and orbital angular momenta contributions, there is another contribution to the magnetic moment of a free atom in the presence of an external magnetic field. It is due to the change in orbital motion of the electron by the applied magnetic field. It is known as the diamagnetic effect and is responsible for diamagnetism in all the atoms. However, diamagnetism itself is really weak so that only those atoms

having no net magnetic moment are classified as diamagnetic. In the other materials, diamagnetic contributions are overshadowed by other stronger interactions such as ferromagnetism and antiferromagnetism.

A diamagnetic material usually expels the applied field which is counter-intuitive. This is a consequence of Lenz's law. When a diamagnetic material is placed in an external magnetic field, electromagnetic induction induces extra currents in the atoms. The direction of these induced currents is in such a way that it establishes a field opposing the applied field which results in its eventual expulsion. Hence the diamagnetic susceptibility is small and negative (see ***Figure 1.12***)

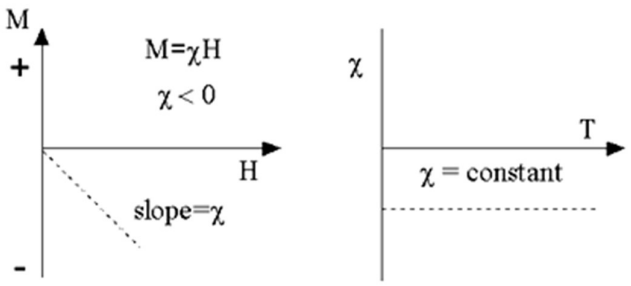

Figure 1.12 (a) Magnetic response of a diamagnetic material to an applied field and ***(b)*** the variation of diamagnetic susceptibility with temperature (Adapted from NPTEL lectures https://nptel.ac.in/)

Even though diamagnetism is universal in nature, only those materials having no other magnetic behaviour or atoms having completely filled or empty atomic/molecular orbitals are classified as diamagnetic. For example, noble gases having completely filled shells and some diatomic gases having completely filled molecular orbitals are diamagnetic.

1.11.2 Paramagnetism

Paramagnetic materials are those having net magnetic moments because the moments are very weakly coupled so that thermal energy causes random orientations of magnetic moments as shown in ***Figure 1.3a***. When

a magnetic field is applied, the moments tend to align in the direction of the applied field. However, only a small fraction of moments get aligned in the field direction for all practical field strengths (***Figure 1.13b***).

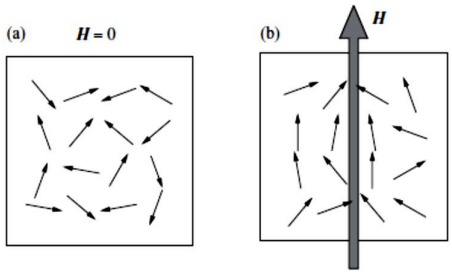

Figure 1.13 Alignment of magnetic moments in a paramagnetic material. ***(a)*** in the absence of a magnetic field (H=0), and ***(b)*** in the absence of a magnetic field (H>0). (Schematic is adapted from Spaldin, N. A., *Magnetic materials: fundamentals and applications*. Cambridge University Press: 2010)[101]

Many of the transition element salts, metallic aluminium and diatomic gas O_2 are paramagnetic. In nature, all the ferromagnetic and ferrimagnetic materials become paramagnetic above a particular transition temperature called Curie temperature (Tc) at which the thermal energy is sufficient to balance the ferromagnetic interactions allowing the ordering of moments.

Langevin's theory of Localized moments establishes the temperature dependence of susceptibility in paramagnetic materials in the form of Curie's law (equation 1.3),

$$\chi = \frac{M}{H} = \frac{C}{T} \qquad (1.3)$$

where *C* is the Curie's constant and *T* is the temperature.

A more generalized form of Curie's law is given by Curie-Weiss law (equation 1.4),

$$\chi = \frac{C}{T-\theta} \qquad (1.4)$$

Paramagnets obeying Curie-Weiss law undergo spontaneous ordering and become ferromagnetic below Curie temperature, *Tc*.

1.11.3 Ferromagnetism

In ferromagnetic materials, there is a strong interaction, internal by nature, among the magnetic moments that enable them to align in a particular direction to yield a spontaneous magnetization in the presence of a small applied field or even in the absence of an external field (***Figure 1.14***). This particular interaction is quantum mechanical by origin which has no classical counterparts.

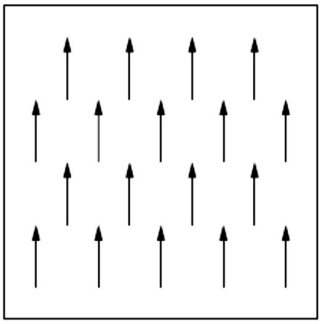

Figure 1.14. Alignment of magnetic moments in a ferromagnetic material. (Schematic is adapted from Spaldin, N. A., *Magnetic materials: fundamentals and applications*. Cambridge University Press: 2010)[101]

As we all know, ferromagnetic materials undergo a transition to paramagnetic above T_c according to Curie-Weiss law. This evidence lead Weiss to conclude that a molecular field acts in ferromagnets below T_c which is strong enough to magnetize the material even without an external magnetic field or a ferromagnetic material can be considered as a paramagnet with a strong internal molecular field. Hence Langevin's theory of localized moments together with Weiss molecular field theory could account for the properties of ferromagnetic materials. The Curie temperature of a ferromagnetic material is given by (equation 1.5),

$$T_C = \frac{\gamma N m_{eff}^2}{3k_B} \qquad (1.5)$$

where $m_{eff} = g\sqrt{J(J+1)}$ γ is Weiss molecular field and *N* is the number of interacting magnetic dipoles.

However, localized magnetic moments theory failed to account for the magnetic moment per atom of the ferromagnetic materials. This is because Weiss theory predicts the same magnetic dipole moment per atom/ion in both ferromagnetic as well as paramagnetic phases. This is not true in practice. Secondly, in localized moment theory, the magnetic moment on each atom/ion should correspond to an integer multiple of electronic moments and is found to be wrong experimentally. To avoid these shortcomings of localized moment's theory, band theory/collective electron theory is employed.

According to band theory, the exchange energy can be minimized if all the electrons have the same spin which is against Pauli's exclusion principle that no two electrons in an orbital can have the same spin state. So the only way to minimize exchange energy is to transfer electrons to band states of higher energies. This energy requirement prevents simple metals from being ferromagnetic. Band theory could account the discrepancies in the localized moment's theory.

Nevertheless, in real life, neither model is correct. The most successful method currently available is density functional theory (DFT).[102] It is an ab-initio many-body theory which includes (in principle) all the electronic interactions.

1.11.3.1 Magnetic Domains

It has been already discussed that the quantum mechanical exchange interaction is responsible for spontaneous parallel alignment of spins and thereby magnetic dipole moments. One might expect a ferromagnetic material as a single large entity having all the magnetic dipoles aligned in a particular direction. However, in practice, it is not true. A ferromagnetic material comprised of a large number of small entities called domains consisting of a large number of atomic moments, each of which is aligned in specific directions. Individual domains are separated by means of certain boundaries known as domain walls.

The significance of domain formation in a ferromagnetic material is that it can minimize the total magnetic energy, the components of which are exchange energy, magnetostatic energy, magnetocrystalline energy and magnetostrictive energy. Out of these four components, magnetostatic energy is the one having a major role in the process of domain formation. The spontaneous magnetization of a ferromagnetic block results in developing an internal magnetic field/magnetization which opposes its own magnetization. It is known as the demagnetizing field, H_d. H_d is responsible for magnetostatic energy. It can be minimized by reducing the demagnetizing field. One way to reduce H_d is to form small magnetic domains at the expense of exchange energy since moments at the boundaries of adjacent domains are not parallel. The width of the domain walls is determined in such a way that the total energy is minimum across the boundary. The most energetically favourable domain walls are those which do not produce magnetic poles within the material thereby introducing no demagnetizing field, H_d. There are two kinds of domain

walls – *Bloch walls* (***Figure 1.15a***), in which spins rotate within the plane of the wall, and in *Neel walls* (***Figure 1.15b***) spins rotate in the plane perpendicular to the plane of the wall.

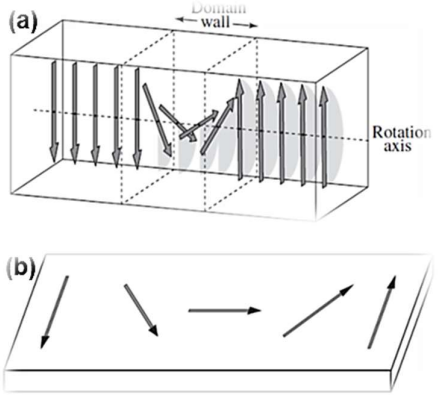

Figure 1.15. (a) Rotation of spins in a Bloch wall. ***(b)*** Neel wall spin dynamics. (Schematic is adapted from Spaldin, N. A., *Magnetic materials: fundamentals and applications*. Cambridge University Press: 2010)[101]

1.11.3.2 Magnetic Hysteresis

Magnetic hysteresis of a ferromagnetic material could be explained in terms of domain dynamics inside the material in an applied magnetic field (***Figure 1.16***). When a magnetic field is applied at an angle slightly off the easy axis of magnetization, from the initial demagnetized state, the domain which aligns closer the field direction starts growing at the expense of others. This growth is facilitated by the motion of domain walls which is not completely reversible. When the applied magnetic field is sufficient enough to eliminate all the domain walls, the sample becomes a single domain with its magnetization pointing in the easy axis close to the applied field direction. Any further increase in magnetization can only occur by rotating the moments from easy axis towards the applied field direction which is known as saturation.

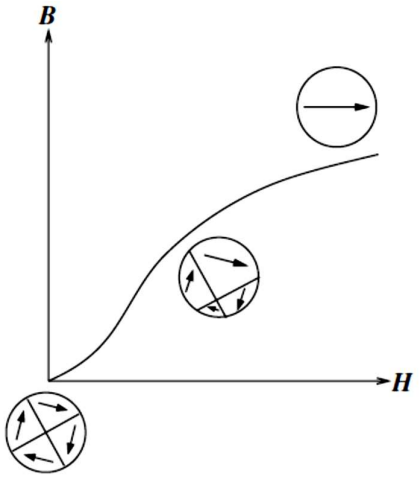

Figure 1.16. Domain dynamics during magnetization of a ferromagnetic material. (Schematic is adapted from Spaldin, N. A., *Magnetic materials: fundamentals and applications*. Cambridge University Press: 2010)[101]

As we remove the applied field at saturation, the dipoles rotate back to easy axis and the magnetic moment decreases. This initial part involving only dipole rotation is reversible. Next part is the initiation of reversal of the magnetic domains by demagnetizing field (H_d) allowing the sample to demagnetize partially. The domain walls are unable to reverse fully to their original positions since the process is driven by H_d which is not strong enough to overcome the energy barriers encountered while the domain walls intersect with crystal imperfections. As a result, the magnetization curve shows hysteresis and some magnetization remains even after complete removal of the applied field. A field in the opposite direction of the initial applied field is necessary to nullify the magnetization and is known as the coercive field.

From an application perspective, materials having large remanence and coercivity are known as hard magnets and are useful as a permanent magnet. High purity materials with a few dislocations/dopants can be easily magnetized/demagnetized and having small remanence and coercivity. Such materials are known as soft magnetic material which is useful in manufacturing electromagnets, magnetic storage devices and transformer cores.

1.11.4 Antiferromagnetism

Antiferromagnetic materials are those in which the interactions among the magnetic moments are in such a way that adjacent moments align antiparallel to each other leaving a zero net magnetic moment (see ***Figure 1.17***). An antiferromagnetic material is comprised of two interpenetrating and identical sublattices of magnetic ions. Below a critical temperature called Neel Temperature (T_N), one sublattice gets magnetized spontaneously in a particular direction whereas the other in an exactly opposite direction at the same magnitude. As a consequence of this arrangement, antiferromagnetic materials have no net spontaneous magnetization and their response to an externally applied magnetic field is linear just like a paramagnetic material at a particular temperature. Their susceptibility is small and positive.

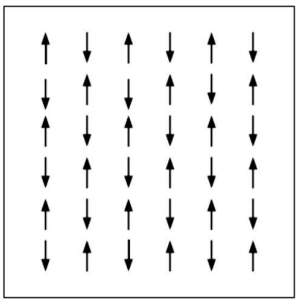

Figure 1.17. The ordering of magnetic moments in an antiferromagnetic material. (Schematic is adapted from Spaldin, N. A., *Magnetic materials: fundamentals and applications*. Cambridge University Press: 2010)[101]

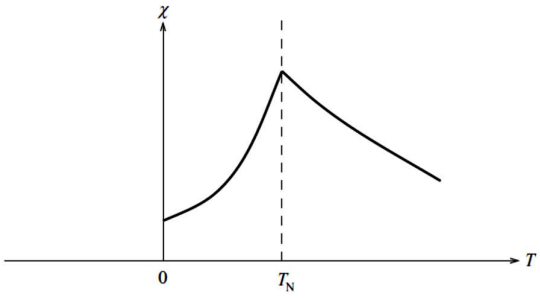

Figure 1.18. Temperature dependence of susceptibility of an antiferromagnetic material. (Schematic is adapted from Spaldin, N. A., *Magnetic materials: fundamentals and applications*. Cambridge University Press: 2010[101])

The temperature dependence is similar to that of a paramagnet. Below T_N, however, χ decreases as we decrease temperature (***Figure 1.18***).

1.11.5 Ferrimagnetism

The ferrimagnets are microscopically similar to antiferromagnetic materials consisting of two interpenetrating sublattices of magnetic atoms/ions within which the moments are aligned parallel. These two sublattices are aligned antiparallel to each other with different magnitudes of magnetic moments so that there is a net magnetization (***Figure 1.19***).

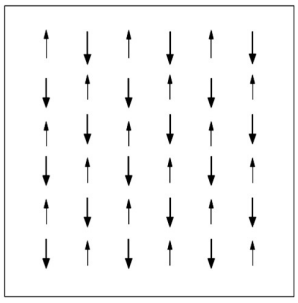

Figure 1.19. Alignment of magnetic moments in a ferrimagnetic material. (Schematic is adapted from Spaldin, N. A., *Magnetic materials: fundamentals and applications*. Cambridge University Press: 2010)[101]

Macroscopically they behave like ferromagnetic materials exhibiting large and positive susceptibility and magnetic hysteresis.

Having explained different aspects of van der Waals 2D materials, the importance of 2D materials in photocatalytic water splitting and introductory concepts of magnetism, it is imperative that the motivation of the thesis is clearly stated. The ensuing section provides a brief account of the motivation of the present investigation followed by the objectives.

1.11 Motivation

The successful mechanical exfoliation of one atom thick graphene from graphite by the scotch tape method was a historic milestone in the realm of carbon nanomaterials. Since then, we witnessed burgeoning research

activities in the area of two-dimensional (2D) materials leading to the discovery of new 2D materials and also new phenomena which are unprecedented. Further, these 2D materials serve as ideal templates for validating purely quantum mechanical phenomena like anomalous quantum Hall effect, quantum tunnelling and conduction at zero charge carrier density to name a few. Though the expectations on graphene to replace all the existing materials didn't meet the anticipations, however, the discovery of graphene served as a precursor for creating other new 2D materials such as transition metal chalcogenides (TMDs), phosphorene, germanene, silicene and 2D transition metal oxides. The emergence of a new class of solids called 'van der Waals (vdW) solids' is also a spin-off of this discovery.

Exfoliating a monolayer or a few layers of a 2D material from its layered bulk counterpart was considered energetically feasible thus enabling employment of top-down techniques like mechanical scotch tape method or liquid phase exfoliation to obtain a 2D material from its bulk precursor material quite easily. However, extraction of a monolayer or a few layers from a non-layered bulk counterpart remained elusive to scientists and engineers till recently.

A quick scan of the latest literature on magnetism at 2D level tells us that 2D magnetism is an emerging area of physics and is going to be both evolutionary as well as revolutionary from a fundamental as well as from an applied perspective. From the statistics given in ***Figure 1.20***, it is very clear that the number of journal publications in vdW 2D materials is approximately 100 times greater than the number of papers in magnetic

vdW materials. Hence, magnetism in two dimensions is still in its infancy and tremendous efforts are still on to realize a 2D magnet. However, until recently, freestanding 2D sheets with intrinsic ferro/ferrimagnetism have not been realized.[103, 104] It was believed that theoretically, the magnetic ground state is impossible at two dimensions.[105] Different strategies such as defect engineering, impurity doping, applying external strain etc., have been employed in order to introduce magnetism in 2D atomic layers.[44, 106-108] Even though tremendous efforts have been devoted to materialize magnetism at two dimensions, the field is wide open and there exist huge scope for big-time research.[19, 109] Any attempt to realize a magnetic 2D material will contribute to the eventuation of future spintronic devices.

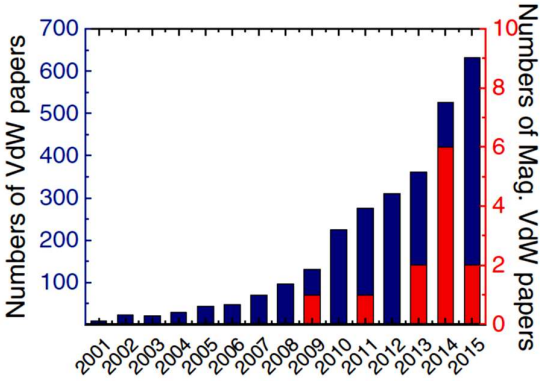

Figure 1.20. Lack of available literature in 2D magnetic materials: Histogram showing number of annual publications in 2D van der Waals (vdW) materials and magnetic vdW materials from 2001 to 2015 (Adapted from *J. Phys.: Condens. Matter 28 (2016) 301001*)[110].

A material which exhibits antiferromagnetic ordering in bulk, on exfoliation, transforms into a material with ferromagnetic ordering, will be of great interest from a fundamental perspective. Such materials provide a rich platform to understand 2D magnetism. Bulk oxides like hematite (Fe_2O_3), ilmenite ($FeTiO_3$) and semiconducting binary telluride of manganese – manganese telluride (MnTe) are non-layered and are antiferromagnetic as well. Their crystal structure is hexagonal and the favourable *c/a* ratio augurs well for easy exfoliation. Both hematite and ilmenite have been previously

employed for water-splitting applications by the phenomena of photocatalysis. Their favourable bandgap and band-edge characteristics serve well for the production of green fuel hydrogen (H_2) by photocatalytic water splitting.[111, 112] 2D counterparts of hematite and ilmenite could be a good choice of materials for this process since the bandgap and band-edge is suitably modified encompassing the visible region of the solar spectrum. All these three materials on exfoliation are expected to display interesting magnetic properties as well.

Thus exfoliation of a few layered 2D materials from their non-layered bulk precursors namely hematite, ilmenite and manganese telluride is one of the motivations of this study. Since their bulk is antiferromagnetic in nature and on exfoliation it might display either ferromagnetic ordering or might destroy the magnetic ordering to become paramagnetic. Thus these 2D non-layered materials could serve as ideal templates to investigate 2D magnetism. This is yet another motivation for the present investigation. Moreover, these extracted layers will be made into heterojunction with titania (TiO_2) nanotubes and its photocatalytic activity will be studied thoroughly and form another major objective of the present work.

Exfoliation of a non-van der Waals solids may occur in certain crystalline directions which are energetically favourable. The preferential exposure of certain planes in the exfoliated mono/few layers is of utmost importance since it determines the stability and other properties such as magnetism and its viability as a photocatalytic material. Molecular dynamics (MD) simulations and phonon dispersion could be employed to know the stability of exfoliated sheets of a certain orientation. Density

functional theory (DFT) calculations could well be the tool to theoretically predict other important properties such as density of states, magnetism and optical bandgap. Theoretical prediction of energetically favourable mono/few layers, densities of states (DOS), magnetic ground state and optical bandgap is yet another motive of the present investigation.

Magnetic vortices are a hurricane like swirls of magnetic spins in the ultra-thin micrometre or sub-micrometre ferromagnetic dots. In general, ferromagnetic materials forms domains in order to reduce magnetostatic energy. However, in ferromagnetic dots (or squares), when the thickness becomes much smaller than the dot diameter (or side), all the spins tend to align in the plane in such a way that the spin direction undergoes gradual change as it curls inward towards the centre so as to minimize loss of exchange energy and to cancel out dipole energy. As we go towards the dot centre, the angle between the adjacent spins in the swirl becomes larger and larger which results in the spins at the core to be oriented parallel to the normal of the plane.

The Monte-Carlo simulation of the surface and the cross-section along the core are shown in the ***Figure. 1.21 (A&B)***. It was also proved that the central vortex core exists only if the dimensions of the ferromagnetic dots are optimum. Precisely, the thickness should be made as small as possible so as to get a good vortex ground state. If the thickness exceeds a certain limit, the spins of the top and bottom layers tend to cancel each other and as a result, the perpendicular magnetization vanishes.

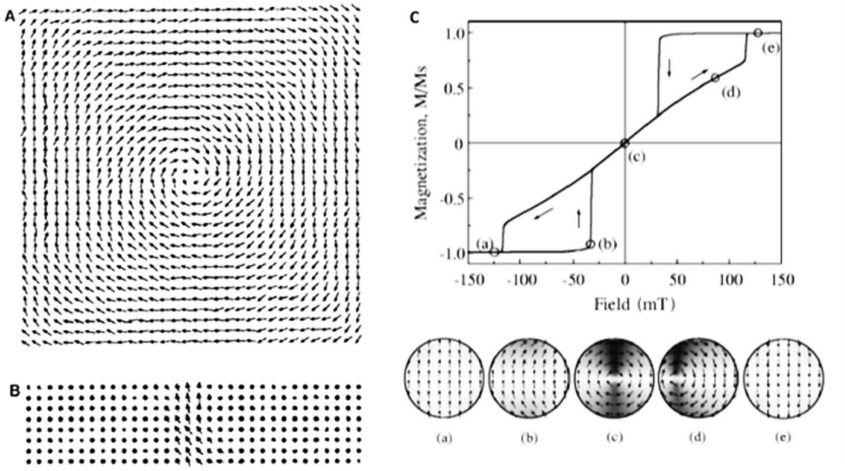

Figure 1.21. Vortex Characteristics*:** Monte-Carlo simulation of magnetic vortices ***(A) surface view, ***(B)*** Cross-section view at the vortex and ***(C)*** Typical hysteresis loop for a magnetic vortex highlighting nucleation, displacement and annihilation of vortices (From *Physical Review B* 65(2): 024414)[113]

Figure. 1.21C depicts a typical hysteresis behaviour and spin evolution with the magnetic field of a vortex system ((a)-(e)). Beginning from the saturation (a) where the system is a single domain state, as we decrease the field, vortex state is nucleated at a particular field called nucleation field, Hn, characterized by an abrupt fall in magnetization (b). Now the vortex core is located at the centre of the dot (c). If we increase the field in the reverse direction, the vortex core starts moving towards the circumference of the dot (shown by (d)) and eventually expels out at a particular field called annihilation field, Ha, to reach back at single domain state (e).

The thermal energy could also aid the switching process if it is greater than the energy barrier pertaining to the states.[114] Hence, there is a temperature at which vortex state can switch to collinear state and vice-versa without the expense of energy or both states can co-exist and is

known as bifurcation temperature (T_e) of the vortices.[115] Tailoring the bifurcation temperature T_e is really important to have better control on vortex dynamics for applications since the devices are susceptible to thermal fluctuations.

An understanding of the vortex dynamics offers ample opportunities in future spintronic devices such as vortex controlled random access memory (VRAM), nanoantennas, high density patterned magnetic media, nanosensors to name a few. Another application of magnetic vortices envisaged is in quantum computing since vortices could be deployed to control electron spin. These robust properties of vortices make them an exceptional system for research. Parameters such as the bi-stability of vortex core and chirality, dependence of Hn/Ha on Curie temperature (Tc) of the ferromagnet, dependence of Hn/Ha on the dimensions of ferromagnetic discs, inter-disc separation of dot arrays, and also the exchange interaction among the arrays of discs matters a lot as far as vortex dynamics is concerned. We choose a composition of Fe_xPd_{100-x} with x varying from 13 to 20 deposited on closely packed polystyrene hemispheres to study the variation of bifurcation temperature (T_e) with respect to the iron composition (x). This is yet another motivation for the present work.

Conventional magnetic measurement techniques such as vibrating sample magnetometer (VSM), SQUID and X-ray based synchrotron techniques are expensive and are meant for bulk magnetic measurements. For samples having 2D geometry – especially 2D materials and thin films, a magnetic measurement set up capable of probing surface magnetism is

essential. Magneto-optic Kerr effect (MOKE) set up is a well-known choice and has been widely employed for local and surface magnetic measurements of thin films and 2D materials. MOKE set up works on the basis of the magneto-optic Kerr effect.[21] When a polarized light beam incident upon the surface of a magnetic material, the reflected light undergoes a polarization rotation (***Figure 1.22***).

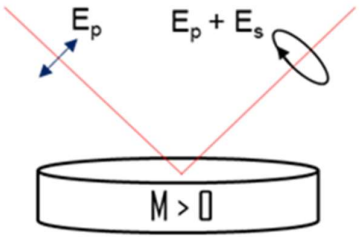

Figure 1.22. Schematic of Magneto-Optic Kerr Effect

The rotation of polarization is directly related to the magnetization of the magnetic material within the probing region of the laser which is ~20 nm, and hence MOKE is an exceptional tool to study the magnetization of ultra-thin magnetic thin films and 2D materials which can be as thin as one atomic layer. Fabrication of a table-top magneto-optic Kerr effect magnetometer, its calibration, automation and evaluation of the initial results forms another important aspect of this study.

Thus the objectives of the present investigations can be summarized as follows.

1. Exfoliation of a 2D material from a non-layered naturally occurring iron ore hematite for the first time and investigations on the magnetic and photocatalytic water-splitting properties.
2. Extracting yet another novel 2D material from a non-layered naturally occurring titania ore ilmenite and to study

the magnetic properties as well as photocatalytic hydrogen evolution.

3. To exfoliate a 2D material from non-layered bulk precursor manganese telluride (MnTe) and to investigate the change in magnetic properties due to exfoliation.
4. Creation of magnetic vortices on 2D nanocaps of soft magnetic alloy of the form Fe_xPd_{100-x} on curved surfaces of polystyrene and to tune the bifurcation temperature (T_e) of magnetic vortices with varying x, being the Fe concentration.
5. To fabricate an in-house fully automated magneto-optic Kerr effect (MOKE) set up for the investigation of surface magnetism and to check the validity of the initial measurements using the Stoner-Wohlfarth model.

1.12 References

1. E. Roduner, *Chemical Society Reviews*, 2006, **35**, 583-592.
2. O. Shenderova, V. Zhirnov and D. Brenner, *Critical Reviews in Solid State and Material Sciences*, 2002, **27**, 227-356.
3. H. W. Kroto, J. R. Heath, S. C. O'Brien, R. F. Curl and R. E. Smalley, *Nature*, 1985, **318**, 162-163.
4. P. M. Ajayan, *Chemical Reviews*, 1999, **99**, 1787-1800.
5. A. K. Geim and K. S. Novoselov, *Nat Mater*, 2007, **6**, 183-191.
6. K. S. Novoselov, A. K. Geim, S. V. Morozov, D. Jiang, Y. Zhang, S. V. Dubonos, I. V. Grigorieva and A. A. Firsov, *Science*, 2004, **306**, 666-669.
7. K. Watanabe, T. Taniguchi and H. Kanda, *Nature materials*, 2004, **3**, 404.
8. K. F. Mak, C. Lee, J. Hone, J. Shan and T. F. Heinz, *Physical Review Letters*, 2010, **105**, 136805.
9. N. J. Roome and J. D. Carey, *ACS Appl. Mater. Interfaces*, 2014, **6**, 7743-7750.
10. H. Liu, A. T. Neal, Z. Zhu, Z. Luo, X. Xu, D. Tománek and P. D. Ye, *ACS Nano*, 2014, **8**, 4033-4041.
11. K. Kalantar-zadeh, J. Z. Ou, T. Daeneke, A. Mitchell, T. Sasaki and M. S. Fuhrer, *Applied Materials Today*, 2016, **5**, 73-89.
12. J. Yu, Q. Wang, D. O'Hare and L. Sun, *Chemical Society Reviews*, 2017, **46**, 5950-5974.
13. F. Wang, Z. Wang, T. A. Shifa, Y. Wen, F. Wang, X. Zhan, Q. Wang, K. Xu, Y. Huang, L. Yin, C. Jiang and J. He, *Advanced Functional Materials*, 2017, **27**, 1603254-n/a.
14. B. D. Cullity and C. D. Graham, *Introduction to Magnetic Materials*, John Wiley & Sons, 2011.
15. M. N. Baibich, J. M. Broto, A. Fert, F. N. Van Dau, F. Petroff, P. Etienne, G. Creuzet, A. Friederich and J. Chazelas, *Physical Review Letters*, 1988, **61**, 2472.
16. A. Ramirez, *Journal of Physics: Condensed Matter*, 1997, **9**, 8171.
17. S. S. Parkin, C. Kaiser, A. Panchula, P. M. Rice, B. Hughes, M. Samant and S.-H. Yang, *Nature Materials*, 2004, **3**, 862.
18. S. A. Wolf, D. D. Awschalom, R. A. Buhrman, J. M. Daughton, S. von Molnár, M. L. Roukes, A. Y. Chtchelkanova and D. M. Treger, *Science*, 2001, **294**, 1488-1495.
19. N. Samarth, *Nature*, 2017, **546**, 216.

20. T. Shinjo, T. Okuno, R. Hassdorf, K. Shigeto and T. Ono, *Science*, 2000, **289**, 930-932.
21. Z. Q. Qiu and S. D. Bader, *Review of Scientific Instruments*, 2000, **71**, 1243-1255.
22. C. Rao, H. Ramakrishna Matte and U. Maitra, *Angewandte Chemie International Edition*, 2013, **52**, 13162-13185.
23. H. Ramakrishna Matte, A. Gomathi, A. K. Manna, D. J. Late, R. Datta, S. K. Pati and C. Rao, *Angewandte Chemie International Edition*, 2010, **49**, 4059-4062.
24. Q. H. Wang, K. Kalantar-Zadeh, A. Kis, J. N. Coleman and M. S. Strano, *Nature Nanotechnology*, 2012, **7**, 699-712.
25. D. Jariwala, V. K. Sangwan, L. J. Lauhon, T. J. Marks and M. C. Hersam, *ACS Nano*, 2014, **8**, 1102-1120.
26. Y. Tokura and N. Nagaosa, *Science*, 2000, **288**, 462-468.
27. M. Osada and T. Sasaki, *Advanced Materials*, 2012, **24**, 210-228.
28. A. C. Neto, F. Guinea, N. M. Peres, K. S. Novoselov and A. K. Geim, *Reviews of Modern Physics*, 2009, **81**, 109.
29. M. Katsnelson and K. Novoselov, *Solid State Communications*, 2007, **143**, 3-13.
30. L. Falkovsky, 2008.
31. E. Pop, V. Varshney and A. K. Roy, *MRS bulletin*, 2012, **37**, 1273-1281.
32. I. Ovid'Ko, *Rev. Adv. Mater. Sci*, 2013, **34**, 1-11.
33. D. Abergel, V. Apalkov, J. Berashevich, K. Ziegler and T. Chakraborty, *Advances in Physics*, 2010, **59**, 261-482.
34. N. Peres, *Reviews of Modern Physics*, 2010, **82**, 2673.
35. V. Georgakilas, M. Otyepka, A. B. Bourlinos, V. Chandra, N. Kim, K. C. Kemp, P. Hobza, R. Zboril and K. S. Kim, *Chemical Reviews*, 2012, **112**, 6156-6214.
36. S. Park and R. S. Ruoff, *Nature Nanotechnology*, 2009, **4**, 217.
37. D. R. Dreyer, S. Park, C. W. Bielawski and R. S. Ruoff, *Chemical society reviews*, 2010, **39**, 228-240.
38. H. He, J. Klinowski, M. Forster and A. Lerf, *Chemical Physics Letters*, 1998, **287**, 53-56.
39. C. N. R. Rao and U. Maitra, *Annual Review of Materials Research*, 2015, **45**, 29-62.
40. P. Ajayan, P. Kim and K. Banerjee, *Physics Today*, 2016, **69**, 38-44.

41. R. Lv, J. A. Robinson, R. E. Schaak, D. Sun, Y. Sun, T. E. Mallouk and M. Terrones, *Accounts of Chemical Research*, 2015, **48**, 56-64.
42. M. S. Xu, T. Liang, M. M. Shi and H. Z. Chen, *Chemical Reviews*, 2013, **113**, 3766-3798.
43. Q. Weng, X. Wang, X. Wang, Y. Bando and D. Golberg, *Chemical Society Reviews*, 2016, **45**, 3989-4012.
44. S. Radhakrishnan, D. Das, A. Samanta, A. Carlos, L. Deng, L. B. Alemany, T. K. Weldeghiorghis, V. N. Khabashesku, V. Kochat and Z. Jin, *Science Advances*, 2017, **3**, e1700842.
45. K. K. Kim, A. Hsu, X. Jia, S. M. Kim, Y. Shi, M. Hofmann, D. Nezich, J. F. Rodriguez-Nieva, M. Dresselhaus, T. Palacios and J. Kong, *Nano Letters*, 2012, **12**, 161-166.
46. W. Chen, Y. Li, G. Yu, C.-Z. Li, S. B. Zhang, Z. Zhou and Z. Chen, *Journal of the American Chemical Society*, 2010, **132**, 1699-1705.
47. C. Ataca and S. Ciraci, *Physical Review B*, 2010, **82**, 165402.
48. J. Zhou, Q. Wang, Q. Sun and P. Jena, *Physical Review B*, 2010, **81**, 085442.
49. M. Chhowalla, H. S. Shin, G. Eda, L.-J. Li, K. P. Loh and H. Zhang, *Nature Chemistry*, 2013, **5**, 263-275.
50. J. R. Schaibley, H. Yu, G. Clark, P. Rivera, J. S. Ross, K. L. Seyler, W. Yao and X. Xu, *Nature Reviews Materials*, 2016, **1**, 16055.
51. J. Goniakowski, F. Finocchi and C. Noguera, *Reports on Progress in Physics*, 2007, **71**, 016501.
52. J. Mannhart and D. G. Schlom, *Science*, 2010, **327**, 1607-1611.
53. D. Chimene, D. L. Alge and A. K. Gaharwar, *Advanced Materials*, 2015, **27**, 7261-7284.
54. H. Y. Hwang, Y. Iwasa, M. Kawasaki, B. Keimer, N. Nagaosa and Y. Tokura, *Nature Materials*, 2012, **11**, 103.
55. Q.-H. Wu, A. Fortunelli and G. Granozzi, *International Reviews in Physical Chemistry*, 2009, **28**, 517-576.
56. M. Osada and T. Sasaki, *Journal of Materials Chemistry*, 2009, **19**, 2503-2511.
57. P. Vogt, P. De Padova, C. Quaresima, J. Avila, E. Frantzeskakis, M. C. Asensio, A. Resta, B. Ealet and G. Le Lay, *Physical Review Letters*, 2012, **108**, 155501.
58. A. Acun, L. Zhang, P. Bampoulis, M. Farmanbar, A. van Houselt, A. N. Rudenko, M. Lingenfelder, G. Brocks, B. Poelsema, M. I.

Katsnelson and H. J. W. Zandvliet, *Journal of Physics: Condensed Matter*, 2015, **27**, 443002.
59. S. Cahangirov, M. Topsakal, E. Aktürk, H. Şahin and S. Ciraci, *Physical Review Letters*, 2009, **102**, 236804.
60. I. G. Buda, C. Lane, B. Barbiellini, A. Ruzsinszky, J. Sun and A. Bansil, *Scientific Reports*, 2017, **7**, 44766.
61. K. Takeda and K. Shiraishi, *Physical Review B*, 1994, **50**, 14916-14922.
62. M. Yi and Z. Shen, *Journal of Materials Chemistry A*, 2015, **3**, 11700-11715.
63. V. Nicolosi, M. Chhowalla, M. G. Kanatzidis, M. S. Strano and J. N. Coleman, *Science*, 2013, **340**, 1420-+.
64. Y. Hernandez, V. Nicolosi, M. Lotya, F. M. Blighe, Z. Y. Sun, S. De, I. T. McGovern, B. Holland, M. Byrne, Y. K. Gun'ko, J. J. Boland, P. Niraj, G. Duesberg, S. Krishnamurthy, R. Goodhue, J. Hutchison, V. Scardaci, A. C. Ferrari and J. N. Coleman, *Nature Nanotechnology*, 2008, **3**, 563-568.
65. J. Heising and M. G. Kanatzidis, *Journal of the American Chemical Society*, 1999, **121**, 638-643.
66. F. Torrisi, T. Hasan, W. Wu, Z. Sun, A. Lombardo, T. S. Kulmala, G.-W. Hsieh, S. Jung, F. Bonaccorso and P. J. Paul, *ACS Nano*, 2012, **6**, 2992-3006.
67. F. S. Wen, H. Hou, J. Y. Xiang, X. Y. Zhang, Z. B. Su, S. J. Yuan and Z. Y. Liu, *Carbon*, 2015, **89**, 372-377.
68. Y. H. Lee, X. Q. Zhang, W. J. Zhang, M. T. Chang, C. T. Lin, K. D. Chang, Y. C. Yu, J. T. W. Wang, C. S. Chang, L. J. Li and T. W. Lin, *Advanced Materials*, 2012, **24**, 2320-2325.
69. C. Zhao, H. Zhang, W. Si and H. Wu, *Nature Communications*, 2016, **7**, 12543.
70. J. Yuan, A. Balk, H. Guo, S. Patel, X. Zhao, Q. Fang, D. Natelson, S. Crooker and J. Lou, *arXiv preprint arXiv:1805.10372*, 2018.
71. X. Yin, X. Liu, Y.-T. Pan, K. A. Walsh and H. Yang, *Nano Letters*, 2014, **14**, 7188-7194.
72. X. Huang, S. Li, Y. Huang, S. Wu, X. Zhou, S. Li, C. L. Gan, F. Boey, C. A. Mirkin and H. Zhang, *Nature Communications*, 2011, **2**, 292.
73. Z. Sun, T. Liao, Y. Dou, S. M. Hwang, M.-S. Park, L. Jiang, J. H. Kim and S. X. Dou, *Nature Communications*, 2014, **5**.

74. S. Ithurria, M. D. Tessier, B. Mahler, R. P. S. M. Lobo, B. Dubertret and A. L. Efros, *Nature Materials*, 2011, **10**, 936.
75. H. Duan, N. Yan, R. Yu, C.-R. Chang, G. Zhou, H.-S. Hu, H. Rong, Z. Niu, J. Mao, H. Asakura, T. Tanaka, P. J. Dyson, J. Li and Y. Li, *Nature Communications*, 2014, **5**, 3093.
76. D. Chen, L. Peng, Y. Yuan, Y. Zhu, Z. Fang, C. Yan, G. Chen, R. Shahbazian-Yassar, J. Lu, K. Amine and G. Yu, *Nano Letters*, 2017, **17**, 3907-3913.
77. Q. Wang, J. Pan, M. Li, Y. Luo, H. Wu, L. Zhong and G. Li, *Journal of Materials Science & Technology*, 2015, **31**, 630-633.
78. Y. Sun, Z. Sun, S. Gao, H. Cheng, Q. Liu, J. Piao, T. Yao, C. Wu, S. Hu and S. Wei, *Nature communications*, 2012, **3**, 1057.
79. Y. Liu, H. Cheng, M. Lyu, S. Fan, Q. Liu, W. Zhang, Y. Zhi, C. Wang, C. Xiao and S. Wei, *Journal of the American Chemical Society*, 2014, **136**, 15670-15675.
80. C. A. Geiger, *Solid Solutions in Silicate and Oxide Systems*, The Mineralogical Society of Great Britain and Ireland, 2001.
81. M. Grätzel, *Nature*, 2001, **414**, 338.
82. A. Fujishima and K. Honda, *Nature*, 1972, **238**, 37-38.
83. M. Ge, Q. Li, C. Cao, J. Huang, S. Li, S. Zhang, Z. Chen, K. Zhang, S. S. Al-Deyab and Y. Lai, *Advanced Science*, 2017, **4**, 1600152.
84. M. Pelaez, N. T. Nolan, S. C. Pillai, M. K. Seery, P. Falaras, A. G. Kontos, P. S. Dunlop, J. W. Hamilton, J. A. Byrne and K. O'shea, *Applied Catalysis B: Environmental*, 2012, **125**, 331-349.
85. S. B. Rawal, S. Bera, D. Lee, D.-J. Jang and W. I. Lee, *Catal. Sci. Technol.*, 2013, **3**, 1822-1830.
86. B. F. Machado and P. Serp, *Catal. Sci. Technol.*, 2012, **2**, 54-75.
87. X.-K. Kong, C.-L. Chen and Q.-W. Chen, *Chemical Society Reviews*, 2014, **43**, 2841-2857.
88. Y. Jia, L. Zhang, A. Du, G. Gao, J. Chen, X. Yan, C. L. Brown and X. Yao, *Advanced Materials*, 2016, **28**, 9532-9538.
89. Y.-W. Son, M. L. Cohen and S. G. Louie, *Nature*, 2006, **444**, 347.
90. M. H. Gass, U. Bangert, A. L. Bleloch, P. Wang, R. R. Nair and A. K. Geim, *Nature Nanotechnology*, 2008, **3**, 676.
91. I.-Y. Jeon, H.-J. Choi, M. Choi, J.-M. Seo, S.-M. Jung, M.-J. Kim, S. Zhang, L. Zhang, Z. Xia and L. Dai, *Scientific Reports*, 2013, **3**, 1810.

92. J. Zhang and L. Dai, *Angewandte Chemie International Edition*, 2016, **55**, 13296-13300.
93. M. A. Lukowski, A. S. Daniel, F. Meng, A. Forticaux, L. Li and S. Jin, *Journal of the American Chemical Society*, 2013, **135**, 10274-10277.
94. D. Voiry, M. Salehi, R. Silva, T. Fujita, M. Chen, T. Asefa, V. B. Shenoy, G. Eda and M. Chhowalla, *Nano Letters*, 2013, **13**, 6222-6227.
95. Z. Wu, B. Fang, A. Bonakdarpour, A. Sun, D. P. Wilkinson and D. Wang, *Applied Catalysis B: Environmental*, 2012, **125**, 59-66.
96. Y. Yu, S.-Y. Huang, Y. Li, S. N. Steinmann, W. Yang and L. Cao, *Nano letters*, 2014, **14**, 553-558.
97. H. Wang, C. Tsai, D. Kong, K. Chan, F. Abild-Pedersen, J. K. Nørskov and Y. Cui, *Nano Research*, 2015, **8**, 566-575.
98. Y. C. Lin, D. O. Dumcenco, H. P. Komsa, Y. Niimi, A. V. Krasheninnikov, Y. S. Huang and K. Suenaga, *Advanced Materials*, 2014, **26**, 2857-2861.
99. H. L. Zhuang and R. G. Hennig, *Physical Review B*, 2013, **88**, 115314.
100. J. Chao, Z. Xie, X. Duan, Y. Dong, Z. Wang, J. Xu, B. Liang, B. Shan, J. Ye and D. Chen, *CrystEngComm*, 2012, **14**, 3163-3168.
101. N. A. Spaldin, *Magnetic Materials: Fundamentals and Applications*, Cambridge University Press, 2010.
102. R. G. Parr, in *Horizons of Quantum Chemistry*, Springer, 1980, pp. 5-15.
103. M. Bonilla, S. Kolekar, Y. Ma, H. C. Diaz, V. Kalappattil, R. Das, T. Eggers, H. R. Gutierrez, M.-H. Phan and M. Batzill, *Nature Nanotechnology*, 2018, **13**, 289-293.
104. B. Huang, G. Clark, E. Navarro-Moratalla, D. R. Klein, R. Cheng, K. L. Seyler, D. Zhong, E. Schmidgall, M. A. McGuire, D. H. Cobden, W. Yao, D. Xiao, P. Jarillo-Herrero and X. Xu, *Nature*, 2017, **546**, 270.
105. N. D. Mermin and H. Wagner, *Physical Review Letters*, 1966, **17**, 1133.
106. O. V. Yazyev and L. Helm, *Physical Review B*, 2007, **75**, 125408.
107. Y. Ma, Y. Dai, M. Guo, C. Niu, Y. Zhu and B. Huang, *ACS nano*, 2012, **6**, 1695-1701.
108. X.-L. Fan, Y.-R. An and W.-J. Guo, *Nanoscale Research Letters*, 2016, **11**.

109. *Nature Nanotechnology*, 2018, **13**, 269-269.
110. J. G. Park, *Journal of Physics-Condensed Matter*, 2016, **28**, 3.
111. K. M. H. Young, B. M. Klahr, O. Zandi and T. W. Hamann, *Catal. Sci. Technol.*, 2013, **3**, 1660-1671.
112. P. García-Muñoz, G. Pliego, J. A. Zazo, A. Bahamonde and J. A. Casas, *Journal of Environmental Chemical Engineering*, 2016, **4**, 542-548.
113. K. Y. Guslienko, V. Novosad, Y. Otani, H. Shima and K. Fukamichi, *Physical Review B*, 2001, **65**, 024414.
114. R. Dittrich, T. Schrefl, M. Kirschner, D. Suess, G. Hrkac, F. Dorfbauer, O. Ertl and J. Fidler, *IEEE Transactions on Magnetics*, 2005, **41**, 3592-3594.
115. Ö. Erik, B. A. Unnar, M. Emil, K. Vassilios, K. P. Gunnar, Y. S. Alexander, A. V. Marc, K. Florian, P. Evangelos Th, S. F. Charles and H. Björgvin, *New Journal of Physics*, 2014, **16**, 053002.

Chapter 2

Experimental

Any experimental investigation requires precise characterization before the results are interpreted in-order to avoid spurious inferences. A proper characterization using sophisticated analytical techniques is a prerequisite in material research. This chapter discusses the working principle of synthesis techniques and analytical methods employed for characterization of prepared samples in this investigation.

2.1 X-Ray Diffraction

X-ray diffraction is one of the frequently employed non-destructive techniques by scientists to determine the crystalline nature of all range of materials.[1] The schematic of the geometry of an X-ray diffractometer is shown in ***Figure. 2.1***. The entire system can be divided into three major sections namely X-ray source, specimen, and detector. All these components lie on the circumference of an imaginary circle known as the focusing circle. The angle between the plane of specimen and incident X-ray is θ, whereas, the angle between the projection of X-ray source and the detector is 2θ. For this reason, the X-ray diffraction pattern obtained using this particular geometry is called θ-2θ scan and is the most generally used geometry.

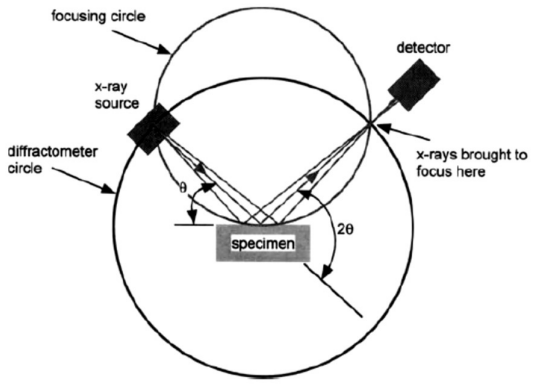

Figure. 2.1. The geometry of X-Ray Diffractometer (adapted from Dorset, D., Microscopy and Microanalysis 4(5): 513-515(1998))[1]

From the figure, it can be seen that the radius of the focusing circle is not a constant and it depends on the 2θ value. It increases as the 2θ value decreases. The range of θ value depends upon the crystal structure of the material under investigation. In general, the range of value of 2θ used is $15^0 - 70^0$.

From the geometry of the diffractometer, we could define another imaginary circle known as diffractometer circle/goniometer circle. The

diffractometer circle is defined in such a way that the specimen is located at the centre with the source and detector at the circumference. Hence the radius of the circle is a constant unlike focusing circle having a variable diameter.

Principle:

Consider the X-ray diffraction given in the ***Figure. 2.2***. The incident and diffracted X-rays make an angle θ with the planes at which it undergoes diffraction.

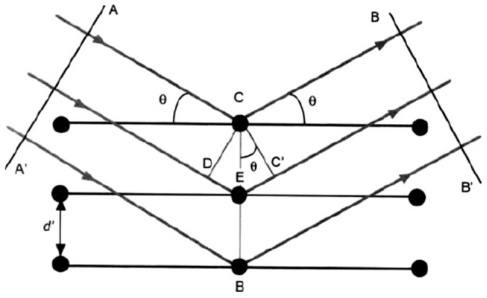

Figure. 2.2. X-ray diffraction from adjacent planes of a crystal. (Adapted from Dorset, D., Microscopy and Microanalysis 4(5): 513-515(1998))[1]

Now the condition for constructive interference of diffracted X-rays from adjacent planes is that the path difference (δ) between the wavefronts AA' and BB' for the rays shown must be an integral multiple of the wavelength of X-ray, λ.

$$\delta = n\lambda$$

where n is an integer. Now consider the wave frontsCC' and CD, the path difference δ is given by,

$$\delta = DE + EC' = 2EC'$$

$$\delta = 2CE \ \sin\theta$$

Since CE is the interplanar spacing d',

$$\delta = 2d' \sin\theta$$

Substituting the value of δ required for constructive interference,

$$n\lambda = 2d' \sin\theta \qquad (2.1)$$

Equation 2.1 is called Bragg's law and is the fundamental equation of X-ray diffraction. n is the order of diffraction and it can be an integer (n = 1,2,3…..). Hence for the first order diffraction (n = 1), the Bragg's law can be written as (equation 2.2),

$$\lambda = 2d' \sin\theta \qquad (2.2)$$

Those X-rays which satisfies the Bragg Equation (equation 2.1) undergoes constructive interference and a peak in intensity occurs. A detector collects these signals to give an output in counts. This output signal is plotted against the corresponding *2θ* value to obtain the X-diffraction spectrum. Each and every material has its own characteristic X-ray diffraction spectrum which enables researchers to identify a given material by analyzing its diffraction peaks.

2.2 X-Ray Photoelectron Spectroscopy

X-Ray Photoelectron Spectroscopy (XPS) is a surface sensitive technique which can be employed to obtain quantitative and chemical state information of a specimen.[2] The fundamental equation governing the working of XPS is 'photo-chemical quantum equivalent law' which is based on Einstein's photoelectric effect, and is given by equation 2.3,

$$h\vartheta = E_{bind} + E_{kin} + \Phi \qquad (2.3)$$

This equation summarizes the interaction of electromagnetic radiation of frequency ϑ on a metallic surface having a binding energy of E_{bind} and a work function, Φ. For the electromagnetic radiation to effect an electron ejection from the metallic surface having a kinetic energyE_{kin}, the radiation should have sufficient energy to overcome the binding energy (E_{bind}) of the metal and the work function (Φ). The work function (Φ) is the energy required for the photoelectron to transfer from Fermi level to the vacuum level. The ejected electron is known as photoelectron. The energy level diagram of electron emission in XPS is shown in ***Figure. 2.3***.

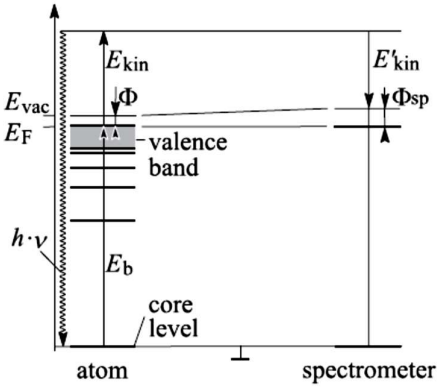

Figure. 2.3. Energy level diagram of photoelectron emission (Adapted from *Pleul, D. and F. Simon, X-ray photoelectron spectroscopy, Springer: 71-89(2008)*)[2].

A basic XPS consists of three major parts- a sample chamber to which the X-ray source is attached, photoelectron trajectories with a hemispherical analyzer and the detector assembly (***Figure 2.4***).

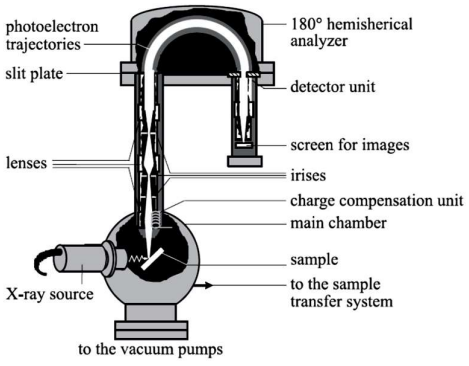

Figure. 2.4. A typical X-ray photoelectron spectrometer (Adapted from *Pleul, D. and F. Simon, X-ray photoelectron spectroscopy, Springer: 71-89(2008)*)[2].

All these parts are connected to a vacuum pump provided with a sample load-lock. The base pressure

during analysis should be less than 10^{-8} mbars in order to avoid partial loss of photoelectrons due to scattering with gas molecules. The photoelectrons ejected by X-ray are forced to follow a hemispherical path in a hemispherical analyzer by applying an appropriate electric field before reaching the counter. The motion of photoelectrons depends on the applied field strength as well as its kinetic energy. This provides a suitable mechanism to separate and analyze photoelectrons with different kinetic energies. The photoelectrons reaching the counter is monitored for a definite interval of time. The plot of the obtained count rate measured in cps (counts per second) in the y-axis against the binding energy in the x-axis gives the XPS spectrum. By analyzing the binding energy and intensity of photoelectron peaks, the elemental identity, chemical state, and quantity of an element could be accurately determined.

2.3 Scanning Electron Microscopy

The scanning electron microscope (SEM) is used to study the surface morphology of samples from micrometric (μm) to nanometric (nm) scales.[3] In a typical SEM (see the schematic in ***Figure 2.5***), the specimen to be analyzed is irradiated with a finely focused electron beam (100 eV to 30 keV) which raster scan across the surface of the specimen to obtain images or the analysis at the given position.

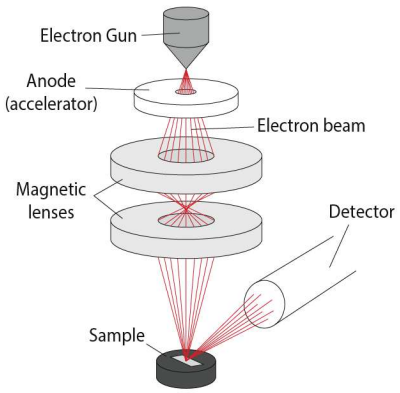

Figure. 2.5. A schematic of the scanning electron microscope (Adapted from https://www.eng-atoms.msm.cam.ac.uk/)

The interaction of the electron beam with the sample results in different signals viz. secondary electrons (SE), back-scattered electrons (BSE), characteristic X-rays and other photons of varying energy. These signals can be used to obtain different characteristics of the sample such as surface topography, crystallography, and composition. Signals due to the secondary electrons (SE) and backscattered electrons (BSE) with most probable exit energies lying in the range of 2-5eV are of great importance owing to their capability to precisely probe surface topography.

Elemental Analysis: In SEM analysis, along with the aforementioned signal, characteristic X-rays are also emitted during the bombardment of the electron beam with the specimen. These X-rays can be analyzed to get both quantitative and qualitative information about the constituent elements of the specimen. This facility is called electron probe microanalyzer (EPMA) in general. This EPMA can be associated with an energy-dispersive spectrometer (EDS) as well as a wavelength-dispersive spectrometer (WDS) for monitoring the characteristic X-rays. EDS is used to measure characteristic X-rays from major elements (>10 wt%) in a specimen, whereas the WDS is used to measure characteristic X-rays from minor or even trace elements (<0.1 wt%).

2.4 Transmission Electron Microscopy

In a transmission electron microscope (TEM), the specimen is irradiated with an electron beam of energy 80-120kV having uniform current density.[4] A schematic illustration of the electron path in a typical transmission electron microscope is given in ***Figure 2.6***.

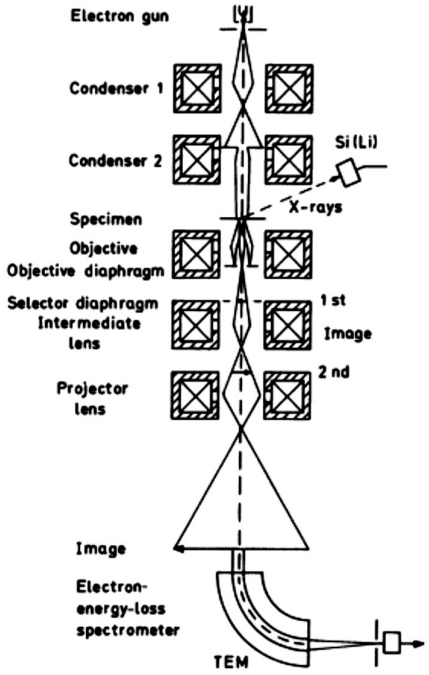

Figure. 2.6. A schematic of scanning electron microscope (Adapted from Reimer, Ludwig. *Transmission electron microscopy: physics of image formation and microanalysis*. Vol. 36. Springer, 2013)[4]

Electrons are generated by means of thermionic, Schottky, or field emission electron gun. Multiple condenser lens stages allow variation of illumination aperture as well as area of the specimen to be illuminated. The intensity distribution of transmitted electrons behind the specimen is focused onto a fluorescent screen with the assistance of three or four stage lens system to generate the image. The obtained image can be recorded either by direct exposure to a photographic emulsion or digitally by using a CCD camera.

Electrons interacting with a material may scatter either elastically or inelastically and also can produce a wide range of secondary signals and are shown in ***Figure 2.7***.

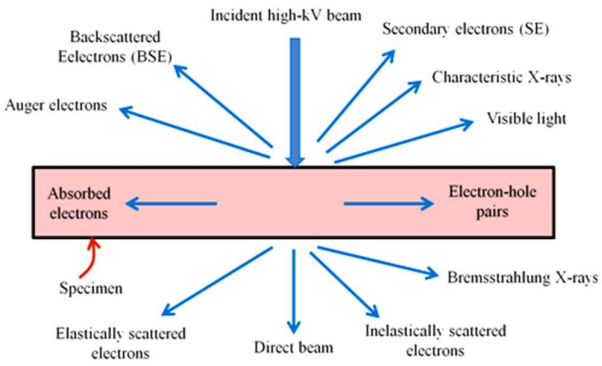

Figure. 2.7. Image highlighting the signals generated when a high-kV electron beam interacts with a material (Adapted from https://nptel.ac.in/)

Many of these signals are utilized for 'analytical electron microscopy (AEM)' using which we can obtain chemical information about the specimen. AEM uses X-ray energy dispersive spectrometry (XEDS) and electron energy loss spectrometry (EELS).

2.4.1 Conventional Modes of the TEM

Dark-Field and Bright-Field Imaging: ***Figure.2.8a*** shows the ray diagram of image formation in a conventional TEM (CTEM). The intermediate lens is focused on the image plane of the objective lens. Assuming all the rays are parallel to the optical axis before hitting the specimen, we can observe that the image formed is the combined output of all the transmitted and diffracted rays leaving the specimen at the viewing screen. In such a case, there is no contrast in the obtained image.

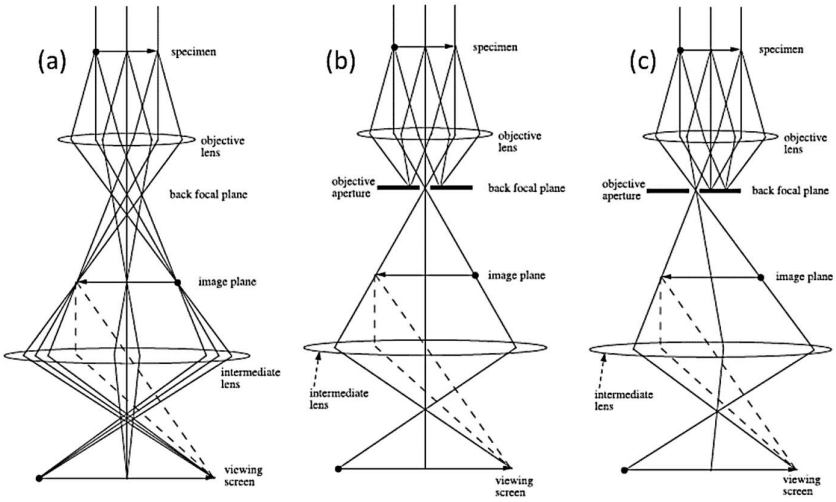

Figure. 2.8. Ray path in ***(a)*** aperture less image mode; ***(b)*** bright-field (BF) and, ***(c)*** dark-field (DF) modes (Adapted from Fultz, B. and Howe, J.M., 2012. *Transmission electron microscopy and diffractometry of materials.* Springer Science & Business Media)[5]

It should be noted here that each point in the back-focal plane of the objective lens contains rays from all parts of the specimen. To form the image of the specimen, rays passing through a single point at the back-focal plane of the objective lens is enough. Another speciality of the points in the back focal plane is that the rays passing through a particular point have all been scattered at a unique angle by the specimen. By appropriately positioning an 'objective aperture' at specific points of the back focal plane, the image can be formed out of electrons diffracted at a particular angle. Based on the aperture position, there are two imaging modes and are illustrated in ***Figure. 2.8b & c***.

- When the aperture is positioned to pass only the transmitted (un-diffracted) electrons, a bright-field (BF) image is formed.
- When the aperture is positioned to pass only some diffracted electrons, a dark field (DF) image is formed.

In CTEM studies of crystalline specimens, image features may be visible due to the 'diffraction contrasts'. Diffraction contrast implies to the variation of diffraction intensity across the specimen. The importance of imaging in BF or DF mode is because of the following reason; when there is an excess of diffracted intensity, there can be a large complementary loss of transmitted intensity thereby reducing the quality of the image. So either BF or DF alone will provide a better contrast image as compared to the aperture-less mode of imaging.

Selected Area Electron Diffraction: The ray path in SAED mode is shown in ***Figure. 2.9***. Here also, the intermediate lens is focused at the back-focal plane of the objective lens. However, unlike BF and DF modes, there is no aperture at the back-focal plane of the objective such that all the diffracted and transmitted electrons are imaged. A second aperture known as 'intermediate aperture' at the image plane of the objective lens, is deployed to confine the diffraction pattern to a specific selected area of the specimen. In order to obtain SAED from a specimen, the following steps are followed - the specimen is examined carefully in image mode to locate features of interest (indicated by the arrowhead in ***Figure.2.9***), introduce the intermediate aperture around this feature and switch the microscope to SAED mode to obtain the electron diffraction pattern.

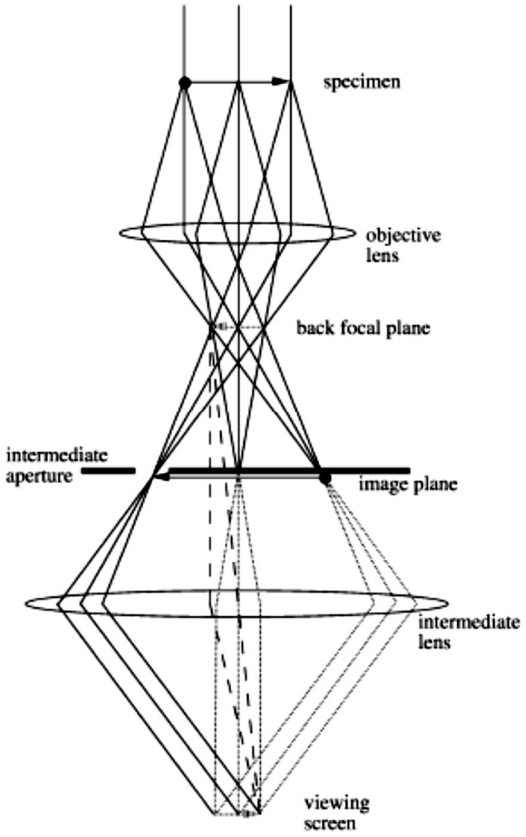

Figure. 2.9. Ray path in SAED mode (Adapted from Fultz, B. and Howe, J.M., 2012. *Transmission electron microscopy and diffractometry of materials.* Springer Science & Business Media)[5]

The separation of diffraction spots on the viewing screen can be used to determine the interplanar spacing (d) of the crystal under investigation.

We have the Bragg's law,

$$n\lambda = 2d \sin\theta$$

For lower order diffractions (θ~1^0) of 100kV (λ = 0.037 Å) electrons,

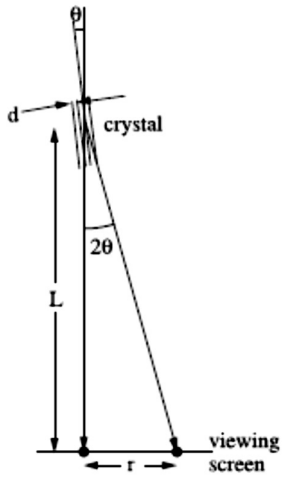

$$\sin\theta \sim \tan\theta \sim \frac{1}{2}\tan 2\theta$$

From Figure. 2.10,

$$\tan 2\theta = \frac{r}{L}$$

Figure. 2.10. Geometry for electron diffraction and definition of camera length, L.

Combining the above equations with Bragg's law,

$$\lambda = d\frac{r}{L}$$

$$\boldsymbol{rd = \lambda L} \qquad (2.4)$$

Equation 2.4 is known as 'camera equation'. It helps us to find out the interplanar spacing, *d* if we know the separation of diffraction spots, *r,* which can be determined from the SAED. The constant, λL, known as the "camera constant", is typical of a TEM and can be found on the console readout display of a modern TEM. Its units are usually in [Å cm].

High-Resolution Transmission Electron Microscope Imaging: Spatial resolution is of utmost importance in any microscopy. In the case of TEM, the ultimate resolution can be achieved by using a method known as 'High-Resolution TEM', simply HRTEM. Beyond diffraction contrast microscopy, as we discussed in CTEM, which measures the intensity of diffracted waves, in "HRTEM" the phase of the diffracted electron wave is preserved when it interferes constructively or destructively with the

transmitted wave. This technique of "phase-contrast imaging" is used to form images of columns of atoms.

HRTEM can be understood in terms of the phase of the electron wavefront and how this phase gets altered by the specimen and the objective lens. The theory of HRTEM based on Huygens principle is beyond the scope of this thesis and could be found elsewhere.[6] However, in order to obtain quantitative information about atomic arrangements in a specimen from HRTEM, computer simulations of the image are required. HRTEM could achieve a resolution smaller than 1 nm, using which one can see the periodic fringes, which represents the direct resolution of the Bragg's diffracting planes. The fringes that are visible in an HRTEM image originate from those planes that are oriented as Bragg's reflecting planes and, that possesses inter-planar spacing greater than the lateral spatial resolution of the TEM.

2.4.2 Analytical Electron Microscopy

Energy Dispersive Spectrometry: Energy Dispersive Spectrometry (EDS) analyzes the X-rays produced from the parts of the specimen as a result of interaction with the high energy electron beam using a solid state detector. These X-rays are characteristics of particular elements and is used to quantify the concentrations of different elements in the specimen.

Electron Energy-Loss Spectrometry: In Electron Energy-Loss Spectrometry (EELS), energy losses of the electrons are analyzed after the energetic electrons traverse through the specimen. Information on local chemistry and structure is obtained from features in EELS spectra caused by plasmon excitations and core electron excitations.

Energy Filtered Transmission Electron Microscopy: A CTEM uses all electrons that pass through the sample, but an instrument component known as an "energy filter" facilitates image formation with electrons that have undergone specific energy loss as it passes through the specimen. The technique of "energy-filtered TEM" (EFTEM), detects "chemical contrast" in specimens by adjusting an energy filter to pass electrons that have lost energy to ionization at the core level of selected elements. These "energy-filtered images" (EFI) can reveal chemical contrast with sub-nanometer spatial resolution.

2.4.3 Scanning Transmission Electron Microscope Imaging

In scanning transmission electron microscopy (STEM), a narrow (∼1–10 Å), focused beam of electrons is moved in a television-style raster pattern across the specimen. In synchronization with the raster scan, various data, such as emitted x-rays, secondary electrons, or backscattered electrons, are acquired from the specimen. Transmitted electrons are detected with a moveable detector at the bottom of the microscope column. The STEM mode of operation is especially useful for spectroscopy work since it permits the acquisition of a "chemical map" of the sample. An annular dark-field detector can also be used in the STEM mode of operation for high-angle annular dark-field (HAADF) (or "Z-contrast") imaging. This HAADF method uses incoherent elastic scattering of electrons to form images of atomic columns.

2.4.4 High-Angle Annular Dark-Field Imaging

"High-Angle Annular Dark-Field," or HAADF imaging (also called "Z-contrast imaging") is one of the emerging imaging techniques in transmission electron microscopy. The major difference of this technique as compared to CTEM and HRTEM is that HAADF images are formed using incoherent elastic scattered electrons. The phase difference of the interfering electron wavefronts are crucial for HRTEM whereas, these are irrelevant for HAADF.[5] Here each atom is considered as independent scatter and there involves no interference of phases of wavefunctions from different atoms. The HAADF images are the direct interpolation of atoms, types and positions in a specimen.

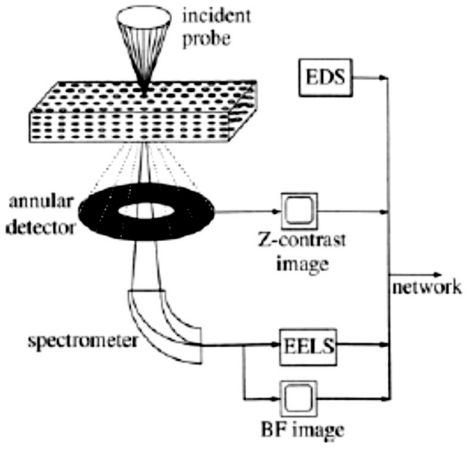

Figure. 2.11. Schematic of a STEM equipped with the annular detector and EELS spectrometer, arranged for HAADF imaging. (Adapted from Fultz, B. and Howe, J.M., 2012. *Transmission electron microscopy and diffractometry of materials.* Springer Science & Business Media)[5]

The images are formed by collecting high-angle (75–150 mrad) elastically-scattered electrons with an annular dark-field detector (***Figure.2.11***) and hence is considered to be an efficient device for dark-field imaging. The angle of scattering is an order-of-magnitude larger than for typical Bragg diffractions, and the relevant part of the scattering potential is an order-of-magnitude smaller than

typical atomic dimensions. The effective size of the atomic scattering potential (typically 0.01–0.03 nm) is also about an order-of-magnitude smaller than the size of the electron beam probe of modern medium-voltage field-emission STEMs (typically 0.15–0.2 nm). A vertical column of atoms can, therefore, be understood as a very sharp object in the plane of the sample.

2.5 Atomic Force Microscope

Atomic Force Microscope (AFM) relies on a scanning technique to produce very high-resolution 3-D images of sample surfaces. The AFM measures ultrasmall forces (less than 1 nN) present between the AFM tip surface and a sample surface.[7, 8] These small forces are measured by measuring the motion of a very flexible cantilever beam with an ultra-small mass given by equation 2.5.

$$\boldsymbol{F} = -k * \boldsymbol{s} \qquad (2.5)$$

Where k is the spring constant and $\boldsymbol{s}$ is the displacement of the cantilever.

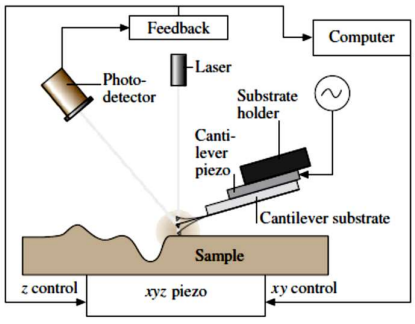

Figure. 2.12. Schematic of an AFM working in tapping mode/oscillating mode (Adapted from Bhushan, Bharat, and Othmar Marti. "Scanning probe microscopy–principle of operation, instrumentation, and probes." *Springer Handbook of Nanotechnology*. Springer, Berlin, Heidelberg, 2010. 573-617).[9]

Most AFMs can be used for topography measurements in the so-called tapping mode (intermittent contact mode)/oscillating mode, in

what is also referred to as dynamic force microscopy. A schematic is shown in ***Figure 2.12***.

There is a large number of dynamic operating modes, however, all of them are variations of a basic strategy. The cantilever is oscillated at its resonant frequency (70-400 kHz), with the help of an additional piezoelectric element mounted on it (equation 2.6).

$$\omega = \sqrt{\frac{k_{eff}}{m}} \qquad (2.6)$$

Where k_{eff} is the effective spring constant and m is the mass of the cantilever. On approaching the sample surface, the oscillation of the cantilever changes due to the interaction between the probe and the force field from the sample. The change in oscillation is monitored by the force transducer (i.e. by the optical lever in most AFMs) and is processed to obtain the image of the surface of the specimen. The scanner adjusts the z height via the feedback loop to maintain the probe at a fixed distance from the sample. The general principle of oscillating AFM modes is shown in ***Figure 2.13***.

Different imaging modes can also be interpreted in terms of the distance and force between the tip and the sample surface and are summarized in ***Figure. 2.13***. If we are using a small oscillation amplitude, we could keep the cantilever in an attractive regime having very low sample-tip forces. This mode is called non-contact AFM mode (denoted by A in ***Figure 2.13***).

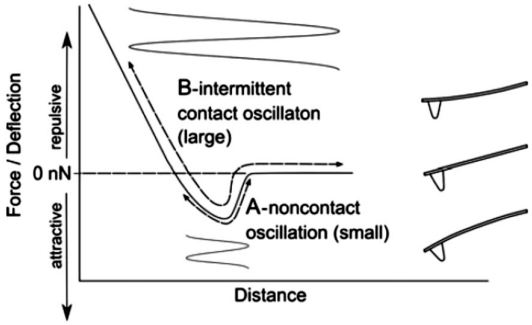

Figure. 2.13. Operating regimes of oscillating AFM mode (Adapted from Eaton, Peter, and Paul West. *Atomic force microscopy*. Oxford university press, 2010)[8]

On the other hand, if we are using a higher amplitude oscillation of the cantilever, the tip moves far away from the surface and the short-range attractive forces vanish. In this regime, long-range repulsive forces dominate and is called intermittent contact mode (denoted by B in ***Figure 2.13***). This mode involves large forces between the tip and surface which can be destructive but is easier to implement. Non-contact mode of AFM is preferred for biological and liquid samples over intermittent contact mode.

Magnetic Force Microscopy (MFM) is a modified version of AFM to measure the surface magnetic properties of a specimen.[10] In MFM, the standard silicon cantilever with a thin magnetic coating is used in order to probe local magnetic properties of the sample. Since magnetic force decay quickly with distance, MFM tip should be kept so close to the surface of the specimen so that it can directly probe the magnetic field distribution to generate the image. Typical materials used as magnetic coating are cobalt, cobalt-nickel and cobalt-chromium.[11]

2.6 Raman Spectroscopy

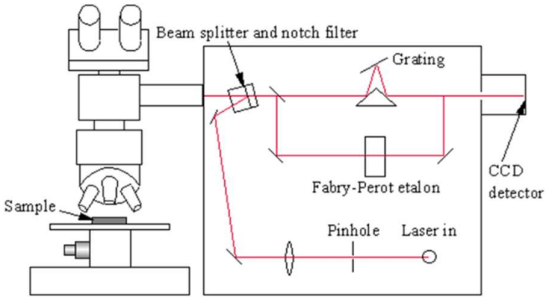

Figure. 2.14. Schematic of a Raman spectrometer (Adapted from chemguide.co.uk)

Raman spectroscopy is commonly used by scientists to obtain a structural fingerprint by which molecules can be identified. The underlying principle is 'Raman Scattering'- the change in frequency of scattered light on interacting with molecular vibrations.[12] By analyzing the molecular vibrations, we can identify the chemical composition and other important information about the material. Raman Effect is too weak (1 part of 10 million) to be detected by naked eye that we use an extremely sensitive spectrometer to analyze the scattered light. A schematic of the modern Raman spectrometer is given in the ***Figure. 2.14***.

At the molecular level, photons interact with matter by absorption or by scattering processes. Scattering can either be elastic, or inelastic, leading to Rayleigh scattering or Raman scattering. The perturbation of the electron clouds of the molecules by the electric field of the scattering photon excite the system to a 'virtual state'. The eventual exchange of energy between the system and the photon results in Raman scattering, subsequently bringing the system to a vibrational energy level above or below that of the initial state. The shift in frequency (due to loss or gain of energy) between the incident and scattered photon due to Raman scattering is termed the Raman shift. The shift in frequency can be either positive (up) or negative (down) depending on whether the system has lost

or gained vibrational energy during inelastic Raman scattering. The down-shifted components are called Stokes lines and the up-shifted components are termed anti-Stokes lines. Generally, Stokes lines are lesser in intensity and are neglected. A Raman spectrum is obtained by plotting the number of scattered photons detected versus Raman shift in the anti-Stokes regime as a result of the interaction with the specimen. Different materials have different vibrational modes, and therefore each of them has its own characteristic Raman spectra. This makes Raman spectroscopy a useful technique for material identification.

2.7 UV-Visible Absorption Spectroscopy

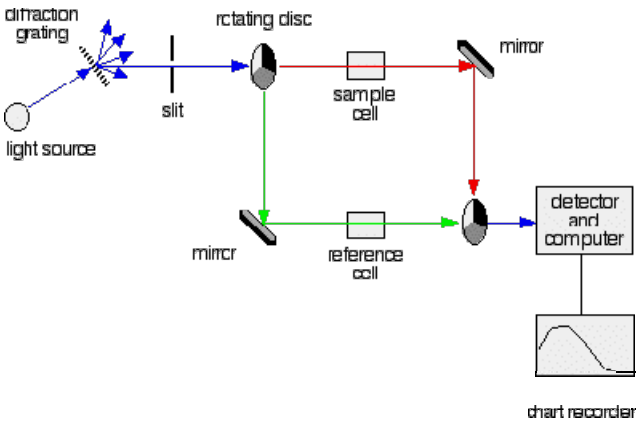

Figure. 2.15. Schematic of a UV-Visible spectrometer (Adapted from www.chm.bris.ac.uk)

The UV-Visible spectrophotometers are used to measure the absorbance of electromagnetic radiation in the ultraviolet (190-400nm) and the visible (400-800nm) region of the entire spectrum.[13] The technique can be used both qualitative and quantitative analysis of light absorption by a material under investigation. A schematic of the UV-Visible spectrometer is given in ***Figure. 2.15***. A light source generates visible and near ultraviolet light

having suitable bandwidth (200-800 nm) of the electromagnetic spectrum. After passing through a monochromator, the light beam is split into two by using a beam splitter which enables the passage of the light both through the specimen (sample cell) and the solvent (reference cell) kept inside a cuvette.

For each wavelength, the intensity of light passing through the reference cell (I_0) and the sample cell (I) is measured. Ideally, I will be always less than I_0 since the specimen absorbs some portion of light while passing through it. Then the absorbance (A) of the sample is given by equation 2.7,

$$A = log_{10}\frac{I_0}{I} \qquad (2.7)$$

The detector converts the incoming light into a current proportionally. The chart recorder usually plots the absorbance against wavelength (nm) in the UV and visible section of the electromagnetic spectrum. From the absorption spectrum obtained, we can determine the bandgap of the specimen by using suitable methods. Tauc et al.[14] proposed and substantiated a method for determining the band gap using optical absorbance data plotted appropriately with respect to energy. This was further improvised by Davis in their work on amorphous semiconductors.[15]

It was shown that the optical absorption strength depends on the difference between the photon energy and the band gap as follows (equation 2.8):

$$(\alpha h\vartheta)^{\frac{1}{n}} = A(h\vartheta - E_g) \qquad (2.8)$$

where h is Planck's constant, ϑ is the photon's frequency, α is the absorption coefficient, E_g is the band gap energy – the energy required for an electron to get excited from valance band maximum to the conduction band minimum, and A is a proportionality constant. The value of the exponent (n) denotes the nature of the electronic transition, whether allowed or forbidden and whether direct or indirect. Typically, the allowed transitions dominate the basic absorption processes, giving either n=1/2 for direct and n=2 for indirect transitions.

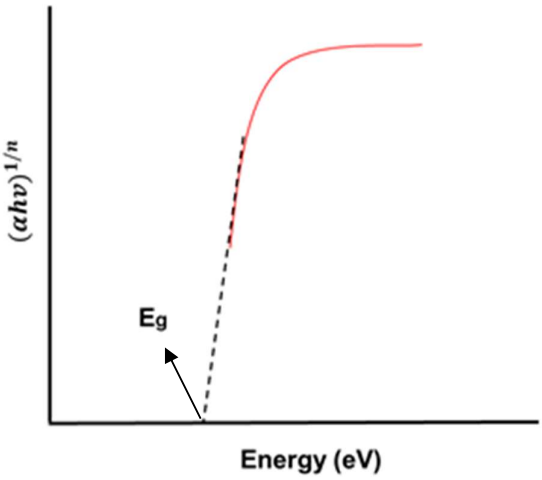

Figure. 2.16. A typical Tauc plot for the determination of bandgap energy

Thus, the basic procedure for a Tauc analysis is to acquire optical absorbance data for the specimen under investigation that spans a range of energies including the band edge. Plotting $(\alpha h\vartheta)^{\frac{1}{n}}$ versus $(h\vartheta)$ with n equals either 1/2 or 2 to see which provides the better fit and thus identifies the correct transition type. An extrapolation of the linear portion of the Tauc plot to the x-axis will give the bandgap energy of the specimen (***Figure 2.16***).

2.8 SQUID Magnetometer

The superconducting quantum interference device (SQUID) is the most sensitive instrument available for measuring magnetic fields. SQUID consists of two superconducting magnets separated by a very thin insulating layer to form two parallel Josephson junctions (see ***Figure.2.17*** for schematic).

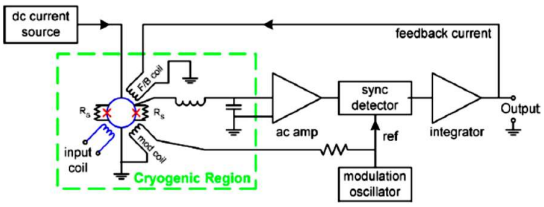

Figure. 2.17. Schematic of a typical dc SQUID magnetometer (Adapted from Fagaly, R. L. "Superconducting quantum interference device instruments and applications." *Review of scientific instruments*77.10 (2006): 101101)[16]

SQUID can be configured in such a way that it can measure small magnetic fields (~10^{-15} T).[16] The underlying principle of a SQUID magnetometer is Josephson Effect.[17, 18]

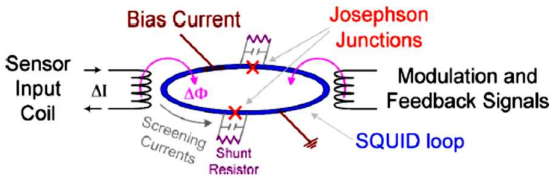

Figure. 2.18. A dc SQUID loop having two Josephson junctions (Adapted from Fagaly, R. L. "Superconducting quantum interference device instruments and applications." *Review of scientific instruments*77.10 (2006): 101101)[16]

The Josephson effect is the phenomenon of supercurrent,[19] a current that flows indefinitely long without any voltage applied, across a device known as a Josephson junction (JJ), which consists of two or more superconductors coupled by a weak link.

Typically, SQUID is a superconducting circular ring interrupted by means of two parallel JJs (***Figure. 2.18***). The enhanced sensitivity of a SQUID is achieved on account of the ability of parallel JJs to accurately probe even a change in magnetic field associated with one flux quantum, defined as (equation 2.9);

$$\emptyset_0 = \frac{2\pi\hbar}{2e} = 2.0678 \text{ x } 10^{-15}T \qquad (2.9)$$

Measurement in a SQUID is performed by moving the sample through the superconducting detection coil having JJs. Keeping a constant current, any minute change in magnetic flux in the SQUID loop by the movement of the sample could be probed by the corresponding voltage oscillations across the junctions. This change in voltage across the JJs proportional to the change in flux can be manipulated by appropriate electronics to obtain the magnetization of the specimen.

2.9 Magnetron Sputtering

Sputtering is a reliable and widely used method for thin-film deposition. It is used for obtaining controlled growth of thin films on a substrate with a good degree of purity. Sputtering involves introducing a controlled flow of a gas, usually chemically inert argon, into an evacuated chamber (typically better than 10^{-8} mbar), and electrically energizing a cathode to establish a self-sustaining plasma.[20] The exposed surface of the cathode, known as the target, is a thick circular slab of the material to be coated onto the substrates. The inert gas forms a plasma of positively charged ions by losing electrons on applying the potential, and are then accelerated towards the target and strike with a tremendous amount of kinetic energy

to eject atoms or molecules of the target material. This sputtered materials having sufficient energy eventually traverses across the chamber and hits the substrate at the other end, sticking to it as a coating or "thin film". The path of these charged ions could be suitably controlled by deploying magnets in the sputter guns as shown in the schematic (***Figure. 2.19***) below.

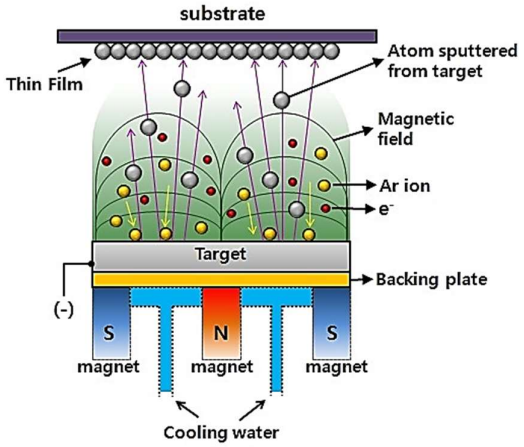

Figure. 2.19. Schematic of a dc magnetron sputtering.

In order to get good film adhesion, it is necessary for the substrate surface to be ultra-clean. Appropriate cleaning and handling steps must be employed prior to loading the substrates inside the chamber. Depending upon the type of material to be coated, viz. conducting or non-conducting, respectively, dc or rf sources are used to power the sputter gun.

2.10 References

1. D. Dorset, *Microscopy and Microanalysis*, 1998, **4**, 513-515.
2. D. Pleul and F. Simon, in *Polymer Surfaces and Interfaces*, Springer, 2008, pp. 71-89.
3. J. I. Goldstein, D. E. Newbury, J. R. Michael, N. W. Ritchie, J. H. J. Scott and D. C. Joy, *Scanning electron microscopy and X-ray microanalysis*, Springer, 2017.
4. L. Reimer and T. Mulvey, *Measurement Science and Technology*, 1994, **5**, 1183.
5. B. Fultz and J. M. Howe, *Transmission electron microscopy and diffractometry of materials*, Springer Science & Business Media, 2012.
6. D. B. Williams and C. B. Carter, in *Transmission electron microscopy*, Springer, 1996, pp. 3-17.
7. B. Bhushan and O. Marti, in *Nanotribology and Nanomechanics*, Springer, 2017, pp. 33-93.
8. P. Eaton and P. West, *Atomic force microscopy*, Oxford University Press, 2010.
9. B. Bhushan, *Springer handbook of nanotechnology*, Springer Science & Business Media, 2010.
10. U. Hartmann, *Annual review of materials science*, 1999, **29**, 53-87.
11. L. Abelmann, S. Porthun, M. Haast, C. Lodder, A. Moser, M. E. Best, P. J. van Schendel, B. Stiefel, H. J. Hug and G. P. Heydon, *Journal of magnetism and magnetic materials*, 1998, **190**, 135-147.
12. N. Colthup, *Introduction to infrared and Raman spectroscopy*, Elsevier, 2012.
13. H.-H. Perkampus, *UV-VIS Spectroscopy and its Applications*, Springer Science & Business Media, 2013.
14. J. Tauc, R. Grigorovici and A. Vancu, *physica status solidi (b)*, 1966, **15**, 627-637.
15. E. A. Davis and N. F. Mott, *The Philosophical Magazine: A Journal of Theoretical Experimental and Applied Physics*, 1970, **22**, 0903-0922.
16. R. Fagaly, *Review of scientific instruments*, 2006, **77**, 101101.
17. R. Jaklevic, J. Lambe, A. Silver and J. Mercereau, *Physical Review Letters*, 1964, **12**, 159.

18. B. D. Josephson, *Physics Letters*, 1962, **1**, 251-253.
19. B. D. Josephson, *Reviews of Modern Physics*, 1974, **46**, 251.
20. P. J. Kelly and R. D. Arnell, *Vacuum*, 2000, **56**, 159-172.

Chapter 3

Hematene – A new 2D Material from non-layered precursor Hematite: Synthesis, Properties and Applications

Natural iron ore hematite (α-Fe_2O_3) is abundant in rocks and soils and is the oldest known iron oxide mineral ever formed on earth. Naturally occurring hematite could be an ideal precursor material for deriving high quality 2D material. This chapter describes the exfoliation of hematite into its 2D counterpart christened 'hematene' and investigations on the magnetism of hematene sheets. The visible light photocatalytic activity of hematene is also carried out by forming a heterojunction with prolific photocatalyst titania (TiO_2). These details are also included in this chapter.

Nature Nanotechnology *13(7): 602-609*

3.1 Introduction

Iron oxides and their derivatives are unique due to their widespread applications in diverse fields including catalysis[1, 2], sensing[3] and magnetic storage media.[11] Hematite (α-Fe_2O_3) is abundant, inexpensive and highly sought after for environmental and energy applications.[4, 5] Hematite exhibits a corundum structure belonging to the D^6_{3d} space group with iron atoms octahedrally surrounded by six oxygen atoms. It is an n-type semiconductor and a well-known antiferromagnet with a Neel temperature (T_N) of 961 K.[6] It undergoes a transition from a weak ferromagnetic (WF) to an antiferromagnetic (AF) phase called Morin transition at 265 K.[7]

Two dimensional (2D) layers of hematite can be exfoliated from its natural ore, belonging to the lamellar specularite variety. These ores are characterized by a lamellar structure with large grain size.[8] Highly oriented large crystals of hematite, with in-and-out of the plane lamella evolved by slow cooling, is an ideal precursor to derive high-quality 2D monolayers – hereafter called 'hematene'. Successful exfoliation of hematene would pave way for new and exotic non-van der Waals 2D solids.

Hematite structure consists of alternating layers of iron and oxygen stacked along [001] axis of the hexagonal unit cell. Below Neel temperature, the alternating iron layers couple antiferromagnetically such that the net magnetization is nullified. But, on exfoliation, that is confining it to ultra-thin 2D layers of hematene may significantly influence the magnetic ordering. The establishment of preferred orientations on

exfoliation will also help in explaining the modified magnetism in such 2D materials. It is envisaged that hematene would induce ferromagnetic order from room temperature down to low temperature (2 K) resulting from suppression of the Morin transition. Such an evolution of FM ordering in hematene could be of interest from a theoretical perspective. For comprehensive understanding, calculations based on density functional theory (DFT) are performed and correlated with experimental results. Also, fully atomistic reactive molecular dynamics (MD) simulations serve as a useful tool to verify the preferred emergence and stability of certain crystallographic planes. Moreover, Hematite has a suitable bandgap for visible solar energy assisted water splitting applications.[4] However, the favourable bandgap energy of hematite for photocatalytic applications are overshadowed by poor carrier transport properties leading to higher recombination of photo-generated charge carriers thereby hindering its huge potential. Two-dimensional morphology of hematene could overcome this shortcoming which enables it to be an excellent material for unassisted photocatalytic water splitting applications.

3.2 Experimental

Liquid exfoliation of hematite into hematene:

The hematite ore used for exfoliation is an electron-probe microanalysis (EPMA) natural mineral standard, provided by the EPMA laboratory in the Earth Science Department, Rice University, Houston, TX, USA. The composition of the hematite standard is Fe_2O_3 = 99.82%, Al_2O_3 = 0.14%, by weight. This ore of hematite was ground into a fine powder using mortar and pestle with acetone as a wetting medium. The fine powdering

helps in dispersing the bulk material for easier exfoliation. 50 mg of the powder was dispersed in 200 mL of N, N-dimethylformamide and sonicated in a bath sonicator for 50 hours. The hematene sheets were separated by centrifugation at relative centrifugal force (RCF) value of 10196 (x g) in a Thermo Scientific Sorvall Legend X1R centrifuge for 30 minutes, and the supernatant liquid was filtered to obtain a few milligrams of hematene. Subsequent characterizations were performed on these 2D sheets. A schematic of the exfoliation process is given in ***Figure 3.1***.

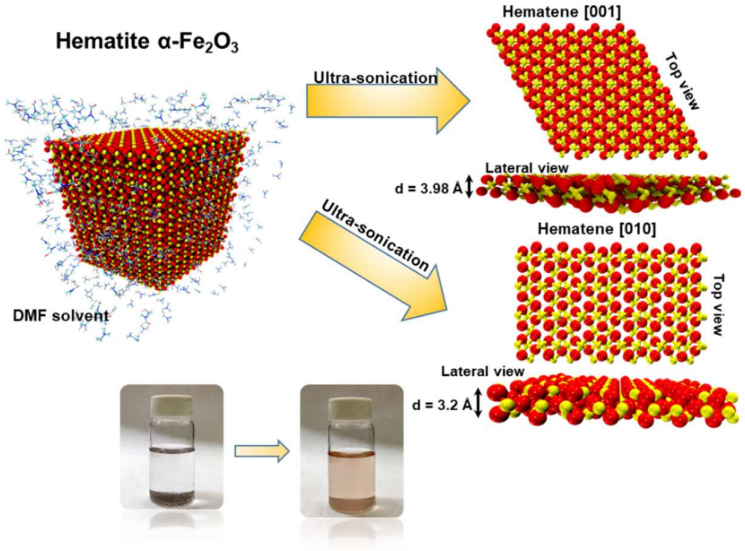

Figure 3.1 Liquid-phase exfoliation of Hematite to Hematene: Schematic of the exfoliation of bulk hematite in N, N-dimethylformamide (DMF) to hematene. Hematite is exfoliated in two different crystallographic planes. The plane spacing and atomic arrangement in these two crystallographic planes are illustrated, where the red spheres correspond to oxygen and yellow spheres correspond to iron. The optical image shows bulk hematite which sediments and the exfoliated hematene, which stays well dispersed in DMF. The reddish-brown colour of hematene is due to its absorbance in the visible region.

Analytical Tools:

The transmission electron micrographs and HRTEM images were obtained at 200 kV with an advanced TEM (JEOL ARM200F, JEOL Co. Ltd.), equipped with a cold field-emission gun and a CETCOR image corrector (CEOS Co. Ltd.). Raman microscopy measurements were carried out in a Renshaw inVia Raman microscope with a 50x objective using He-Ne laser of wavelength 632.8 nm with a spot size of 1µ. Scanning electron micrographs were acquired with an FEI Quanta high-resolution microscope. PHI Quantera XPS was used for analysis of elemental composition in the samples. Photoluminescence (PL) Spectra was recorded on a Horiba Nanolog Spectrofluorometer. UV-Visible absorption measurements were performed on a Shimadzu 2450 UV-Visible spectrophotometer in the range of 190-800 nm. A magnetic property measurement system (MPMS 3) by Quantum Design was used to measure the magnetic properties. The quantitative analysis of hematene was carried out at Rice University, Department of Earth Science on a Jeol JXA 8530F Hyperprobe (Field Emission Electronprobe Micro-Analyzer) using 5 wavelength dispersive spectrometers (WDS). Analytical conditions employed were: 15 kV acceleration voltage, 20 nA beam current, <1-micron beam size, 20 seconds counting time per element (10 seconds for peak and 5 seconds for each lower and upper background, respectively). The standard calibration for oxides used Fe metal for Fe (Kα), rutile for Ti (Kα), diopside for Si (Kα) and periclase for O (Kα). The ZAF matrix correction method was employed for quantification.

Formation of hematene/TiO_2 heterojunction and photocatalytic measurements:

Titanium foils (0.25 mm thickness, 99.7% pure, Sigma-Aldrich) were ultrasonically cleaned with a soap solution followed by acetone and isopropyl alcohol for 5 min each and dried in a nitrogen jet. The anodization was performed in a two-electrode electrochemical cell with titanium foil as the working electrode (anode) and platinum (Pt) foil as the counter electrode (cathode) under a constant voltage of 55 V at room temperature, in ethylene glycol electrolyte which contains 3 vol% of deionized water and 0.3 wt% of NH_4F. After completing the anodization process, the TiO_2 nanotubes film was ultrasonically cleaned in isopropyl alcohol for 3 to 5 minutes to remove the debris on the top of the nanotubes. The samples were annealed at 530 ˚C for 3 hours in an oxygen atmosphere. The 2D Fe_2O_3 nanosheets (hematene) were coated on nanotube films by drop casting until its colour turned into brick-red. The Fe_2O_3 loaded nanotube samples were heated at 200 °C for 20 minutes to remove the surface adsorbed organic compounds.

The photocurrent measurements were carried out using photoelectrochemical (PEC) cells in a three electrode mode using a CH instrument (model 660C) electrochemical analyzer. Na_2SO_4 (0.5 M) was used as the electrolyte. The hematene/titania (TNT) film, Ag/AgCl and Pt foil were used as the working, reference and counter electrodes respectively. A Newport (Model No: 67005) xenon arc lamp source fitted with an AM 1.5 G filter was used for illumination. The output intensity was kept at 100 mW/cm^2 using a National Renewable Energy Laboratory (NREL) calibrated silicon solar cell. The Mott-Schottky measurements

were also performed in a three-electrode configuration under dark conditions at a frequency of 1000 Hz in 0.5 M Na_2SO_4. The incident photon to current conversion efficiency (IPCE) was measured using a setup consisting of Newport monochromator (Newport, Model No: 74125) and power meter and a two-electrode PEC cell configuration consisting of a bare or hematene loaded titania nanotube photoanode and a platinum cathode.

3.3 2D morphology of Hematene

Bright-field transmission electron microscopy (TEM) (***Figure 3.2a (i)&(ii)***) at two different magnifications confirms exfoliation and formation of mono/bilayer hematene**.** From the high-resolution scanning TEM (HRSTEM) (***Figure 3.2a(iii) & 3.2b***), it can be deduced that there are two different exfoliation planes resulting in monolayers with orientations in [001] and [010] directions corresponding to (001) and (010) planes. These images and corresponding Fourier transforms (inset) illustrate the hexagonal symmetry of hematene with lattice parameters a= 5.0356 Å and c=13.7489 Å described with respect to the hematite parent phase. The structural model developed using the high-resolution images (***Figures 3.2a & 3.2b***), where yellow spheres denote iron ions at octahedral voids and red spheres denote oxygen ions, explicitly show the difference in arrangement of atoms in the two planes. The plane and cross-sectional view of the MD simulated hematene (001) and (010) planes have a thickness of 3.98 Å and 3.2Å, respectively (***Figure 3.2c & 3.2d***).

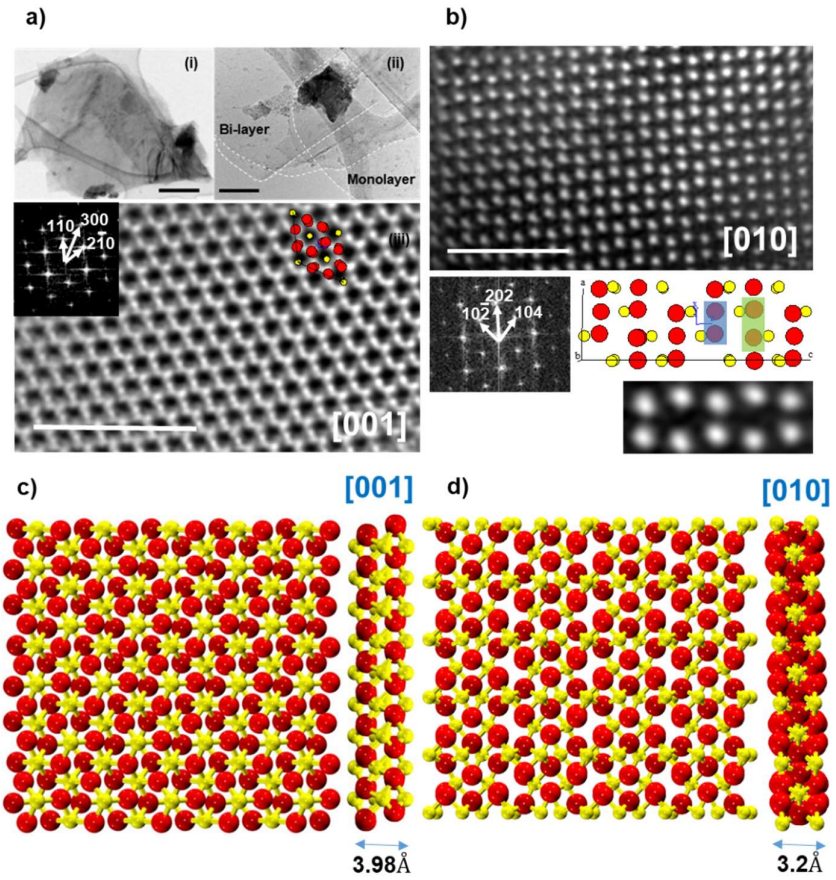

Figure 3.2. ***2D Morphology of Hematene: (a)*** (clockwise, from left) (i) bright field TEM image of a single sheet (the scale bar is 0.5 μm); (ii) High magnification bright field TEM image of a monolayer and bilayer hematene (the scale bar is 50 nm), and; (iii) HRSTEM image (the scale bar is 2 nm) of hematene in [001] orientation with its Fourier transform (FT) in the inset and position of atoms shown by red (oxygen) and yellow (iron) spheres. ***(b)*** HRSTEM (the scale bar is 2 nm) of hematene in [010] orientation with its FT at the bottom left and the structural model indicating the observed positions of ions; red spheres correspond to oxygen and yellow spheres correspond to iron at the right bottom. A high-resolution view of the [010] oriented plane is given at the bottom right corner in which variable distance between oxygen atoms in the adjacent columns are evident (highlighted in yellow and blue stripes in the structural model). Planar and cross-sectional simulated view of, ***(c)*** the [001] oriented plane, and ***(d)*** the [010] oriented plane.

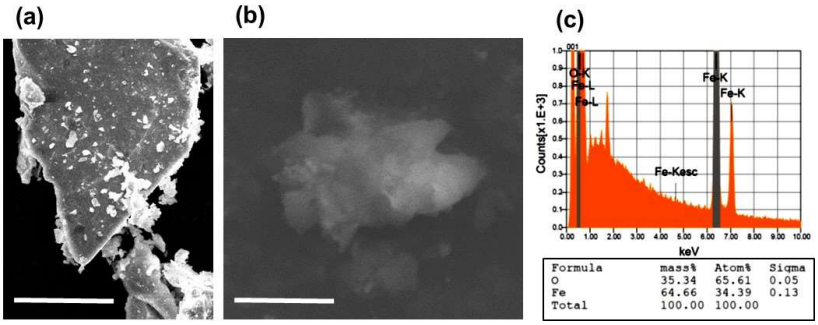

Figure 3.3. a) Scanning electron microscopy (SEM) image of pristine hematite (the scale bar is 20 µm) **b)** SEM micrograph of hematene (the scale bar is 5 µm) **c)** EPMA-WDS analysis of hematene

The surface morphology in scanning electron microscopy (SEM) (***Figure 3.3a & 3.3b***) shows thin sheets and the composition/purity was studied using field emission electron-probe microanalysis (FE-EPMA) equipped with wavelength dispersive spectroscopy (WDS) (***Figure 3.3c***), which shows only iron and oxygen atoms and do not show any impurities. The thickness of hematene sheets was measured by using atomic force microscopy (AFM) and is in good agreement with the theoretically observed monolayer thickness (***Figure 3.4***).

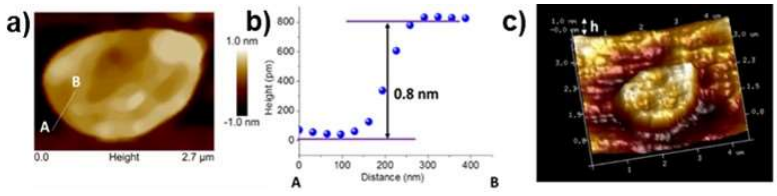

Figure 3.4. a) AFM images of the 2D hematene sheet **b)** height profile of the hematene sheet (bilayer), and **c)** 3D reconstruction of the image of hematene sheet.

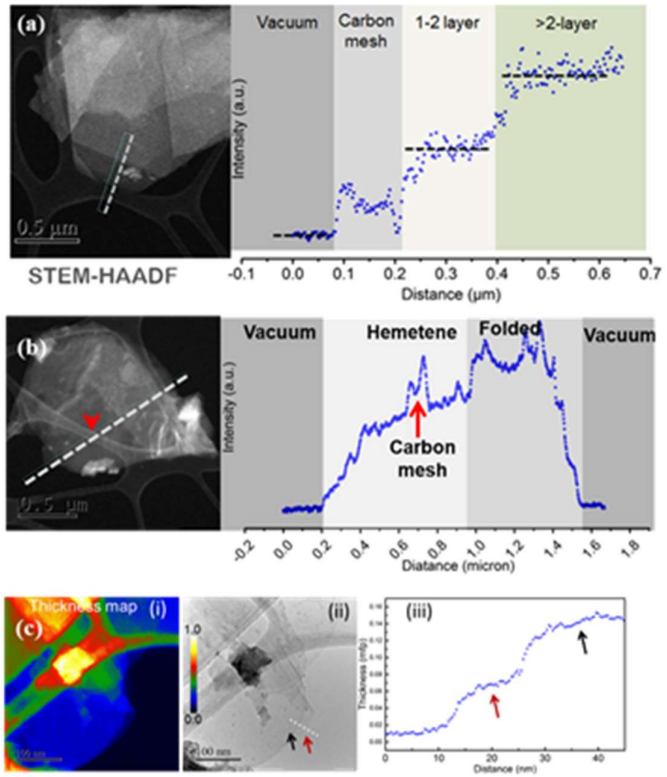

Figure 3.5. (a) The STEM images of hematene, with the line profiles. The step-wise nature of the line profile shows the 2D nature of hematene; ***(b)*** The STEM image of monolayer and intensity profile; ***(c)*** (i) Thickness map and (ii) bright field (iii) Intensity profile of a monolayer and bilayer hematene.

The line-intensity profile of high angle annular dark field STEM (HAADF-STEM) image (mass-thickness image) of several randomly stacked 2D hematene is given in ***Figure 3.5a***. The intensity plot shows a step but not continuous intensity variation. Generally, HAADF intensity gradually increases for the bulk materials as a function of thickness (from edge to core, when Z remain constant), but here the intensity step is a clear indication for the formation of well-separated 2D materials which are stacked over each other. We have used such intensity variation to quantify

the single layer as shown in ***Figure 3.5b***. Furthermore, we performed energy-filtered TEM (EFTEM) (above image), which shows thin 2D sheets of hematene ***Figure 3.5c***. In the EFTEM technique, a relative specimen thickness map can also be computed (given in the graph shown on the right) by acquiring an unfiltered and a zero-loss image (same region and identical conditions) using Poisson statistic of inelastic scattering. It gives the relative measure of the specimen thickness in units of the local inelastic mean free path. The colour map clearly distinguishes monolayer and bi-layer. Also, the thickness is found to be uniform across the sheet. The intensity profile across the bi-layer further confirm two sheets stacked randomly on top of each other.

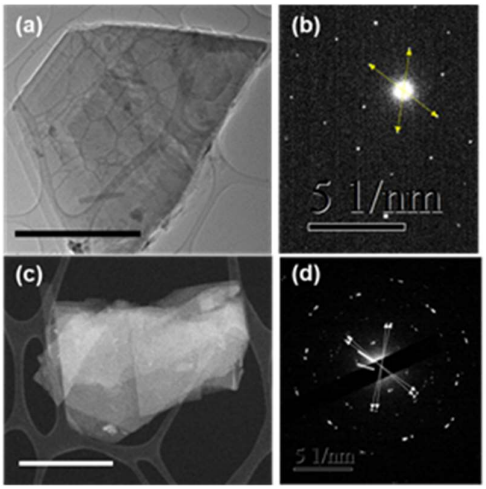

Figure 3.6. ***(a)-(b)*** Low magnification bright field image (scale bar 1µm) of an unexfoliated thick sheet and corresponding diffraction pattern. ***(c)-(d)*** Low magnification HAADF image (scale bar 1µm) and diffraction pattern covering the stacks of multiple 2D sheets.

In order to clarify the crystallographic registry, we have performed TEM of unexfoliated samples and stacked 2D sheets as shown in ***Figure. 3.6***. The dark contrast in the bright-field TEM image in ***Figure. 3.6a*** clearly reveals a thickness of several nanometers. The diffraction pattern (***Figure. 3.6b***) from these crystals shows a single oriented pattern. On the other hand, the randomly stacked 2D sheet can be seen in high angle annular dark field (HAADF) image

(***Figure. 3.6c***). To check the orientation of these, we have performed selected area diffraction as shown in ***Figure. 3.6d***. It clearly shows a miss orientation of 8-10 degree between similar planes (as shown by two lines) belonging to two hematene sheets stacked up on one another. We do observe a number of spots also due to misoriented planes corresponding to other exfoliated stack of hematene sheets.

3.4 Characterization of Hematene

Raman studies were carried out to confirm the formation of hematene. The Raman spectra of pristine hematite consist of seven symmetric vibration modes, namely two A_{1g} modes (225 and 498 cm^{-1}) and five E_g modes (247, 293, 299, 412 and 613 cm^{-1}).[9] The intense peak at around 1300 cm^{-1} is attributed to two-magnon scattering.[10] All the significant peaks of the hematene match with the reported spectrum of hematite (***Figure 3.7a***).[9,11]

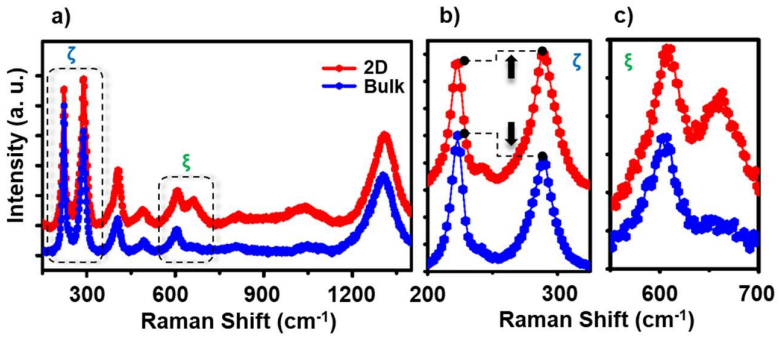

Figure 3.7. (a) Raman spectrum of bulk hematite powder and hematene; an enlarged view of the indexed peaks ζ and ξ are shown in ***(b)*** and ***(c)*** respectively. ***(b)*** The intensity variation of major Raman modes at 223 (A_g) and 288 cm^{-1}(E_g). ***(c)*** Presence of the Raman forbidden E_u mode at 662 cm^{-1} in hematene.

The striking variation observed on exfoliation is the change in intensity of the strong A_{1g} and E_g modes at 223 and 288 cm^{-1}, respectively. The

intensity ratio I_{A1g}/I_{Eg} is 1.18 in bulk, which decreases to 0.92 after exfoliation (***Figure 3.7b***). On comparing the peak positions of bulk and exfoliated hematite, it is evident that the A_{1g} modes shift towards lower frequencies (red-shift), whereas the E_g modes undergo blue-shift. The breakdown of the phonon momentum selection rule $q \approx 0$ due to confinement of phonons cause the observed redshift of A_{1g} modes.[12] However, the blue-shift of the E_g modes has not been previously observed in hematite. An additional mode observed at around 662cm^{-1} assigned to E_u, a forbidden vibrational mode in the Raman spectra of hematite (***Figure 3.7c***). This mode originates from disorder within the hematite crystal lattice.[13] The broad and weak appearance of the hematene E_u mode could be due to strong resonance on the surface, where the layers do not have complete symmetry of the bulk structure.[14] The shifts and intensity variations of all the Raman modes are summarized in **Table 3.1.**

Table 3.1. The variation of Raman frequency and intensity of various observed Raman Modes of hematite due to exfoliation is summarized.

Mode	**Bulk**		**Exfoliated**	
	Raman Shift(cm^{-1})	Intensity (norm)	Raman Shift(cm^{-1})	Intensity (norm)
A_g	222.8	1	222.6	0.920
E_g	288.3	0.84	289.3	1
E_g	401.7	0.24	405.2	0.35
A_g	493.7	0.10	490.1	0.10
E_g	603.2	0.17	607.7	0.24
E_u	-	-	662.6	0.18
Magnon	1300.9	0.68	1304.1	0.64

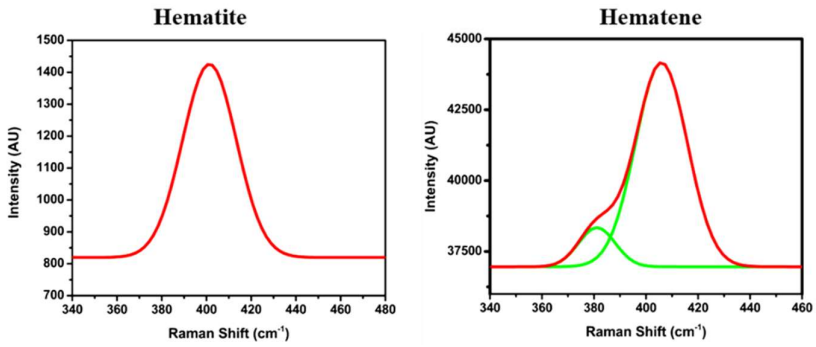

Figure 3.8. The defect mode (T) in hematene.

The appearance of additional peaks in the Raman spectra on exfoliation of hematite into hematene is due to defect states. The commonly observed LO and T modes ascribed to the loss of symmetry and formation of tetragonal defects respectively in hematite are observed in hematene.[13, 15] The ratio of LO mode to the Eg mode in hematite increases from 0.18 in hematite to 0.77 in hematene. Besides the loss of symmetry, the compensation of the surface by oxygen atoms leads to the appearance of T mode in hematene which is found to be absent in hematite (see ***Figure 3.8***). This has been previously observed in nanoparticles on decreasing their size which increases the surface area.[15]

It is imperative that the valence state of Fe is clearly established and for that, X-ray photoelectron spectroscopy (XPS) of pristine hematite (**Figure *3.9a***) and hematene (***Figure 3.9b***) were carried out. The obtained Fe2p spectrum confirmed that iron is exclusively in the +3 oxidation state in hematene with $Fe2p_{3/2}$ and $Fe2p_{1/2}$ peaks around 710.7 eV and 724.3 eV, respectively, which are 13.6 eV apart.[16] The peak in the O1s spectrum centred at 529.7 eV, is attributed to the lattice oxygen, while the peak

located at 532 eV corresponds to the oxygen defects in metal oxides.[17] The intense peak corresponding to defects state of oxygen in hematene signifies a very profound increase in the number of surface oxygen, typical of a 2D morphology.

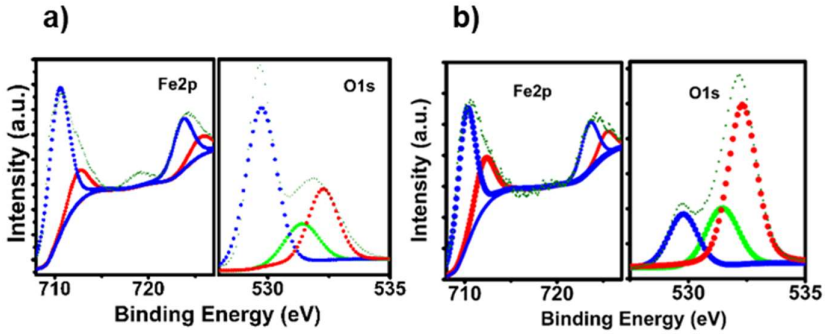

Figure 3.9. (a) X-ray photoelectron spectra of Fe2p and O1s of hematite and ***(b)*** Hematene.

3.5 Mechanism of exfoliation

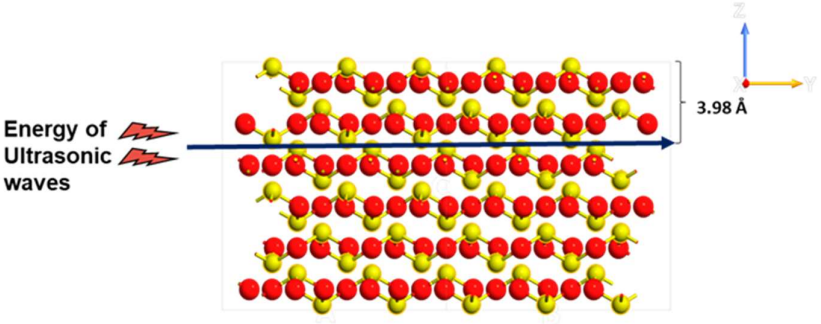

Figure 3.10. A representative figure showing the exfoliation of hematite into layered hematene in [001] direction.

Crystals commonly contain planes of atoms along which the bonding of the atoms is weaker compared to other planes. In hematite with the trigonal crystal structure, [001] has the highest broken bond density.[18] Alternating layers of Fe^{3+} and O^{2-} form a dipole moment perpendicular to [001] and tend to be less stable. On application of ultrasonic energy, the

hydrodynamic forces cleave the hematite crystal along the [001] and [010] directions. A pictorial representation is shown in ***Figure 3.10***.

3.6 Stability of Hematene

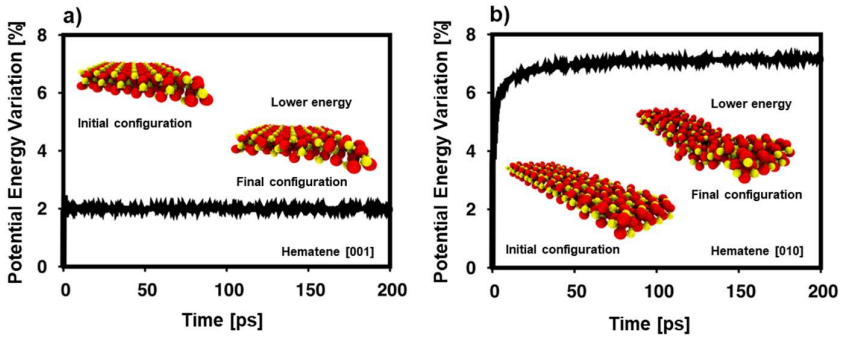

Figure 3.11. Potential energy variation of the hematene ***(a)*** (001) and ***(b)*** (010) sheets simulated by molecular dynamics; the minimum energy stable configurations are shown.

The surface structure of (001) and (010) faceted hematene sheets were simulated using fully atomistic reactive molecular dynamics (MD). The observed iron/oxygen ratio (=0.66), thickness (~0.4 nm), and crystal symmetry were used as parameters. The structural stability was established in the NPT ensemble at zero pressure (vacuum) and room temperature.[19] The planar edges were kept within the periodic boundary conditions in order to avoid any border effects. Molecular dynamics simulations were performed using the open source software LAMMPS[20] using the fully atomistic reactive force field called reaxFF.[21] In this approach, the chemical reactions as the bond formation and/or breaking can be accurately estimated due to its parameterization through the density functional theory (DFT) calculations and/or experimental data. The parameterization used in this work is described in detail in *Ref.50*.[22] The structural stability was investigated for two different arrangements [001]

and [010] (see ***Figure. 3.2 c&d***). In both cases, the structures were equilibrated during 200 ps under NPT ensemble at 300 K and zero pressure using Nose-Hoover integrator scheme.[23] The simulation box was kept within the periodic boundary conditions along the sheet plane in order to avoid any border effect. The potential energy-time graph of the hematene sheets along the two different orientations (***Figure 3.11a & 3.11b***) stabilizes after 200 ps at room temperature. However, the (001) faceted sheet exhibit lower structural variations and is presumed to be more stable.

3.7 Magnetic Properties of Hematene

Magnetism in hematite is largely governed by the antiferromagnetic Fe^{3+}–O–Fe^{3+} super-exchange interactions.[6] Furthermore, specularite could show lamellar magnetism giving higher magnetization values.[8] It is well established that between the T_N of approximately 961 K and the Morin transition temperature (T_M) at ~265 K, hematite exhibits weak ferromagnetism.[7, 24] In this phase, the spins lie perpendicular to the c-axis such that the spins of the iron sub-lattice within each layer are approximately parallel to each other, but antiparallel to those in adjacent layers. A Dzyaloshinski-Moriya interaction[25] give rise to a small canting of moments within each plane and results in a net ferromagnetic moment of 0.005 μB/iron atom and is a weak ferromagnetic (WF) state. Below T_M, moments rotate through almost 90° to lie along the c-axis. This phase referred to as the antiferromagnetic (AF) state having no net magnetization (the anti-parallel moments are slightly canted to give parasitic weak ferromagnetism).

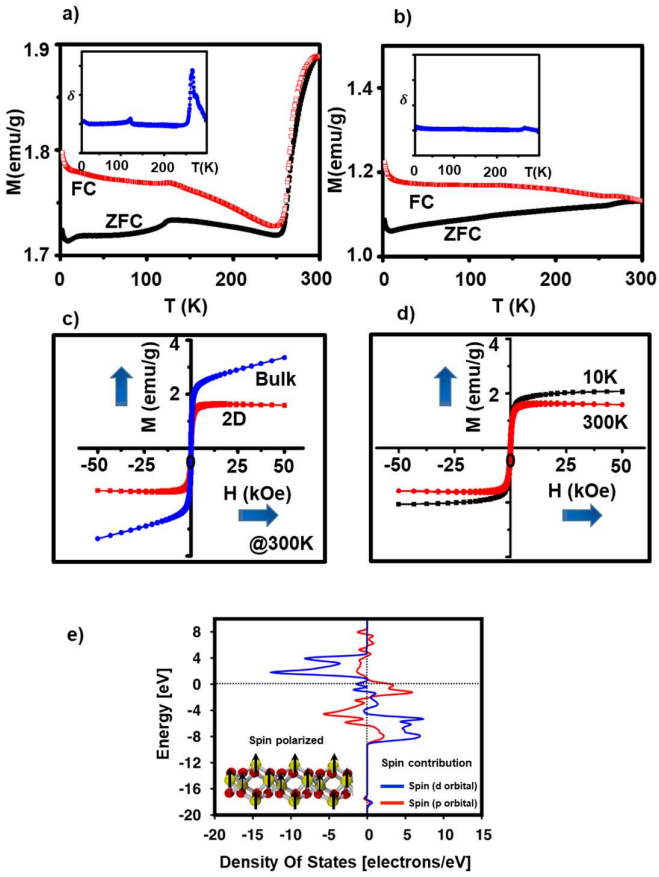

Figure 3.12 Magnetism of Hematene: (a) The FC-ZFC measurement of bulk hematite at 1000 Oe (from 300K down to 2K) with the differential (dM/dT) plot of the ZFC curve shown in the inset. ***(b)*** FC-ZFC measurement of hematene at 1000 Oe with the differential plot in the inset. ***(c)*** Comparison of the room temperature hysteresis of bulk and hematene and ***(d)*** The comparison of room temperature (300K) and low temperature (10K) hysteresis of hematene. ***(e)*** The density of states contributions of p and d orbitals of hematene as determined by DFT calculations; spin polarization in hematene is also shown.

Consequently, a sharp drop in susceptibility is observed at T_M. Bulk hematite shows this drop at around 265 K, which is evident in the field

cooled - zero field cooled (FC-ZFC) plots and characterized by a sharp peak in the differential (dM/dT) plot of the ZFC curve (***Figure 3.12a***).

We hypothesize that hematite nanostructuring could significantly influence its magnetic properties. Earlier reports on nanocrystalline hematite indicate that particle shape, size, crystallinity, and surface influence the value of T_M.[26, 27] Sorescu and co-workers detected the WF and AF phases in hematite nanostructures and they coexist below T_M, but the population of WF phase strongly depends on the morphology.[28]

Furthermore, the Morin transition has been found to be completely suppressed in mesoporous hematite and hematite nanotubes due to a long-range magnetic ordering.[29, 30] Similar behaviour is observed in hematene. Splitting between the FC and ZFC curves from the highest experimental temperature (300 K) implies a WF phase over the entire temperature range studied and the suppression of a Morin transition (***Figure 3.12b***). The hysteresis of hematene exhibits a WF phase with a good degree of saturation at the room temperature. The loop saturates at low field compared to pristine hematite that saturates only at an applied field >50,000 Oe (5 T) (***Figure 3.12c***). The hysteresis loop for hematene traced at 10 K also displays an enhanced coercivity (H_c) and saturation magnetization (M_s) (Refer ***Table 3.2***), which is characteristic of an FM phase (***Figure 3.12d***). Irrespective of the orientation of magnetic sublattices, the surface spins of the 2D sheets in addition to WF by uncompensated spin canting would greatly enhance the FM behaviour as compared to the pristine sample; giving rise to a good degree of saturation and enhanced coercivity.

Spin-polarized calculations within the framework of DFT aid further investigation of the magnetic response of hematene. All first principle calculations were performed using CASTEP code[31], a plane-wave implementation of density functional theory (DFT), in the spin-polarized approach. The exchange-correlation (XC) contribution to the DFT energy was calculated using the GGA/PW91 functional[32] in the GGA+U framework (Hubbard term). It is a standard approach for systems that presents a strong correlation as in iron oxides materials.[33, 34] Due to the strong electronic correlation present in these iron oxide systems, calculations are performed considering the Hubbard term. The total spin and the density of states were elucidated for the most stable (001) orientated hematene.

Table 3.2 presents the occupation, charge and spin per atom. Two important magnetic properties could arise: the spin polarization from iron atoms, as already shown for hematite[40], and (001) faceted hematene favours FM ordering, while bulk prefers AF ordering. ***Figure 3.12e*** depicts the density of states based on the contributions of the p and d orbitals. As expected, the major contribution is from the d orbitals. The schematic of the FM order in (001) faceted hematene is also shown at the bottom left side of ***Figure 3.12e***, which is in compliance with the FM behaviour observed experimentally.

Table 3.2 Charge and spin populations through Mulliken analysis. Notice how the magnetic ordering comes mostly from iron atoms.

Species	s	p	d	f	Total occupation	Charge(e)	Spin (ħ)
O	1.87	4.86	0.00	0.00	6.73	-0.73	0.03
O	1.87	4.86	0.00	0.00	6.73	-0.73	0.03
O	1.87	4.86	0.00	0.00	6.73	-0.73	0.03
O	1.87	4.86	0.00	0.00	6.73	-0.73	0.03
O	1.87	4.86	0.00	0.00	6.73	-0.73	0.03
O	1.87	4.86	0.00	0.00	6.73	-0.73	0.03
O	1.87	4.81	0.00	0.00	6.68	-0.68	0.02
O	1.87	4.81	0.00	0.00	6.68	-0.68	0.02
O	1.87	4.81	0.00	0.00	6.68	-0.68	0.02
Fe	2.50	6.53	5.89	0.00	14.92	1.08	1.84
Fe	2.56	6.30	6.10	0.00	14.96	1.04	1.94
Fe	2.50	6.53	5.89	0.00	14.92	1.08	1.84
Fe	2.56	6.30	6.10	0.00	14.96	1.04	1.94
Fe	2.54	6.58	5.76	0.00	14.89	1.11	2.09
Fe	2.54	6.58	5.76	0.00	14.89	1.11	2.09

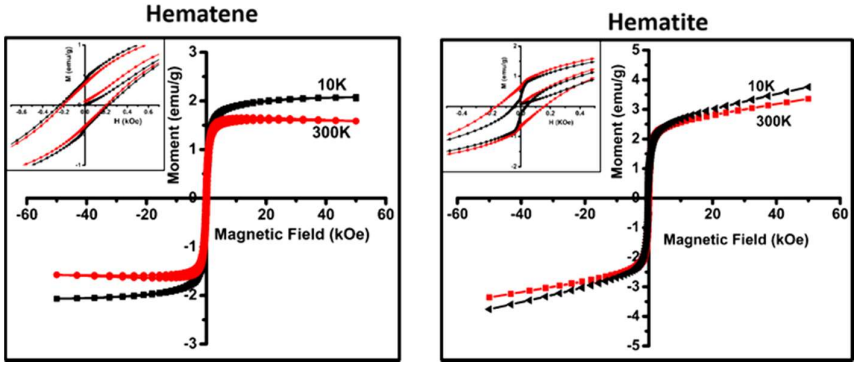

Figure 3.13. The hysteresis of hematene and hematite, the zoomed inset shows the magnetization at the zero applied fields and the coercivity.

The room-temperature (300 K) and low temperature (10 K) M-H measurements of pristine hematite and hematene are shown below (***Figure 3.13***) and the loop parameters are summarized in ***Table 3.3***.

Table 3.3. Comparison of magnetic properties of pristine hematite and hematene.

Hysteresis Parameters	**Bulk**	**Hematene**	**Temperature**
Hc (Oe)	160	200	300 K
Mr (emu/g)	0.65	0.35	
Ms (emu/g)	-	1.60	
Hc (Oe)	40	230	10 K
Mr (emu/g)	0.20	0.40	
Ms (emu/g)	-	2	

3.8 Photocatalytic Activity of Hematene

α-Fe_2O_3 (hematite) has a band gap in the range of 1.8 to 2.2 eV, which is optimum for hydrogen generation via water photoelectrolysis.[35, 36] However, it suffers from poor carrier transport properties, primarily because of its intrinsic, as well as, surface defects serving as midgap trap centres, limiting the lifetime of photo-generated carriers to a few picoseconds.[37] The hole diffusion length in the material is generally less than ~4 nm and the electron transport is hindered by very low mobility. Slow water oxidation kinetics is another problem. Spontaneous water splitting is generally not expected from α-Fe_2O_3 due to its more positive flat band potential (vs normal hydrogen electrode, NHE) compared to water reduction potential.[15] Hematene is expected to mitigate these problems due to the 2D geometry, enabling photons to generate electrons and holes at the surface itself so that they can carry out redox reactions before recombination. As the light absorbed in a monolayer is too low to efficiently split water, we used a high surface area material, titanium

dioxide nanotube arrays, to support hematene and consequently enhance light absorption.

Titanium dioxide is a powerful oxidation photocatalyst with superior carrier transport properties, but possessing an unfavourable band gap (3.2 eV for the anatase phase).[38] The photoresponse of titania is limited to wavelengths in the ultraviolet region (< ~400 nm). Doping and surface sensitization with narrow bandgap semiconductors and plasmonic metal nanoparticles are commonly adopted for enhancing the visible light photoactivity.[39] The titania nanotube array films fabricated using anodic oxidation were proven to yield incident photon-to-current conversion efficiencies (IPCE) near 80% in the ultraviolet region of the solar spectrum.[40] We hypothesized that the visible light activity of these nanotubes could be enhanced by loading hematene sheets on the surface. Although the conduction electrons in hematite generally possess a lower energy than those in titania, we predicted an upward shift (more negative vs NHE) in the flat band position of α-Fe_2O_3 as a result of widening of the band gap from 1.83 eV to 2.2 eV upon exfoliation, making the new position conducive for electron transport to the conduction band (CB) of titania.

Figures *3.14a* and ***3.14b*** show the photographs and scanning electron microscope images of bare titania nanotube array film and hematene loaded titania nanotubes, respectively.[41] The SEM images showed no significant difference between the surfaces of bare and hematene loaded nanotubes, except some aggregated 2D sheets seen on the surface (**Figure *3.14c***). As evident from the inset of **Figure *3.14c,*** the greyish titania film

turned into brick red upon loading hematene. The Raman spectrum of the hematene loaded TiO_2 nanotube film is given in **Figure *3.14d***. All peaks could be assigned to either the anatase phase of titania or α-Fe_2O_3.[38, 42]

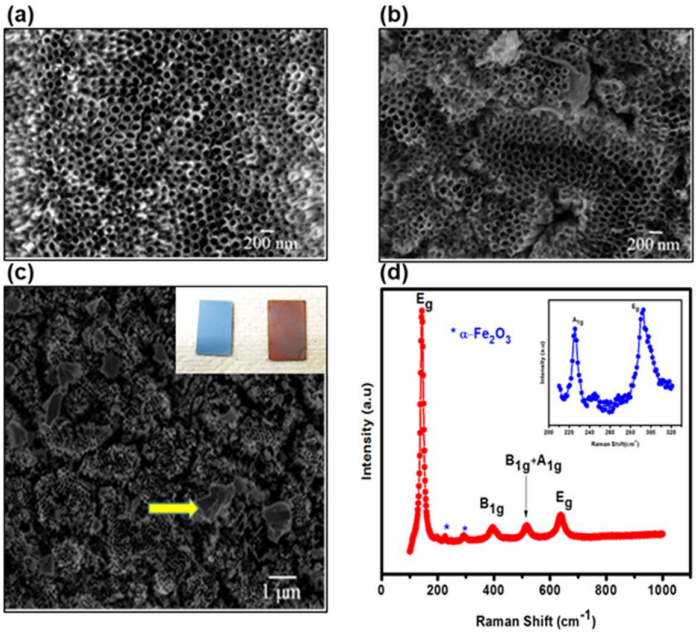

Figure 3.14. SEM images of ***(a)*** bare titania nanotube array; ***(b)*** Hematene loaded nanotubes and; ***(c)*** the nanotube surface having aggregated 2D sheets, and; ***(d)*** Raman spectrum of hematene loaded titania nanotubes.

The photocurrent spectrum clearly showed visible light photocatalytic activity in nanotubes loaded with hematene (***Figure 3.15a***). The incident photon conversion efficiency (IPCE) spectra of bare, as well as hematene-loaded nanotubes, were recorded in a two-electrode configuration with no external electrical bias applied between the electrodes. Nanotubes loaded with particles from the hematite ore used for exfoliation did not show noticeable IPCE in the ultraviolet or visible light region. IPCE spectra of

bare nanotubes and those with low and high loading levels of 2D sheets are given in ***Figure 3.15b***.

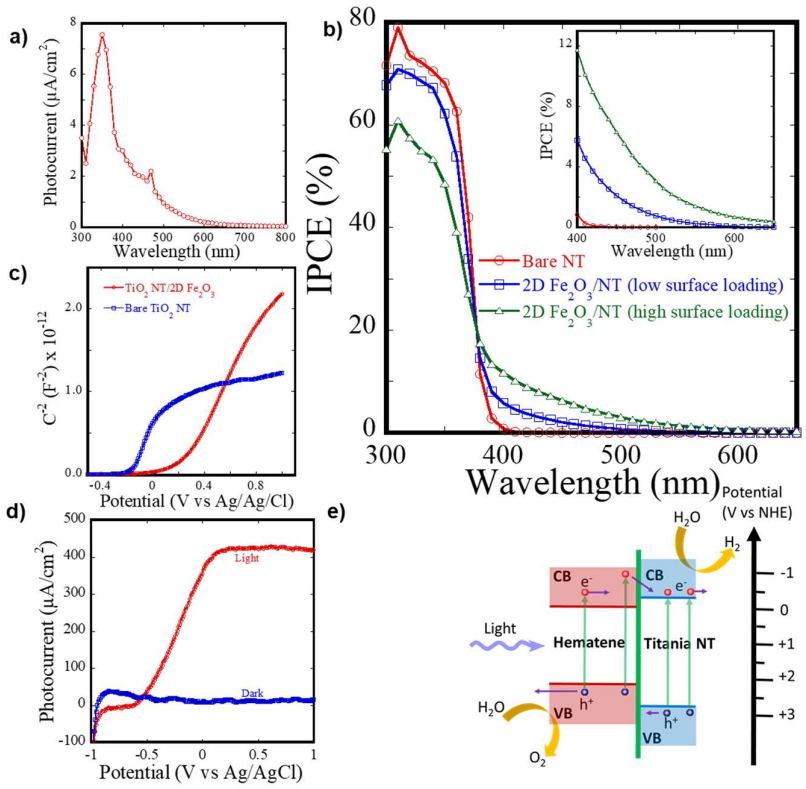

Figure 3.15. Photocatalysis: (a) Photocurrent spectrum showing the visible light photocatalytic activity of the titania nanotube (NT)-hematene system. ***(b)*** IPCE spectra of bare titania NT array film and those with low and high loading levels of hematene. ***(c)*** Mott-Schottky plots showing the band positions of bare and hematene loaded titania NT at pH 6.2. ***(d)*** Linear sweep voltammograms of a hematene-titania (high surface loading) photoanode recorded under dark and AM 1.5G illumination conditions. ***(e)*** Schematic representation of interfacial charge transfer between hematene and TiO_2 NTs. Energetic photoelectrons in the conduction band (CB) of hematene get transferred to the CB of titania NT while photo-generated holes in the valence band (VB) oxidize water.

IPCE was calculated using the relation (equation 3.1),

$$IPCE = \frac{100\, hcj(\lambda)}{e\lambda P(\lambda)} \qquad (3.1)$$

where h is the Planck constant, c the velocity of light, e the electron charge, λ the wavelength, $j(\lambda)$ the photocurrent density at λ and $P(\lambda)$ the power density of light at λ. The solar photocurrent (AM 1.5G irradiance) density j was calculated using the relation given in equation 3.2,

$$j = \int_{\lambda_{min}}^{\infty} IPCE \;\; I(\lambda)\, \lambda \left(\frac{e}{hc}\right) d\lambda \qquad (3.2)$$

Here $I(\lambda)$ is the power density of AM 1.5G solar radiation at the wavelength λ.

The IPCE increased from almost zero to 12% at 400 nm with zero external bias. The solar photocurrent calculated by integrating IPCE with the AM1.5G spectrum showed a dramatic increase with hematene loading on nanotubes due to the enhanced visible light activity. The values obtained for curves in ***Figure 3.15b*** are respectively 0.56, 0.67 and 0.93 mA/cm^2 for bare nanotubes and those with low and high hematene loading. Corresponding average photocurrent densities for IPCE spectra recorded from various photoelectrochemical cells are 0.57±0.01, 0.67±0.02 and 0.83±0.05 mA/cm^2. Kontos *et al.* showed that titania nanotubes functionalized with iron oxide nanoparticles possess enhanced activity for photodegradation of methyl orange.[35] These results were not supported with data from IPCE measurements. The authors speculated that the enhancement was due to the improved charge carrier separation. LaTempa *et al.* developed hematite nanotube arrays, but the maximum IPCE was only about 3.5%.[43]

We note that the IPCE in the range of 12% is unprecedented in α-Fe_2O_3 loaded titania nanotubes. A slight reduction observed in IPCE in the

ultraviolet region (***Figure 3.15b***) was believed to be a consequence of the accumulation of 2D sheets on the surface of nanotubes clogging the pores. Titania nanotubes contribute substantially to the high IPCE in the ultraviolet region. The accumulated hematene sheets (***Figure 3.14c***) on the surface block the ultraviolet wavelengths from reaching titania nanotubes and lower the IPCE. The IPCE is expected to go up further upon conformal loading of 2D sheets onto the nanotube surface.

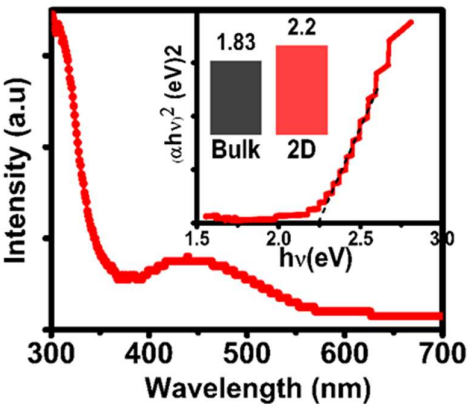

Figure 3.16. The UV-visible absorption spectrum of hematene; the band-gap is determined from the Tauc-plot (inset); an increased bandgap is observed on confinement to 2-dimensions.

Non-zero IPCE in hematene/nanotube samples in the 400 – 550 nm wavelength range (see ***Figure 3.15b***) suggests that holes from hematene took part in water oxidation and electrons were transferred to the nanotubes. To find out if the electron injection from hematene to titania nanotube was facilitated by an upward shift in the CB, we performed Mott-Schottky measurements. As Mott-Schottky measurements were not originally developed for porous nanostructured samples, the results are used only for qualitative interpretations. The Mott-Schottky plots given in ***Figure 3.15c*** show a shift in the flat band position towards a more positive potential (vs Ag/AgCl) upon hematene loading. Thus, an offset exists in the band positions of titania nanotubes and hematene. However, the magnitude of the offset may be less compared to

pure hematite (ore) due to the increased band gap (2.2 eV compared to 1.83 eV of the pristine hematite) upon exfoliation (***Figure 3.16***). It is believed that the enhancement in the visible light activity of titania nanotubes originated from the transfer of hot electrons from hematene. The linear sweep voltammetry curves recorded under the AM 1.5G conditions showed a saturation photocurrent of 0.42 mA/cm^2 (***Figure 3.15d***).

A schematic representation of interfacial charge transfer between hematene and TiO_2 nanotubes is shown in ***Figure 3.15e***. Under illumination, photons with energies greater than 2.2 eV excite electrons from the valence band of hematene to the CB. The electrons excited by high energy photons reach higher levels in the hematene conduction band and get thermodynamically transferred to the CB of TiO_2. Such a transfer is apparently facilitated by the 2D morphology of hematene. The photogenerated holes in the valence band of hematene take part in the water oxidation process. The holes are also generated in titania nanotubes by ultraviolet photons and these holes are transferred to hematene sheets having an interface with the walls of the nanotube. The holes generated in the regions of nanotubes not covered by hematene directly perform water oxidation. The magnitude of the photocurrent is lower compared to the solar photocurrent obtained by integrating IPCE. The lower ultraviolet content in the simulated spectrum (intensity notable for λ>350 nm) compared to the standard AM1.5G solar spectrum (intensity high for λ>280 nm) is believed to be the primary cause.

3.9 Conclusion

A two-dimensional material 'Hematene' was successfully exfoliated from a non-van der Waals/non-layered natural hematite ore by means of liquid exfoliation in dimethylformamide solvent. Two-dimensional morphology is confirmed by means of STEM and AFM imaging. Hematene phase purity is confirmed by means of Raman spectroscopy. It was established that the exfoliated planes are of [001] and [010] orientation and molecular dynamics simulations proved [001] oriented hematene sheets were most stable.

Hematene, the two-dimensional counterpart of hematite was proved to have a ferromagnetic ground state whereas hematite is antiferromagnetic. The [001] oriented hematene sheets were subjected to spin-polarized density functional theory calculations and the results predicted a ferromagnetic ground state. The ferromagnetism of the exfoliated hematene sheets was verified experimentally by means of SQUID-VSM measurements. The Photocatalytic water splitting activity of hematene sheets was demonstrated by forming a heterojunction with titania nanotube array electrodes. It was found that hematene sheets are capable of sensitizing titania nanotubes, to capture the visible portion of the solar spectrum (400 nm – 700 nm), otherwise having photocatalytic activity at UV region (<400 nm) only.

3.10 References

1. M. Marelli, A. Naldoni, A. Minguzzi, M. Allieta, T. Virgili, G. Scavia, S. Recchia, R. Psaro and V. Dal Santo, *ACS Appl. Mater. Interfaces*, 2014, **6**, 11997-12004.
2. M. Mishra and D.-M. Chun, *Applied Catalysis A: General*, 2015, **498**, 126-141.
3. J. Chen, L. Xu, W. Li and X. Gou, *Advanced Materials*, 2005, **17**, 582-586.
4. K. Sivula, F. Le Formal and M. Grätzel, *ChemSusChem*, 2011, **4**, 432-449.
5. A. S. Teja and P.-Y. Koh, *Progress in Crystal Growth and Characterization of Materials*, 2009, **55**, 22-45.
6. A. Hill, F. Jiao, P. Bruce, A. Harrison, W. Kockelmann and C. Ritter, *Chemistry of Materials*, 2008, **20**, 4891-4899.
7. F. J. Morin, *Physical Review*, 1950, **78**, 819-820.
8. P. Robinson, R. J. Harrison and S. A. McEnroe, *Nature*, 2002, **418**, 517.
9. D. L. A. deFaria, S. V. Silva and M. T. de Oliveira, *Journal of Raman Spectroscopy*, 1997, **28**, 873-878.
10. K. F. McCarty, *Solid State Communications*, 1988, **68**, 799-802.
11. D. Bersani, P. P. Lottici and A. Montenero, *Journal of Raman Spectroscopy*, 1999, **30**, 355-360.
12. I. H. Campbell and P. M. Fauchet, *Solid State Communications*, 1986, **58**, 739-741.
13. J.-W. Jang, C. Du, Y. Ye, Y. Lin, X. Yao, J. Thorne, E. Liu, G. McMahon, J. Zhu, A. Javey, J. Guo and D. Wang, *Nature Communications*, 2015, **6**, 7447.
14. S. H. Shim and T. S. Duffy, *American Mineralogist*, 2002, **87**, 318-326.
15. I. V. Chernyshova, M. F. Hochella Jr and A. S. Madden, *Physical Chemistry Chemical Physics*, 2007, **9**, 1736-1750.
16. J. Chastain, R. C. King and J. Moulder, *Handbook of X-ray photoelectron spectroscopy: a reference book of standard spectra for identification and interpretation of XPS data*, Physical Electronics Eden Prairie, MN, 1995.
17. X. Lu, Y. Zeng, M. Yu, T. Zhai, C. Liang, S. Xie, M.-S. Balogun and Y. Tong, *Advanced Materials*, 2014, **26**, 3148-3155.

18. Z.-y. Gao, W. Sun and Y.-h. Hu, *Transactions of Nonferrous Metals Society of China*, 2014, **24**, 2930-2937.
19. S. Nosé, *The Journal of Chemical Physics*, 1984, **81**, 511-519.
20. S. Plimpton, *Journal of Computational Physics*, 1995, **117**, 1-19.
21. A. C. T. van Duin, S. Dasgupta, F. Lorant and W. A. Goddard, *The Journal of Physical Chemistry A*, 2001, **105**, 9396-9409.
22. M. Aryanpour, A. C. T. van Duin and J. D. Kubicki, *The Journal of Physical Chemistry A*, 2010, **114**, 6298-6307.
23. W. G. Hoover, *Physical Review A*, 1985, **31**, 1695.
24. F. Grønvold and E. J. Samuelsen, *Journal of Physics and Chemistry of Solids*, 1975, **36**, 249-256.
25. T. Moriya, *Physical Review*, 1960, **120**, 91-98.
26. R. D. Zysler, D. Fiorani, A. M. Testa, M. Godinho, E. Agostinelli and L. Suber, *Journal of Magnetism and Magnetic Materials*, 2004, **272–276, Part 2**, 1575-1576.
27. D. Schroeer and R. C. Nininger, *Physical Review Letters*, 1967, **19**, 632-634.
28. M. Sorescu, R. A. Brand, D. Mihaila-Tarabasanu and L. Diamandescu, *Journal of Applied Physics*, 1999, **85**, 5546-5548.
29. F. Jiao, A. Harrison, J.-C. Jumas, A. V. Chadwick, W. Kockelmann and P. G. Bruce, *Journal of the American Chemical Society*, 2006, **128**, 5468-5474.
30. L. Liu, H.-Z. Kou, W. Mo, H. Liu and Y. Wang, *The Journal of Physical Chemistry B*, 2006, **110**, 15218-15223.
31. S. J. Clark, M. D. Segall, C. J. Pickard, P. J. Hasnip, M. I. Probert, K. Refson and M. C. Payne, *Zeitschrift für Kristallographie-Crystalline Materials*, 2005, **220**, 567-570.
32. J. P. Perdew, J. A. Chevary, S. H. Vosko, K. A. Jackson, M. R. Pederson, D. J. Singh and C. Fiolhais, *Physical Review B*, 1992, **46**, 6671.
33. G. Rollmann, A. Rohrbach, P. Entel and J. Hafner, *Physical Review B*, 2004, **69**, 165107.
34. Z. D. Pozun and G. Henkelman, *The Journal of Chemical Physics*, 2011, **134**, 224706.
35. A. I. Kontos, V. Likodimos, T. Stergiopoulos, D. S. Tsoukleris, P. Falaras, I. Rabias, G. Papavassiliou, D. Kim, J. Kunze and P. Schmuki, *Chemistry of Materials*, 2009, **21**, 662-672.
36. J. H. Kennedy and K. W. Frese, *Journal of the Electrochemical Society*, 1978, **125**, 723-726.

37. J. H. Kennedy and K. W. Frese, *Journal of the Electrochemical Society*, 1978, **125**, 709-714.
38. D. O. Scanlon, C. W. Dunnill, J. Buckeridge, S. A. Shevlin, A. J. Logsdail, S. M. Woodley, C. R. A. Catlow, M. J. Powell, R. G. Palgrave and I. P. Parkin, *Nature Materials*, 2013, **12**, 798-801.
39. M. Pelaez, N. T. Nolan, S. C. Pillai, M. K. Seery, P. Falaras, A. G. Kontos, P. S. Dunlop, J. W. Hamilton, J. A. Byrne and K. O'shea, *Applied Catalysis B: Environmental*, 2012, **125**, 331-349.
40. B. M. Rao, A. Torabi and O. K. Varghese, *MRS Communications*, 2016, **6**, 375-396.
41. M. Paulose, K. Shankar, S. Yoriya, H. E. Prakasam, O. K. Varghese, G. K. Mor, T. A. Latempa, A. Fitzgerald and C. A. Grimes, *The Journal of Physical Chemistry B*, 2006, **110**, 16179-16184.
42. T. Ohsaka, F. Izumi and Y. Fujiki, *Journal of Raman spectroscopy*, 1978, **7**, 321-324.
43. T. J. LaTempa, X. Feng, M. Paulose and C. A. Grimes, *The Journal of Physical Chemistry C*, 2009, **113**, 16293-16298.

Chapter 4

Ilmenene – A novel 2D Material from Ilmenite

Ilmenite resembles hematite structurally and non-layered in nature having a favourable c/a ratio for exfoliation. This chapter describes the exfoliation of 'ilmenene', the 2D counterpart of ilmenite, by liquid phase exfoliation. Investigations on the magnetism of ilmenene sheets is carried out both experimentally and theoretically and the results are correlated. The Photocatalytic activity of ilmenene is also studied by forming a heterojunction with titania nanotubes and the evolved hydrogen employing this heterojunction is quantified. These results are also discussed in this chapter.

ACS Chemistry of Materials *30(17): 5923-5931*

4.1 Introduction

The successful exfoliation of hematene, a non-van der Waals material, from hematite[1] ore serves as a motivator for exploring the possibility of obtaining high-quality two-dimensional (2D) material from naturally occurring ore materials. Ilmenite ore is similar in structure to hematite where half of the iron is replaced by titanium. Besides the structural similarity, like hematite, ilmenite is also an antiferromagnetic semiconductor with a Neel temperature of 55 K.[2] Such resemblances of hematite and ilmenite augurs well for the exfoliation of a 2D material of ilmenite. The 2D analogue of ilmenite is christened 'ilmenene'.

Ilmenite is expected to have two oxidation state for cations with respect to anion state O^{2-}, that is, either $Fe^{2+}Ti^{4+}$ or $Fe^{3+}Ti^{3+}$. The interchange between these charge configurations is common in Fe and Ti-bearing minerals.[3] This charge ordering influences the electronic and magnetic properties of ilmenite. Knowledge of the type of 'charge ordering' prevailing in the ilmenene sheets is very important in the study of its ground state electronic and magnetic properties.

Naturally occurring layered magnetic materials have been studied extensively, both theoretically and experimentally, to see whether they retain magnetism down to mono/few layers.[4-12] There are a large number of iron-rich natural ores having robust magnetism in their bulk form. Ilmenite ($FeTiO_3$) is one among them which has an important role in determining earth's magnetism.[13] It is envisaged that ilmenene, the 2D analogue of ilmenite, will serve as an ideal template for investigating 2D magnetism, which is a hot topic of research from a fundamental

perspective. A thorough understanding of magnetism in 2D ilmenene would be helpful in tailoring the magnetic properties of such 2D magnetic semiconductors. Such a proposition is attractive in developing 2D magnetic semiconductors and would augment the search for 2D magnetic materials for future spintronic applications.

Apart from magnetic properties, it is our endeavour to propose a plausible mechanism of exfoliation which would become a template for proposing new functional materials. Density functional theory (DFT) calculations are intended to corroborate the experimental findings. Ilmenene is expected to have comparable bandgap energy with that of titania along with the presence of defect states which qualifies it to be a good choice to sensitize titania nanotube array electrodes for visible light activity.

4.2 Experimental

The ilmenite ore is an electron-probe microanalysis (EPMA) natural mineral standard, provided by the EPMA laboratory in the Earth Science Department, Rice University, Houston, TX, USA. The composition of the ilmenite standard is given in ***Table.4.1***. Finely powdered ilmenite is liquid exfoliated in dimethylformamide (DMF) solvent, ultracentrifuged followed by filtration of the supernatant liquid to obtain ilmenene. Most of the experimental conditions are similar in nature as that adopted in the case of hematene. The details are described in chapter 3. A schematic of the exfoliation process is given in ***Figure 4.1***.

Constituent Compounds		Cation numbers normalized to 3 Oxygen atoms	
Chemical Formula	Percentage	Name	Cation Number
TiO_2	54.61	Ti	0.930
FeO	22.42	Fe2+	0.424
MgO	14.55	Mg	0.491
Fe_2O_3	5.41	Fe3+	0.092
Cr_2O_3	1.73	Cr	0.031
MnO	0.55	Mn	0.011
Al_2O_3	0.44	Al	0.012
NiO	0.17	Ni	0.003
CaO	0.13	Ca	0.003
SiO_2	0.12	Si	0.003
Total	100.13	Total	2.00

Table 4.1. The constituent compounds of ilmenite and cation numbers.

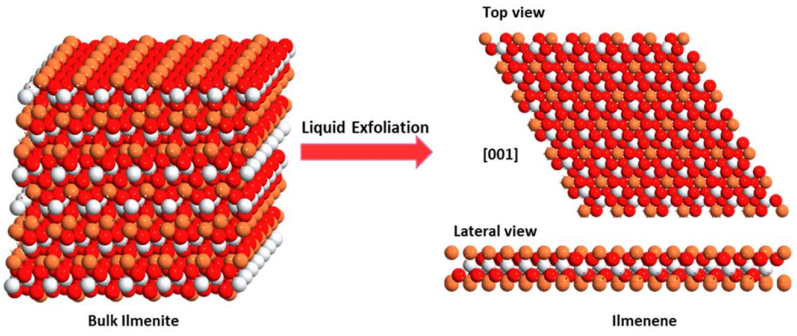

Figure 4.1. Schematic: Liquid exfoliation of bulk ilmenite (left) into most stable [001] oriented 2D monolayers (right). Planar (right top) and a cross-sectional view (right bottom) of the monolayer are shown; White, brown and red colours denote Ti, Fe and O atoms, respectively.

Analytical Tools: Most of the characterization techniques employed are similar to those used in the characterization of hematene (refer chapter 3 analytical tools section). Photoluminescence (PL) Spectra was recorded on a Horiba Nanolog Spectrofluorometer. The emission spectra were recorded through a 5 nm slit width with an excitation wavelength of 280 nm passing through a 5 nm slit width.

Formation 2D $FeTiO_3/TiO_2$ heterojunction and Photocatalysis Measurements:

The preparation conditions are identical and details are already provided in chapter 3. As prepared NTs were sensitized with ilmenene sheets by dipping them in a colloidal solution of ilmenene at 200 ℃ for 24 hours in a Teflon sealed autoclave. The ilmenene coated nanotubes were annealed at 200 °C for 30 minutes.

The photocurrent measurements were carried out using an electrochemical analyzer (CH instruments model 660C) in a three-electrode configuration. The 2D $FeTiO_3$/ TiO_2 with an area of 0.70 cm^2, platinum and Ag/AgCl were used as the working, counter and reference electrodes receptively. Aqueous 0.5 M Na_2SO_4 solution was used as the electrolyte. Potential sweeps were made from -1 to +1 V at a rate of 1 mV/S. The hydrogen generation experiments were conducted using a two-electrode system consisting of $FeTiO_3$ sensitized NT as the photoanode and a platinum foil as the cathode. A simulated sunlight illumination (xenon arc lamp, Newport, model 67005) of intensity 100 $mWcm^{-2}$, set using a National Renewable Energy Laboratory (NREL) calibrated silicon solar cell, was used for recording current-voltage characteristics and

hydrogen generation experiments. A same three-electrode configuration under dark conditions at a frequency of 1000 Hz in 0.5 M Na_2SO_4 was used for Mott-Schottky measurements as well. The light sources were fitted with AM 1.5 G filters. The incident photon to current conversion efficiency (IPCE) was recorded using a setup consisting of a monochromator and a power meter (both from Newport).

The photocatalytic hydrogen production was done at room temperature in a quartz dual chamber setup employing 2D $FeTiO_3/TiO_2$ as oxygen evolving electrode and a platinum foil as hydrogen evolving electrode. An aqueous solution of 0.5 M Na_2SO_4 was used as the electrolyte. The evolved hydrogen was measured using a calibrated gas chromatograph (GC 2014, Shimadzu) equipped with a thermal conductivity detector.

4.3 Results and Discussions

4.3.1 2D Morphology of Ilmenene

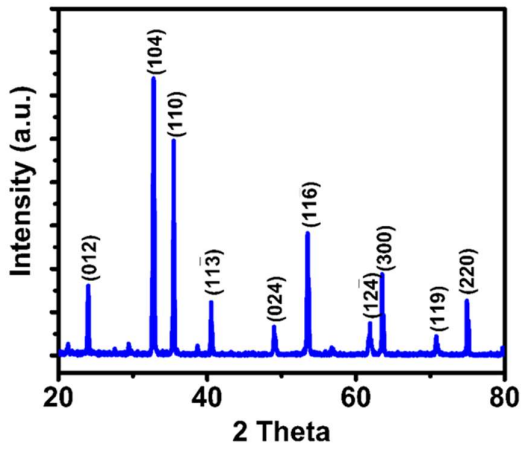

Figure 4.2. XRD of pristine Ilmenite powder

Naturally occurring ilmenite ore was powdered using a mortar and pestle. As obtained pristine powder was subjected to X-ray diffraction (XRD) (***Figure.4.2***). The XRD pattern confirms the crystallinity of ilmenite with rhombohedral geometry (JCPDS file 075-1208) having $R\bar{3}$ space group. The obtained powder was subjected to ultrasonic cavitation in Dimethylformamide (DMF) for 50 hours (see Methods section for the detailed description of sample preparation) to obtain ilmenene.

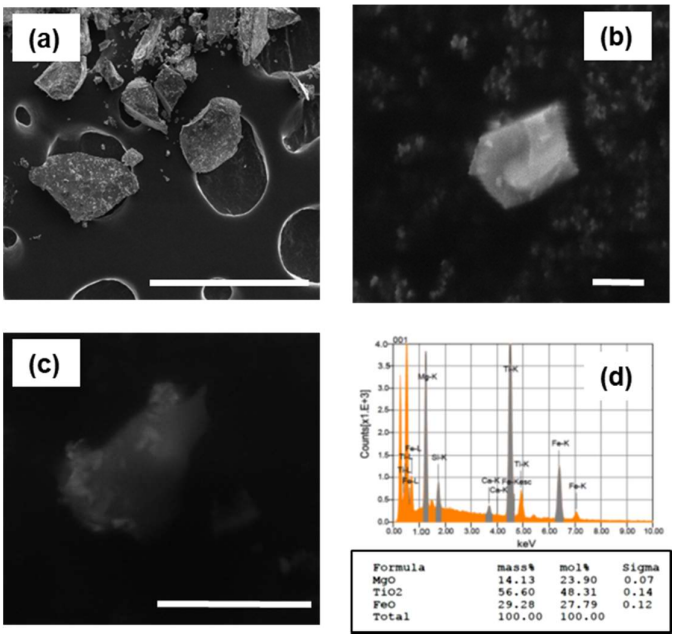

Figure 4.3 Scanning electron micrographs of ***(a)*** pristine ilmenite (scale bar 400µm). ***(b) & (c)*** ilmenene (scale bar 1µm & 3µm respectively), and ***(d)*** WDS elemental analysis of ilmenene.

Pristine as well as exfoliated samples were subjected to scanning electron microscopy (SEM) and wavelength dispersive spectroscopy (WDS) analysis (***Figure 4.3 a-d***). It is evident from scanning electron micrographs (***Figure. 4.3a & 4.3b-c***) that the exfoliation has resulted in

well-separated ilmenene sheets. The elemental composition of these ilmenene sheets studied by using field emission electron-probe microanalysis (FE-EPMA) equipped with WDS (***Figure. 4.3d***) gives a 1:1:3 ratio of iron, titanium and oxygen. Usually, Mg is also observed as an impurity and it is common in ilmenite ores. Mg substitutes for Fe or Ti in the original ilmenite lattice which is evident from WDS result.[14]

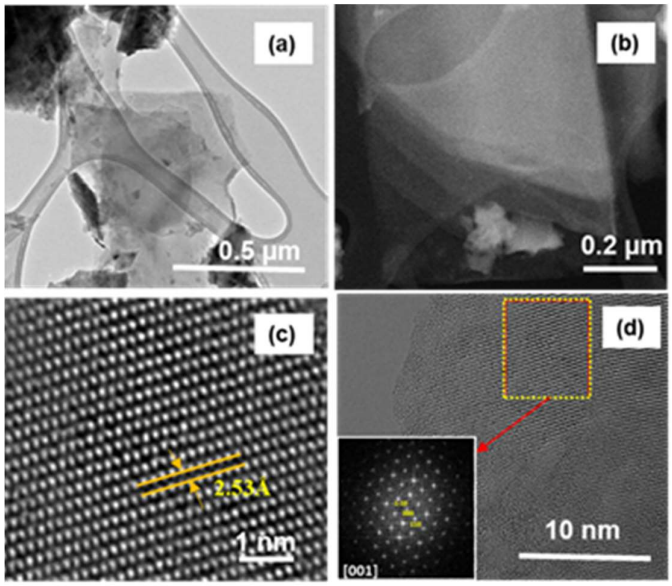

Figure 4.4 2D Morphology: (a) Bright field TEM images (scales bar 0.5µm) showcasing mono and bilayer ilmenene sheets; ***(b)*** Dark-field TEM images (scale bar 0.2 µm) of a multilayer stack of ilmenene sheets ; ***(c)*** HRTEM (scale bar 1 nm); interplanar spacing of 2.53 Å, corresponding to the $(11\bar{2}0)$ and $(\bar{2}110)$ lattice spacing of the ilmenite structure signifying (001) plane; ***(d)*** HRTEM (scale bar 10 nm) with Fourier transform in the inset.

To confirm the 2D nature and crystallinity, ilmenene sheets were subjected to transmission electron microscopy (TEM) measurements. The transmission electron micrographs (***Figure. 4.4a&b***) indicate the formation of mono and few-layer ilmenene sheets. Fellows, et al.[15]

showed that [001] surface of ilmenite is the most stable one and discussed the various possible configurations of [001] surface. The ilmenene sheet in [001] orientation in which the inter-planar spacing of 2.53 Å, corresponding to $11\bar{2}0$ and $\bar{2}110$ lattice spacing of the ilmenite structure, is shown in ***Figure. 4.4c***. From the high-resolution TEM (HRTEM) images (***Figure. 4.4c-d***), it can be clearly seen that the ilmenene sheets are of unique orientation [001], corresponding to (001) faceted planes. These HRTEM images along with the associated Fourier transforms (inset) suggests that the atoms are arranged hexagonally.

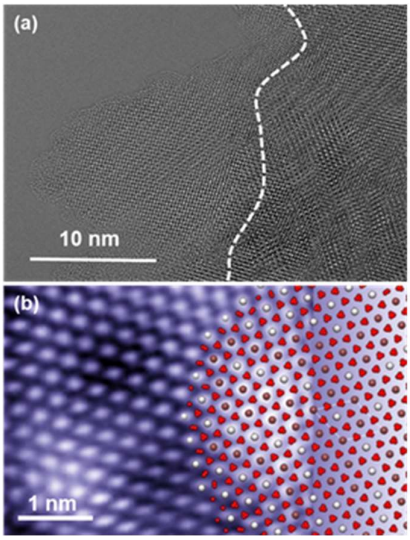

Figure 4.5 (a) TEM (scale bar 10 nm) showing misaligned stacks of ilmenene sheets; and, ***(b)*** HRSTEM (1 nm) showing individual constituent atoms at (001) ilmenene sheets (color codes of atoms – Fe (brown), Ti (white) and O (red)).

Figure. 4.5a shows an HRTEM image of a bilayer stack of ilmenene sheets. The change in crystallinity across the sheet edge (shown by a white dash) signifies random stacking of sheets. HRSTEM (***Figure. 4.5b***) image in which individual atomic contrasts are visible (highlighted by colour codes – Fe (brown), Ti (white) and O (red)).

The thickness of exfoliated sheets was measured using an atomic force microscope (AFM) (***Figure. 4.6***). Most of the sheets are of thickness ~ 2 nm corresponding to 3-4 monolayers.

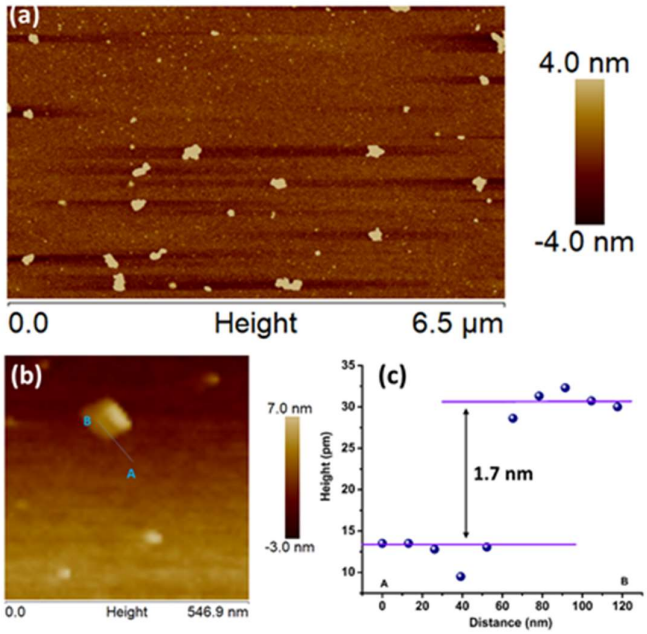

Figure. 4.6. AFM of an ilmenene sheets. ***(a)*** Ilmenene sheets drop cast on a silicon substrate. ***(b)*** An enlarged view of one single sheet. ***(c)*** Line profile of section AB gives the thickness of the ilmenene sheet (~1.7 nm).

4.3.2 Mechanism of Exfoliation and Stability

A plausible mechanism of exfoliation is put forth based on the above results. It is known that crystals generally having certain planes of atoms oriented in a particular direction possess weaker bonding (ie., high broken bond density) when compared to planes of atoms oriented in a different direction.[16] For example, hematite and ilmenite (corundum crystals), [001] oriented planes have weaker atomic bonds. In addition to that, alternate anion and cation layers induce a dipole moment perpendicular to the planes resulting in reduced stability. Thus, as we apply suitable ultrasonic energy, the hydrodynamic forces cleave the crystal in [001]

direction to obtain [001] oriented planes. From a first look, cleavage along Fe^{2+} or Ti^{4+} is possible due to the presence of two different sites of cations within a single cation layer.[15] The relaxed structures of Fe-terminated and Ti Terminated ilmenene sheets are depicted in ***Figure 4.7a-d*** and are simulated using Virtual NanoLab version 2016.2. The thickness of the relaxed structure for Fe-terminated ilmenene is found to be 3.33 Å.

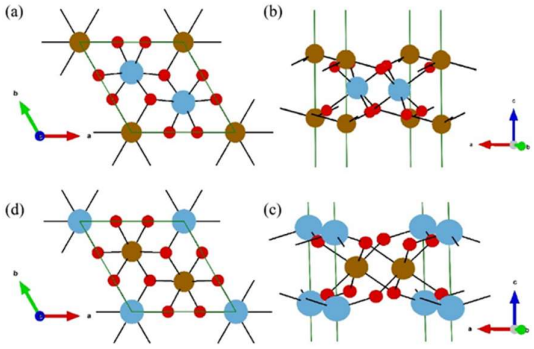

Figure 4.7. (a) & (b) Crystal structure of Fe-terminated (001) ilmenene as seen from top and side views, respectively. ***(c) & (d)*** Crystal structure of Ti-terminated (001) ilmenene as seen from top and side views, respectively.

Figure 4.8. Mechanism of exfoliation of bulk ilmenite in [001] direction. Exfoliation direction is indicated by yellow arrows. Atom colour codes; Fe (brown), Ti (white) and O (red).

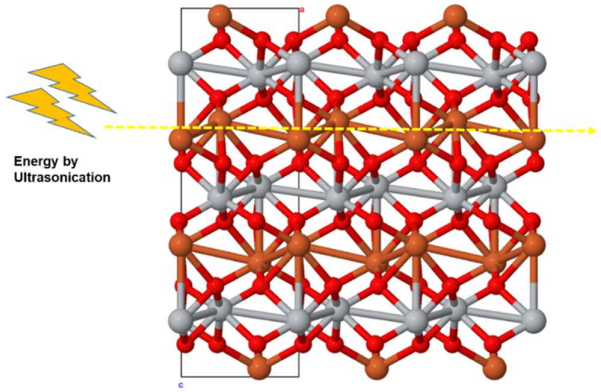

However, when we apply external energy by means of ultrasonic waves, cleavage along Fe^{2+} layers occurs since Fe-termination is energetically favourable. A schematic showing the mechanism of exfoliation is shown in ***Figure 4.8***.

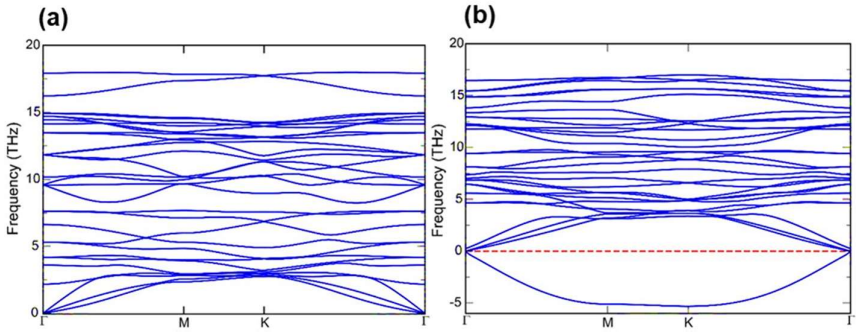

Figure 4.9. Phonon dispersion of ***(a)*** Fe-terminated and ***(b)*** Ti-terminated ilmenene sheets.

The stability of Fe-terminated and Ti-terminated ilmenene sheets is investigated by means of phonon dispersion (See ***Figure 4.9***) using Vienna Ab initio Simulation Package (VAFP)-Density Functional Perturbation Theory (DFPT) calculations in Phonopy software[17] and Fe-terminated ilmenene is found to be dynamically stable. A negative phonon frequency of phonons in the phonon dispersion of Ti-terminated ilmenene implies the dynamic instability of Ti-termination. Also, recently scientists have examined a number of possible terminations of ilmenite [001] surface using B3LYP (Becke, three-parameter, Lee-Yang-Parr) functional theory and proved that Fe terminated surfaces are having the lowest cleavage energy.[18] This is in accordance with what we have anticipated.

4.3.3. Characterization of ilmenene

The bulk ilmenite and the 2D ilmenene were analyzed using Renshaw inVia Raman microscope with a 50x objective using He-Ne laser of wavelength 632.8 nm with a spot size of 1µm. The recorded spectra are depicted in ***Figure.4.10***. Based on the group theory analysis of ilmenite, ten Raman active lattice vibration modes are predicted, which are assigned based on atomic vibrations. In that, $A_{g(1)}$ and $E_{g(1)}$ modes correspond to Ti-O stretching modes, $A_{g(2)}$, $A_{g(3)}$, $E_{g(2)}$ and $E_{g(3)}$ corresponds to O-Ti-O bending motions, $A_{g(4)}$ and $E_{g(4)}$ represent the translations of the TiO_6 octahedra against Fe^{2+} cations, and $E_{g(5)}$ signifies the translations of the Fe2+ cation against the oxygen framework.

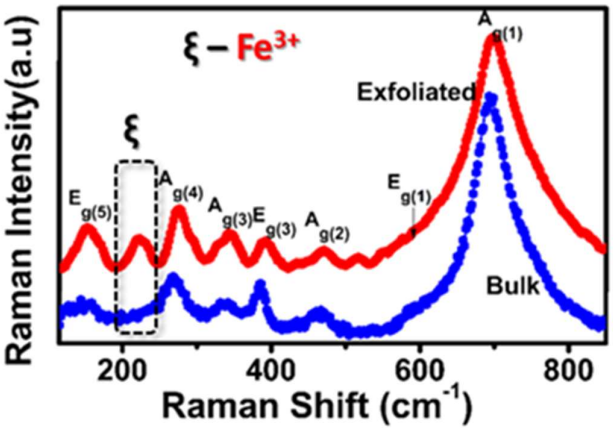

Figure 4.10. Raman spectrum of bulk ilmenite and ilmenene.

It may be noted here that though all the ten modes could not be observed in bulk ilmenite and ilmenene, we could identify distinct modes centred at 152 cm^{-1}, 275 cm^{-1}, 342 cm^{-1} , 392 cm^{-1} , 470 cm^{-1}, 592 cm^{-1} and 698 cm^{-1} corresponding to $E_{g(5)}$, $A_{g(4)}$, $A_{g(3)}$, $E_{g(3)}$, $A_{g(2)}$, $E_{g(1)}$ and $A_{g(1)}$ respectively, thereby confirming the presence of the ilmenite phase.[19] All the Raman modes of ilmenene are blue shifted with respect to the pristine ilmenite and are attributed to the phonon confinement exhibited by

materials at reduced dimensions. Structural reconstruction on exfoliation to 2D from bulk can also be a contributing factor for the shift in Raman modes as reported by Lee et. al. in single layer MoS_2.[20] In terms of the intensities of the distinct Raman modes ($E_{g(5)}$, $A_{g(4)}$, $A_{g(3)}$, $E_{g(3)}$ and $A_{g(2)}$), intensity of the lower order modes ($E_{g(5)}$, $A_{g(4)}$ and $A_{g(3)}$) enhances on exfoliation whereas intensity of modes at higher frequencies ($E_{g(3)}$ and $A_{g(2)}$) diminishes. The enhancement in intensity is due to the optical interference of the excitation laser and the emitted Raman radiation while the reduction is due to the non-availability of the sample for laser interaction. A notable observation is that a Raman mode centred at 222 cm^{-1}, corresponding to Fe_2O_3 (Fe^{3+}) phase, was found in ilmenene which has not shown up in the pristine ilmenite. This is due to the charge transfer excitations ($Fe^{2+} + Ti^{4+} \rightarrow Fe^{3+} + Ti^{3+}$) occurring between iron and titanium atoms at reduced dimensions.[21]

Both ilmenite and ilmenene samples were subjected to X-ray photoelectron spectroscopy (XPS). The high-resolution spectra of Fe 2p, Ti 2p and O 1s of bulk ilmenite and ilmenene are given in ***Figure. 4.11a&b*** respectively. In ***Figure. 4.11a***, the Fe2p spectrum of ilmenene refers to 3+ oxidation state of Fe having a $Fe2p_{3/2}$ peak centred at 710.9eV.[22, 23] The Ti2p spectra indicate a 3+ oxidation for Ti as well ($Ti2p_{3/2}$ centred at 458 eV), thereby confirming $Fe^{3+}Ti^{3+}$ charge ordering in ilmenene. The bulk ilmenite is found to have both Fe^{2+} (lower binding energy) and Fe^{3+} states (***Figure. 4.11b***).

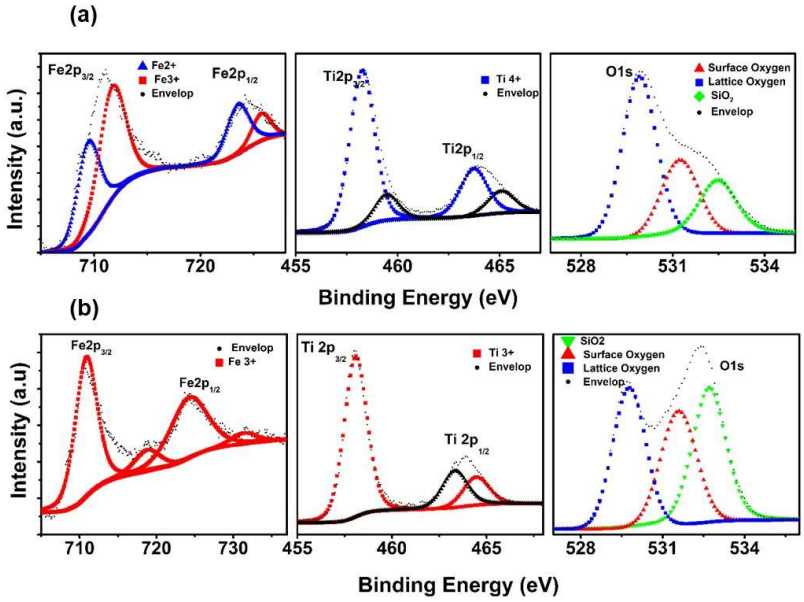

Figure 4.11. XPS of ***(a)*** Pristine ilmenite; and, ***(b)*** ilmenene

The presence of Fe^{3+} ions in the pristine ilmenite is due to the inter-valence charge transfer from Fe^{2+} to Ti^{4+},[24] whereas titanium doublets signify Ti^{4+} state with slightly higher binding energy. The reduced oxidation state of titanium atoms in ilmenene could also be due to the surface effect of the ultrathin metal oxide nanosheets. The surface atoms have a tendency to gain electrons (reduction) from surrounding oxygen atoms and to get reduced from the Ti^{4+} to the Ti^{3+} state as explained by Sun et. al.[25] Further, the peak with an O1s binding energy around 529.8 eV indicates that the oxygen atoms exist as O^{2-} species (lattice oxygen) and that of at 531.6 eV reveals the presence of adsorbed oxygen on the surface of $FeTiO_3$. The peak at 532.7eV could be assigned to the Si-O bond of the Si/SiO_2 wafer.[26] An appreciable increase in the ratio of surface to lattice oxygen was noticed and is found to be greater in the case of the

exfoliated sample compared to pristine ilmenite which is further supporting evidence to the 2D morphology of ilmenene.

4.3.4 Magnetic properties of ilmenene

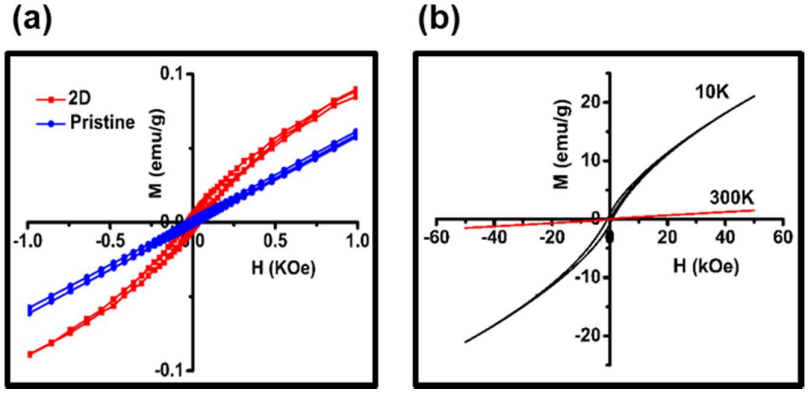

Figure. 4.12 M-H hysteresis measurements of ***(a)*** pristine and 2D ilmenite at 300 K, and ***(b)*** ilmenene at 300 K and at 10 K.

The M–H loops for pristine and exfoliated $FeTiO_3$ were measured at room temperature with an applied field between -50 and 50 kOe (in the figure, -1 to 1 kOe range is shown in order to get the clear contrast of the loops) and are shown in ***Figure. 4.12a***. At low fields (<1000 Oe), a visible non-linearity is observed in the case of ilmenene whereas no such deviation from paramagnetic behaviour is noticed for pristine ilmenite. This could be because of the introduction of anisotropy due to surface spins.[27] As a result of the introduction of anisotropy in ilmenene, an enhancement in coercivity and remanent magnetization is observed (***Figure. 4.13c&d***). Low temperature (10K), below T_N ~ 55 K (see ***Figure 4.13 a &b***), M-H loop of ilmenene was plotted and compared with room-temperature M-H plot (***Figure. 4.12b***). A huge enhancement coercivity (~ 25 times) was observed which reinforces the contribution of surface spins to the

anisotropy. In addition to the experimental evidence, ilmenene is purported to exhibit ferromagnetic order which is confirmed by DFT calculations and is discussed in the following section.

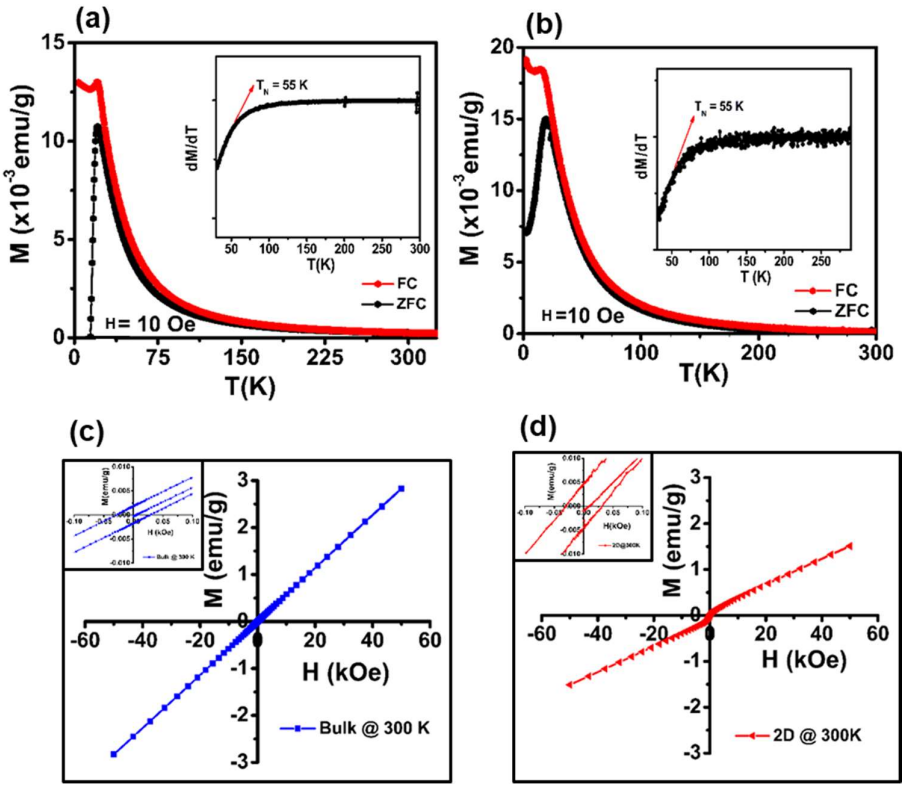

Figure. 4.13. FC-ZFC magnetization of ***(a)*** pristine and ***(b)*** ilmenene; Room temperature hysteresis of ***(c)*** bulk ilmenite and ***(d)*** ilmenene, with the respective zoom in views in the inset.

Raman and XPS analysis confirm the considerable increase of Fe^{3+}/Ti^{3+} charge ordering state in ilmenene whereas it is less prominent in the pristine sample. According to Hartree-Fock theory, Fe^{3+}/Ti^{3+} charge ordering of cations will favour ferromagnetic (FM) ordering. So, in addition to the surface effects, the charge transfer excitation from $Fe^{2+}Ti^{4+}$

to $Fe^{3+}Ti^{3+}$ in ilmenene could be another contributing factor for the observed anisotropy. It is also observed that at room temperature, M–H loop did not saturate even up to a field of 50 kOe which is due to the predominant paramagnetic phase of ilmenene.[28, 29]

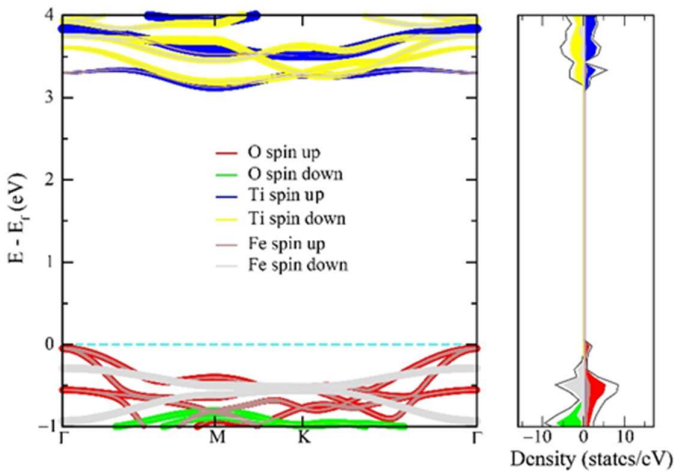

Figure 4.14. Electronic bandstructure and PDOS of [ferromagnetic; Fe-terminated; (001)] ilmenene, as calculated from the DFT+U method.

Theoretical calculations based on DFT were performed to substantiate the experimental findings. The calculations were performed using DFT+U approach,[30] as implemented in the Vienna ab initio simulation package (VASP),[31] as DFT underestimate the strong on-site Coulomb repulsion of transition metal d-electrons. Electron-ion interactions were described using all-electron projector augmented wave pseudopotentials, and Perdew-Burke-Ernzerhof (PBE) generalized gradient approximation (GGA),[32] was used to approximate electronic exchange and correlation. The Brillouin zone had been sampled using a well-converged Monkhorst-Pack scheme. All the structures were relaxed using a conjugate gradient

scheme until the energies and forces converged to 10^{-5} eV and 0.01 eV $Å^{-1}$. The value of U (Hubbard parameter) was varied from 1 to 8 and that of J (on-site Coulomb interaction) was fixed to be 1, for both Fe and Ti atoms. The structures of slabs were generated using Virtual NanoLab version 2016.2

The energies and bandgap values of ferromagnetic and antiferromagnetic configurations of both Fe and Ti-terminated (***Table. 4.2***& ***Table. 4.3*** respectively) (001) planes were evaluated. The energies of Fe-terminated ilmenene are lower than that of Ti-terminated ones for all values of U together with dynamic stability (*Section 4.3.2*), exfoliated ilmenene are predominantly Fe-terminated. Calculations carried out at 0 K points towards a less stable ferromagnetic configuration of (001) ilmenene, however, since the difference between ferromagnetic and antiferromagnetic configurations (ΔE_{FM-AFM}) is only 7.40 meV/unit cell (U=7, J=1), the possibility of ilmenene exhibiting ferromagnetic ordering at room-temperature is high. The difference in magnetic ordering between bulk and the monolayer arises due to the presence of antiferromagnetic coupling between the adjacent Fe layers (interlayer Fe–Fe direct exchange) in bulk, whereas an individual layer is always ferromagnetic. The results for magnetic ordering in the ferromagnetic phase is summarized in ***Table. 4.4*** and that of antiferromagnetic ordering in bulk is given in ***Table 4.5***. The magnitude of the local magnetic moment of iron increases to 3.77 μB due to the presence of Fe^{3+} ions. The band gap of ferromagnetic (001) ilmenene is indirect in nature (Γ→M) and has a band gap of 3.15 eV (U=7, J=1) (Refer ***Figure 4.14***), which matches exactly with experimental value (given in the photocatalysis section).

Table 4.2. Energy and bandgap values of antiferromagnetic and ferromagnetic configurations of Fe-terminated ilmenene as a function of U.

U [eV]	E_{AFM} [eV/unit cell]	E_{FM} [eV/unit cell]	E_{FM-AFM} [meV/unit cell]	E_g(AFM) [eV]	E_g(FM) [eV]
1	-81.6167	-81.7401	-123.45	0.41	0.06
2	-78.9930	-78.9443	48.65	0.90	0.46
3	-76.5085	-76.4757	32.77	1.42	1.05
4	-74.1483	-74.1260	22.23	1.97	1.66
5	-71.9039	-71.8887	15.28	2.54	2.28
6	-69.7703	-69.7597	10.59	3.09	2.87
7	-67.7436	-67.7362	7.40	3.53	3.15
8	-65.8220	-65.8169	5.08	3.75	3.39

Table 4.3. Energy and bandgap values of antiferromagnetic and ferromagnetic configurations of Ti-terminated ilmenene as a function of U.

U [eV]	E_{AFM} [eV/unit cell]	E_{FM} [eV/unit cell]	E_{FM-AFM} [meV/unit cell]	E_g(AFM) [eV]	E_g(FM) [eV]
1	-78.5836	-78.6771	-93.53	0.00	0.00
2	-75.7235	-75.9783	-254.80	0.14	0.00
3	-73.0791	-73.0021	77.02	0.47	0.00
4	-70.5927	-70.8070	-214.27	0.88	0.61
5	-68.2340	-68.8018	-567.84	1.35	1.40
6	-66.9217	-66.9291	-7.34	2.45	2.14
7	-63.8661	-65.1927	-1326.67	2.10	2.55
8	-63.5676	-63.6000	-32.04	2.92	2.54

Table 4.4. Local magnetic moments of transition metal atoms of Fe-terminated ilmenene for ferromagnetic phase (U=7, J=1).

Species	Local magnetic moment (μ)	Species	Local magnetic moment (μ)
Fe1	3.77	Ti1	0.10
Fe2	3.77	Ti2	0.10
μ_{avg}	3.77	μ_{avg}	0.10

Table 4.5. Local magnetic moments of transition metal atoms of bulk ilmenite for antiferromagnetic phase (U=7, J=1).

Species	Local magnetic moment (|μ|)	Species	Local magnetic moment (|μ|)
Fe_1	3.46	Ti_1	0.07
Fe_2	3.49	Ti_2	0.17
Fe_3	3.51	Ti_3	0.06
Fe_4	3.54	Ti_4	0.04
Fe_5	3.50	Ti_5	0.18
Fe_6	3.46	Ti_6	0.05
μ_{avg}	3.49	μ_{avg}	0.09

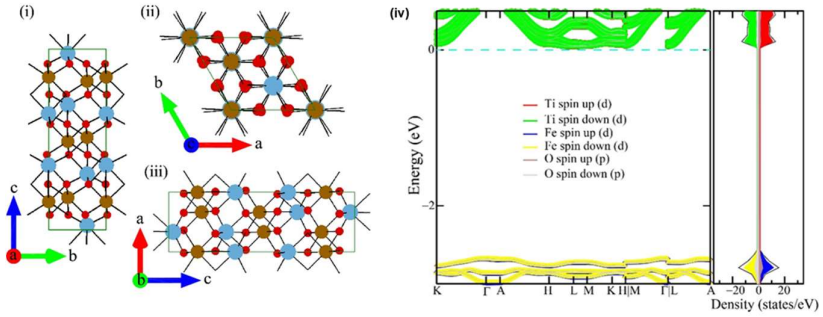

Figure 4.15 *(i), (ii) & (iii)* Crystal structure of bulk ilmenite as seen from a, c and b axes, respectively. Brown, blue and red colours denote Fe, Ti and O atoms, respectively. *(iv)* Electronic bandstructure and projected density of states (PDOS) of bulk ilmenite, as calculated from the DFT+U method.

Theoretical calculations were performed for the bulk ilmenite system as well for comparison. The optimized lattice parameters of bulk ilmenite are found to be: a = b = 5.02 Å and c = 13.64 Å (***Figure. 4.15 (i), (ii) & (iii)***). The antiferromagnetic phase of bulk ilmenite has been found to be more stable than that of ferromagnetic in previous theoretical reports.[2, 33]. We could see that $\mu_{Fe} \approx 3.5$ μB and $\mu_{Ti} \approx 0$ μB, corresponding to Fe^{2+} and Ti^{4+} ions, respectively. Experimental observations also yielded major proportions of these ions in the bulk. The electronic band structure for the

antiferromagnetic phase is shown in ***Fig. 4.15 (iv)***, where its band gap was obtained to be 2.72 eV.

4.3.5 Photocatalytic Activity of Ilmenene

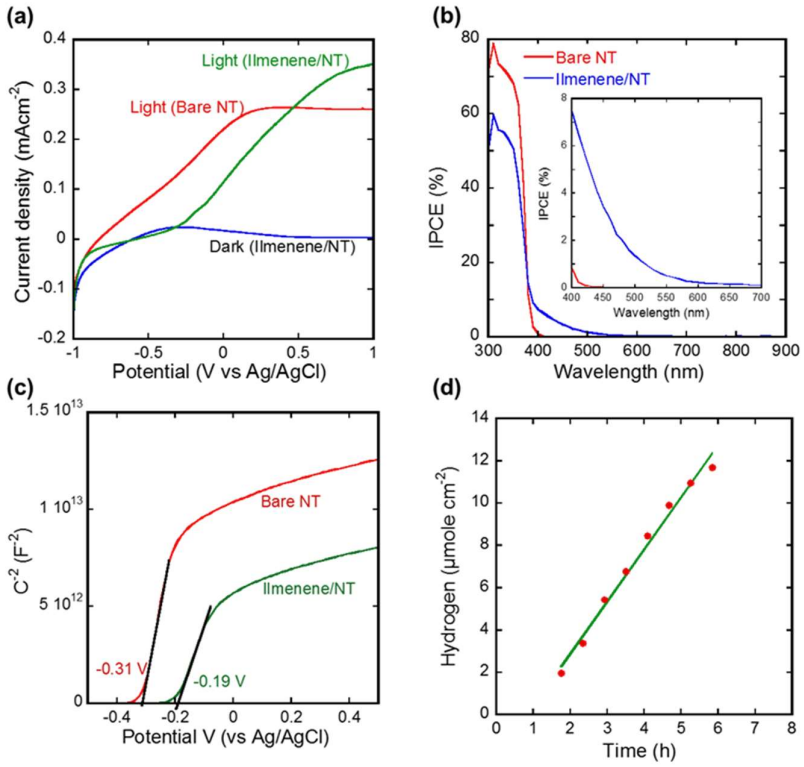

Figure 4.16. Photoelectrochemical studies: (a) Current measured using linear potential sweep under illumination and dark conditions; ***(b)*** IPCE spectra recorded from bare NT and $FeTiO_3$/TNT photoanodes; ***(c)*** Mott-Schottky curves; and, ***(d)*** Hydrogen evolution with time.

The photocatalytic activity of the ilmenene-titania nanotube heterojunction (2D $FeTiO_3$/TNT) was carried out and the findings are summarized in ***Figure 4.16***. ***Figure. 4.16a*** shows the current measured using linear potential sweep under illumination and dark conditions. Compared to bare titania nanotubes (TNTs), the 2D $FeTiO_3$/TNT

electrode yielded a higher photocurrent. On the other hand, the onset potential shifted and became more positive. ***Figure. 4.16b*** shows the incident photon to current conversion efficiency (IPCE) spectra recorded from bare NT and 2D $FeTiO_3$/TNT photoanodes. It is evident that bare nanotubes resulted in very high IPCE (70-80%) at UV wavelengths and almost zero at wavelengths greater than ~ 400 nm. On the other hand, 2D $FeTiO_3$/TNT showed significant IPCE (~ 7% at 400 nm) up to about 550 nm. Such a high IPCE at visible light wavelengths has not been reported on any $FeTiO_3$ based heterojunction electrodes except by Ginley and Butler, where they obtained 15% IPCE at 350 nm in single crystal $FeTiO_3$.[34] Non-zero IPCE at below band gap energy range indicate the transfer of electrons from the conduction band of ilmenene to that of titania nanotubes. No external bias was applied between the electrodes for IPCE measurements.

Under solar irradiation, the photo-generated holes in ilmenene and TiO_2 could oxidize the electrolyte species. The concurrent photogenerated electron transport towards the titanium substrate carrying $FeTiO_3$ sensitized titania nanotubes establishes a photocurrent in the external circuit. In order to have a photocurrent generated under visible light photon irradiation, the charges should be originating from ilmenene and electrons transported to titanium dioxide NTs. The effective carrier separation at the ilmenene-titania NT (1D) interface is believed to have made this electron injection possible.

The high IPCE of the bare titania NT film electrode at ultraviolet (UV) wavelengths (***Figure. 4.16b***) portrays NT as an effective electron transport medium. The bare NT electrodes showed no photocurrent under below bandgap irradiation. The ilmenene prepared on FTO glass showed negligible light absorption. Thus, the titania nanotubes here played the role of a high surface area support for ilmenene to enhance the visible light absorption, as an electron acceptor (from ilmenene), as the electron transport medium and a photocatalyst utilizing the UV region of the solar spectrum. The IPCE in the UV region diminished slightly upon loading ilmenene on titania nanotubes. ***Figure. 4.17*** shows the SEM images of bare and ilmenene loaded titania nanotube array films. Although it is difficult to recognize ilmenene on the walls of nanotubes, thick sheets of $FeTiO_3$ can be seen on the surface of nanotubes. These thick sheets are aggregates from colloidal solution since exfoliation of non-layered solids will result in thick layers along with monolayers of the material and is difficult to separate by mere ultracentrifugation. Upon accumulation on the surface, they inhibit the photocatalytic properties.

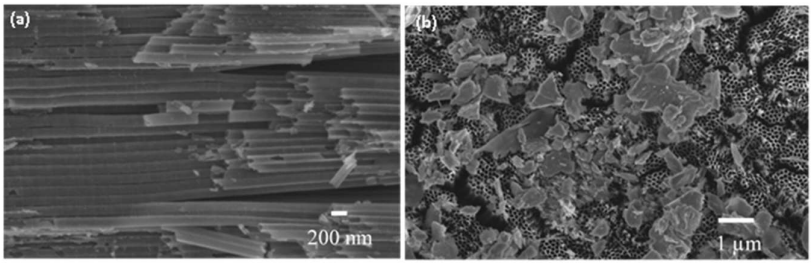

Figure 4.17. SEM images showing the ***(a)*** lateral and ***(b)*** top views of the titania nanotubes loaded with ilmenene. While FeTiO3 aggregates can be seen on the top surface of the nanotubes, the 2D sheets on the walls of the nanotubes cannot be discerned.

$FeTiO_3$ is reported to have more positive flat band potential (vs NHE) than TiO_2.[35] Mott-Schottky curves (***Figure. 4.16c***) obtained from bare TiO_2 NT and 2D $FeTiO_3/TiO_2$ NT electrodes showed a positive shift (120 mV) in the flat band potential of NTs upon loading ilmenene. Evidently, the shift was caused by the more positively (vs Ag/AgCl) located conduction band of ilmenene. In such a situation, the electron transfer from the conduction band bottom of ilmenene to that of TiO_2 NT is less likely. We believe that the observed external quantum efficiency (IPCE) at wavelengths above 400 nm is primarily due to the excitation of electrons to the higher energy states in the conduction band that are positioned appropriately for transferring electrons to the conduction band of TiO_2 NTs.

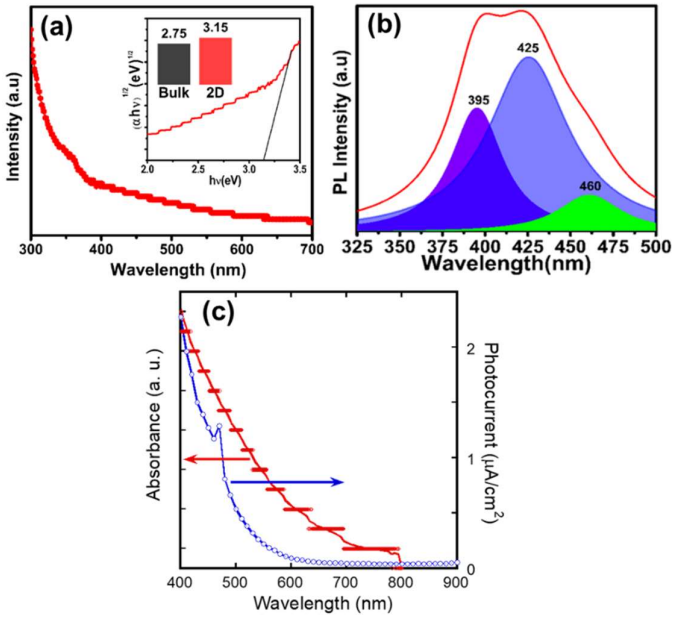

Figure 4.18. (a) Band gap energy of ilmenene and is found to be 3.15 eV (Tauc plot in the inset); ***(b)*** Photoluminescence spectra of ilmenene***;*** and ***(c)*** A comparison of the absorbance spectrum of ilmenene and photocurrent spectrum of ilmenene-titania nanotube array electrode in the visible light region.

Although the bandgap of ilmenene was found to be about 3.15 eV, the visible light absorption in ilmenene apparently arises from the defect states in the bandgap. This is evident from the weak light absorption in the 400-700 nm region (see ***Figure. 4.18a***). ***Figure. 4.18c*** shows a comparison of the visible light photocurrent and absorbance spectra. Both these physical quantities have non-zero magnitudes even in the below-bandgap wavelength region (> 400 nm), but the photocurrent diminishes quickly and becomes zero at about 550 nm while absorbance spectrum extends further till ~700 nm. The quantum efficiency spectrum (***Figure. 4.16b***) essentially follows the photocurrent trend. The result indicates that excitation to higher energy levels in the ilmenene conduction band occurs from the defect states that are apparently staying closer to the valence band. Photoluminescence spectrum of ilmenene having visible emission (around 460 nm) provides further evidence for the presence of defect states (***Figure. 4.18b***).

IPCE integrated over the AM1.5 (global) solar spectrum in the wavelength region above 350 nm (the cut off wavelength for the AM1.5 filter is ~ 350 nm) showed the photocurrent as 0.42 and 0.48 mA/cm^2 respectively for bare and ilmenene loaded TiO_2NT electrodes.[36] The lower IPCE in the UV region limited the photocurrent enhancement in the 2D $FeTiO_3/TiO_2$ NT system. The hydrogen evolution was verified by conducting experiments using a two-electrode photoelectrochemical (PEC) cell consisting of a 2D $FeTiO_3$/NT anode and platinum cathode (see 'Experimental' for a detailed description). A voltage bias (0.9 V) was applied between the two electrodes. ***Figure. 4.16d*** shows the hydrogen

evolution from the platinum electrode with time. We note that although $FeTiO_3$ was investigated for photocatalytic decomposition of organics and half-cell oxygen evolution from water using electron acceptors, to the best of our understanding this is the first report on hydrogen generation using a full PEC cell.

4.4 Conclusion

In conclusion, this work demonstrates the synthesis of a new 2D material 'ilmenene' from a non-layered naturally occurring titania ore precursor, ilmenite, by means of liquid exfoliation. Naturally occurring minerals can act as excellent precursors for the exfoliation of novel 2D materials with improved properties with respect to their bulk counterparts. Ilmenene exhibits a weak FM ordering at room temperature owing to the charge transfer excitations and surface spin induced anisotropy. DFT calculations confirm the FM ordering in ilmenene. The successful exfoliation by a simple method to get a 2D non-van der Waals solid is a further motivation to discover new and novel analogues of 2D materials from altogether different non-layered precursors. The visible photocatalytic activity of anatase TiO_2 was enhanced upon sensitizing it with ilmenene despite having a conduction band offset impeding low energy electron injection to titania. The results indicate that ilmenene could be used in conjunction with stable wide bandgap semiconductors for developing efficient visible light photocatalysts for hydrogen generation.

4.5 References

1. A. Puthirath Balan, S. Radhakrishnan, C. F. Woellner, S. K. Sinha, L. Deng, C. d. l. Reyes, B. M. Rao, M. Paulose, R. Neupane, A. Apte, V. Kochat, R. Vajtai, A. R. Harutyunyan, C.-W. Chu, G. Costin, D. S. Galvao, A. A. Martí, P. A. van Aken, O. K. Varghese, C. S. Tiwary, A. Malie Madom Ramaswamy Iyer and P. M. Ajayan, *Nature Nanotechnology*, 2018, **13**, 602-609.
2. N. C. Wilson, J. Muscat, D. Mkhonto, P. E. Ngoepe and N. M. Harrison, *Physical Review B*, 2005, **71**, 075202.
3. D. M. Sherman, *Physics and Chemistry of Minerals*, 1987, **14**, 355-363.
4. J. Luxa, O. Jankovsky, D. Sedmidubsky, R. Medlin, M. Marysko, M. Pumera and Z. Sofer, *Nanoscale*, 2016, **8**, 1960-1967.
5. S. Lee, K.-Y. Choi, S. Lee, B. H. Park and J.-G. Park, *APL Mater.*, 2016, **4**, 086108.
6. M. W. Lin, H. L. L. Zhuang, J. Q. Yan, T. Z. Ward, A. A. Puretzky, C. M. Rouleau, Z. Gai, L. B. Liang, V. Meunier, B. G. Sumpter, P. Ganesh, P. R. C. Kent, D. B. Geohegan, D. G. Mandrus and K. Xiao, *Journal of Materials Chemistry C*, 2016, **4**, 315-322.
7. N. Sivadas, M. W. Daniels, R. H. Swendsen, S. Okamoto and D. Xiao, *Physical Review B*, 2015, **91**.
8. J. He, S. Ma, P. Lyu and P. Nachtigall, *Journal of Materials Chemistry C*, 2016, **4**, 2518-2526.
9. Z. Zhang, X. Zou, V. H. Crespi and B. I. Yakobson, *ACS Nano*, 2013, **7**, 10475-10481.
10. M. Kan, J. Zhou, Q. Sun, Y. Kawazoe and P. Jena, *Journal of Physical Chemistry Letters*, 2013, **4**, 3382-3386.
11. B. Huang, G. Clark, E. Navarro-Moratalla, D. R. Klein, R. Cheng, K. L. Seyler, D. Zhong, E. Schmidgall, M. A. McGuire, D. H. Cobden, W. Yao, D. Xiao, P. Jarillo-Herrero and X. Xu, *Nature*, 2017, **546**, 270.
12. M. Bonilla, S. Kolekar, Y. Ma, H. C. Diaz, V. Kalappattil, R. Das, T. Eggers, H. R. Gutierrez, M.-H. Phan and M. Batzill, *Nature Nanotechnology*, 2018, **13**, 289-293.
13. E. Brok, M. Sales, K. Lefmann, L. T. Kuhn, W. F. Schmidt, B. Roessli, P. Robinson, S. A. McEnroe and R. J. Harrison, *Physical Review B*, 2014, **89**, 054430.

14. A. Mehdilo, M. Irannajad and B. Rezai, *Minerals Engineering*, 2015, **70**, 64-76.
15. R. A. Fellows, A. R. Lennie, A. W. Munz, D. J. Vaughan and G. Thornton, *American Mineralogist*, 1999, **84**, 1384-1391.
16. Z.-y. Gao, W. Sun and Y.-h. Hu, *Transactions of Nonferrous Metals Society of China*, 2014, **24**, 2930-2937.
17. A. Togo and I. Tanaka, *Scripta Materialia*, 2015, **108**, 1-5.
18. N. C. Wilson and S. P. Russo, *Physical Review B*, 2011, **84**, 075310.
19. X. Wu, S. Qin and L. Dubrovinsky, *Geoscience Frontiers*, 2011, **2**, 107-114.
20. C. Lee, H. Yan, L. E. Brus, T. F. Heinz, J. Hone and S. Ryu, *ACS Nano*, 2010, **4**, 2695-2700.
21. S. Takele and G. R. Hearne, *Journal of Physics: Condensed Matter*, 2004, **16**, 2707.
22. A. P. Grosvenor, B. A. Kobe, M. C. Biesinger and N. S. McIntyre, *Surface and Interface Analysis*, 2004, **36**, 1564-1574.
23. P. García-Muñoz, G. Pliego, J. A. Zazo, A. Bahamonde and J. A. Casas, *Journal of Environmental Chemical Engineering*, 2016, **4**, 542-548.
24. T. Fujii, M. Yamashita, S. Fujimori, Y. Saitoh, T. Nakamura, K. Kobayashi and J. Takada, *Journal of Magnetism and Magnetic Materials*, 2007, **310**, e555-e557.
25. Z. Sun, T. Liao, Y. Dou, S. M. Hwang, M.-S. Park, L. Jiang, J. H. Kim and S. X. Dou, *Nature communications*, 2014, **5**.
26. A. B. Gambhire, M. K. Lande, S. B. Rathod, B. R. Arbad, K. N. Vidhate, R. S. Gholap and K. R. Patil, *Arabian Journal of Chemistry*, 2016, **9, Supplement 1**, S429-S432.
27. S. T. Xu, Y. Q. Ma, G. H. Zheng and Z. X. Dai, *Nanoscale*, 2015, **7**, 6520-6526.
28. T. Varga, A. Kumar, E. Vlahos, S. Denev, M. Park, S. Hong, T. Sanehira, Y. Wang, C. J. Fennie, S. K. Streiffer, X. Ke, P. Schiffer, V. Gopalan and J. F. Mitchell, *Physical Review Letters*, 2009, **103**, 047601.
29. Y. H. Chen, *Journal of Non-Crystalline Solids*, 2011, **357**, 136-139.
30. V. I. Anisimov, J. Zaanen and O. K. Andersen, *Physical Review B*, 1991, **44**, 943-954.
31. G. Kresse and J. Hafner, *Physical Review B*, 1993, **47**, 558.

32. J. P. Perdew, K. Burke and M. Ernzerhof, *Physical Review Letters*, 1996, **77**, 3865-3868.
33. R. A. P. Ribeiro and S. R. de Lazaro, *RSC Advances*, 2014, **4**, 59839-59846.
34. D. S. Ginley and M. A. Butler, *Journal of Applied Physics*, 1977, **48**, 2019-2021.
35. H. P. Maruska and A. K. Ghosh, *Solar Energy*, 1978, **20**, 443-458.
36. O. K. Varghese and C. A. Grimes, *Solar Energy Materials and Solar Cells*, 2008, **92**, 374-384.

Chapter 5

2D Manganese Telluride and its Properties

Manganese Telluride (MnTe) is the only semiconducting material in the transition metal based binary compounds having a hexagonal crystal geometry and exhibiting antiferromagnetic behaviour at room-temperature. This chapter describes the extraction of a 2D material from MnTe by means of liquid phase exfoliation and investigation carried out on the magnetic properties.

ACS Applied Nano Materials *1(11): 6427-6434*

5.1 Introduction

Titanium Sulfide (TiS), Vanadium Phosphide (VP), Iron Sulfide (FeS), Cobalt Sulfide (CoS), Manganese Arsenide (MnAs), Manganese Selenide (MnSe), Manganese Sulfide (MnS), Manganese monoantimonide (MnSb) and Manganese Telluride (MnTe) belong to the family of transition metal based binary compounds and are well known for their magnetic, optical and transport properties.[1-8] Most of these compounds exhibit metallic behaviour and are having NiAs-type hexagonal crystalline structure. However, Manganese Telluride (MnTe), unlike other materials behave as a semiconductor, while a few other binary compounds belonging to the same family (MnSe and MnS) are insulating. The band structure of these materials is in between that of charge transfer and band insulators and hence called "crossroads electronic structure".[9] Historically speaking, the thermal and magnetic properties of MnTe have been investigated from the beginning of the 19th century.[2, 10] However, it was only in the year 1963 the antiferromagnetic property of MnTe was established beyond doubt by neutron diffraction studies, soon after the Neels two sublattice theory was propounded.[11, 12] The discovery of diluted magnetic semiconductors in the seventies gave a further fillip to the ongoing investigations on MnTe.[13, 14] MnTe is a room-temperature antiferromagnetic material having a Neel temperature (T_N) of 307 K.[15] For many years scientists believed that only ferromagnetic materials have applications in spintronics until recent investigations on materials like MnTe proved that anti-ferromagnetic materials are also promising candidates for spintronic applications.[16, 17]

Magnetism in two dimensions (2D) is always fascinating and at the same time, is not unambiguously explained. 2D magnetism has been an

emerging research area ever since the discovery of Graphene.[18] Earlier investigations on magnetic properties of 2D materials suggested that it is tricky to retain the magnetic order down to monolayers as explained by Mermin-Wagner theorem.[19] Efforts are on to realize 2D materials having appreciable magnetic properties which involve different strategies namely impurity doping,[20] introducing defects,[21] and grain boundary engineering.[22] Despite these efforts, it was only recently that scientists isolated a magnetic 2D material: a ferromagnetic monolayer of CrI_3.[23] We have succeeded in isolating two new 2D non-van der Waals materials namely hematene and ilmenene from their ores hematite[24] and ilmenite[25] respectively by means of liquid phase exfoliation. The details are described in the previous two chapters. They were found to be exhibiting ferromagnetic ordering quite different from their antiferromagnetic bulk counterparts. MnTe being antiferromagnetic and non-van der Waal in nature, it was thought that its 2D analogue too would be interesting from a physics point of view.

5.2 Experimental

Sample preparation: Commercially available MnTe (99.9% (metals basis): Gute Chemie) was powdered well by employing mortar and pestle using acetone as the wetting medium. 50 mg of the obtained powder was dispersed in 200 mL of N, N-dimethylformamide (DMF) and ultra-sonicated for 50 hours to obtain a suspension of MnTe sheets. The ultrathin 2D MnTe sheets were separated by centrifugation at RCF value of 10195 (x g) for 30 minutes. Ultrathin 2D sheets of MnTe were isolated by filtering the supernatant liquid and was used for further characterizations.

Characterization: The transmission electron micrographs were acquired using an FEI Titan Themis (s) transmission electron microscope. FEI Quanta high-resolution microscope was employed to obtain scanning electron microscopy (SEM) images. A Bruker multimode 8 microscope was employed in the ScanAsyst mode to obtain atomic force microscopy (AFM) images. Raman spectra were measured in a Renshaw inVia Raman microscope using 632.8 nm laser with a spot size of 1µ. X-ray photoelectron spectroscopy (XPS) measurements were carried out in a PHI Quantera model machine. A Shimadzu 2450 UV-Visible spectrophotometer was employed to obtain UV-Visible absorption measurements whereas, magnetic measurements were carried out by using a magnetic property measurement system (MPMS 3) by Quantum Design.

5.3 Results and Discussion

5.3.1 Confirmation of 2D Morphology

Commercially available manganese telluride is liquid exfoliated in DMF to obtain ultrathin 2D sheets of MnTe (see ***Figure 5.1***. *Schematic*). Pristine MnTe is analyzed using X-ray diffractometer (XRD). The pristine sample is NiAs type polycrystalline MnTe (Refer ***Figure 5.2***) corresponding to a hexagonal structure having P63/mmc space group and lattice constants of a = 4.1475 Å and c = 6.71 Å (ICDD: 01-089-2886). In addition to major MnTe phase, there is a small amount of $MnTe_2$ phase (ICDD: 03-065-3340) which could be due to a non-stoichiometric excess of tellurium compared to manganese.[26]

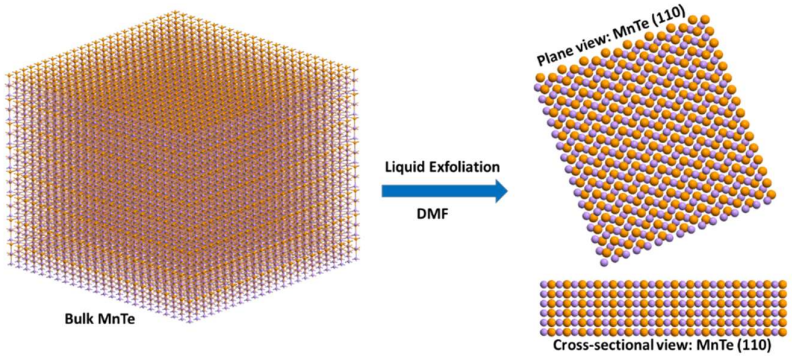

Figure 5.1. Schematic: Liquid exfoliation of manganese telluride in dimethylformamide(DMF) solvent. A planar and cross-sectional view of obtained [110] oriented 2D sheets of MnTe is shown. Manganese and Tellurium atoms are coloured violet and orange respectively.

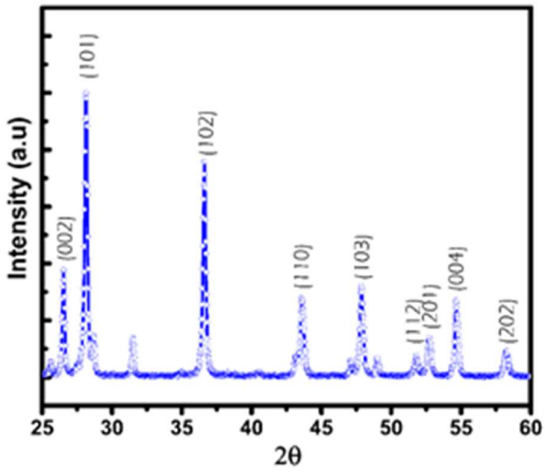

Figure 5.2. X-ray Diffraction of pristine MnTe

The surface morphology of the exfoliated samples was analyzed using a scanning electron microscope (SEM). The obtained scanning electron micrographs (***Figure 5.3a&b***) shows that the exfoliated sheets resemble a sheet morphology. Atomic force microscope (AFM) measurements (***Figure 5.4 & 5.5a***) confirm the ultrathin nature of the sheets.

A low-resolution AFM image is given in ***Figure 5.4*** which shows that most of the exfoliated MnTe sheets are in the thickness range of 2 nm to 3 nm along with a small number of thick (~10 nm) sheets as well.

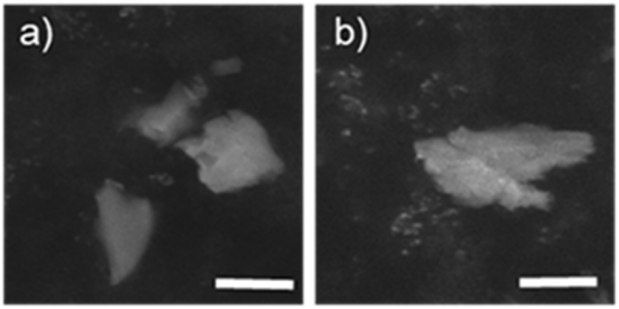

Figure 5.3. Scanning electron micrographs of exfoliated MnTe ***(a)*** & ***(b)*** having a scale bar of 2.5 μm

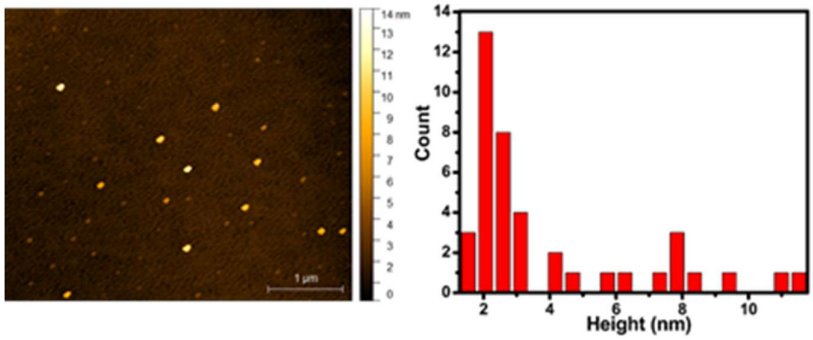

Figure 5.4. AFM image showing a number of exfoliated MnTe sheets having ultrathin thickness.

High angle annular dark field scanning transmission electron microscopy (HAADF-STEM) images of 2D MnTe show well-defined lattice fringes with its Fourier transform (FFT) in the inset (***Figure 5.5c***) confirming the crystallinity of the obtained sheets. (110) planes corresponding to an interplanar distance of 0.207 nm is clearly noticeable in the HAADF-STEM image.[27] Low magnification HAADF-STEM (***Figure 5.5d*****)** and TEM (***Figure 5.5e***) images indicate the 2D nature of exfoliated MnTe.

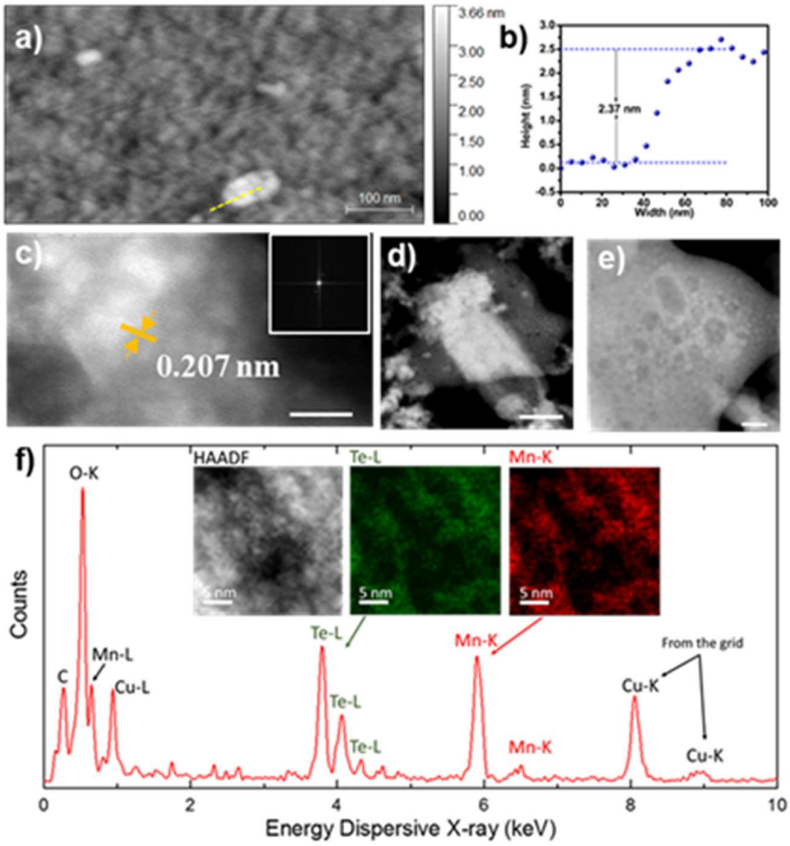

Figure. 5.5. Morphology and composition of 2D MnTe: ***(a)*** AFM image and, ***(b)*** corresponding height profile of an exfoliated MnTe sheet. ***(c)*** HAADF-STEM image of 2D MnTe (scale bar, 5nm) with its Fourier transform in the inset. ***(d)*** HAADF-STEM (scale bar, 100 nm) and ***(e)*** TEM image of a 2D MnTe sheet (scale bar, 20 nm). ***(f)*** EDS of the Mn–K, Mn–L, Te-L signals along with EDS-STEM elemental mapping for Mn (K) and Te (L) with scale bar, 10 nm in the inset. Cu signal is from the Cu TEM grid.

To verify the compositional details of MnTe sheets, STEM-EDS mapping analysis was carried out (***Figure. 5.5f***) and it confirms the purity of the material having the majority of Mn and Te elements. The homogeneous distribution of Mn and Te was also evident from the STEM-EDS mapping analysis (***Figure. 5.5f inset***). STEM-EELS mapping of Mn and Te is also

given in ***Figure. 5.6***. A thin organic coating (which has oxygen) produced during exfoliation and the TEM grid are likely to be the source of oxygen peaks in EDS and EELS data as oxygen was also observed in regions of the grid with no sample.

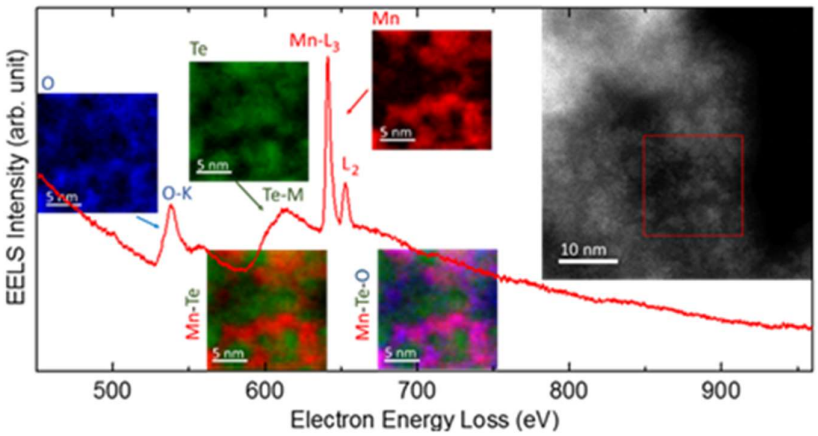

Figure 5.6. STEM-EELS map of Mn and Te

Raman spectra of the obtained 2D MnTe sheets are shown in ***Figure 5.7a***. Group theory predicts one E_{2g} Raman Active mode in MnTe around 178 cm^{-1}. In the Raman Spectra of exfoliated MnTe (***Figure 5.7a***), we could see two intense modes centred at 120.3 cm^{-1} and 140.4 cm^{-1}. These peaks correspond to A_1 and E_u bond stretching[28] of crystalline elementary Tellurium precipitates on the surface of MnTe sheets, formed by the decomposition on laser exposure as reported earlier.[29, 30] The predicted E_{2g} Raman Active mode corresponding to MnTe centred at around 178 cm^{-1} is also evident.

XPS analysis of the Mn2p and Te3d of exfoliated MnTe sheets are shown in ***Figure 5.7b&c*** respectively. The Mn2p doublets ($Mn2p_{3/2}$ and $Mn2p_{1/2}$) at 640.8 and 652.7 eV are from Mn-Te bonding, the doublets at 642.4 and

653.9 are contributed by MnO_2 residing on the surface.[31, 32] Te3d spectra, however, has predominant Te-Mn doublets (573 and 583.4 eV) and only traces of Te-O doublets (576 and 586.4 eV). Therefore, Raman spectra together with XPS results confirm the purity of MnTe phase.

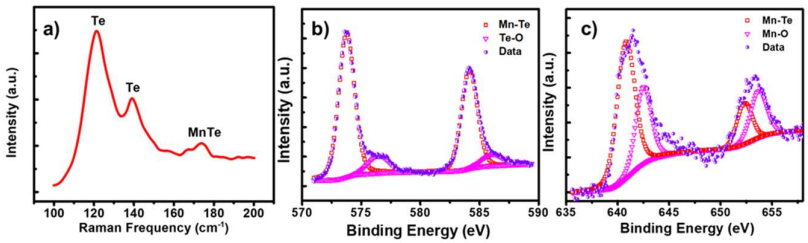

Figure. 5.7. Characterizations of 2D MnTe: (a) Raman spectrum of exfoliated MnTe sheets, ***(b) Te3d*** XPS spectrum, and (***c)*** Mn2p XPS spectrum of exfoliated MnTe sheets.

5.3.2 Magnetic properties

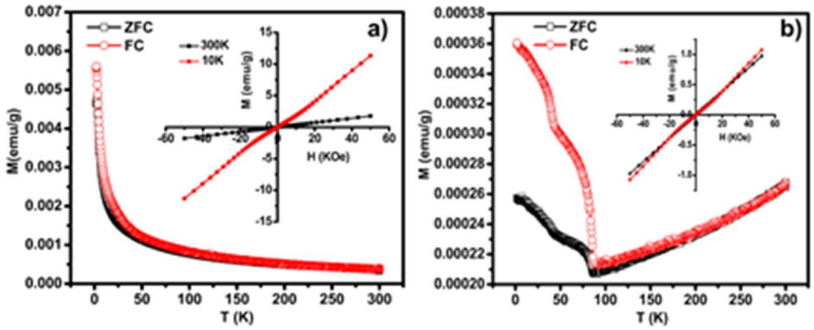

Figure. 5.8. Magnetism: (a) FC-ZFC M-T diagram (at 10 Oe) of exfoliated MnTe with M-H at 300K and 10K at the inset ***(b)*** FC-ZFC M-T diagram (at 10 Oe) of pristine MnTe with M-H at 300K and 10K at the inset.

From the magnetic measurements, it is very clear that the 2D MnTe is paramagnetic whereas pristine MnTe is antiferromagnetic. As the temperature is decreased below 300 K, magnetization (susceptibility) of 2D MnTe increases gradually (refer to ***Figure 5.8a***) which is typical of a

paramagnetic behaviour. Room temperature (300K) M-H loop (***Figure 5.8a*** inset) further confirms the paramagnetic behaviour having a linear M-H relationship. However, low temperature (10K) M-H loop with enhanced magnetization (nearly 10 times) and almost zero coercivity (Refer ***Figure 5.8a*** inset) indicates a weak magnetic ordering, a transition which could not be observed in FC-ZFC measurements. The observed paramagnetic behaviour could be due to the vanishing of the interplanar exchange interactions among the magnetic Mn ions in 2D MnTe sheets. These exchange interactions are responsible for the antiferromagnetic alignment of magnetic cations in pristine MnTe.

In the absence of strong exchange interactions, the only interactions that remain in MnTe sheets are dipolar in nature.[33] Due to the very weak nature of these dipolar interactions, the magnetic moments are oriented randomly even at low temperatures resulting in paramagnetic behaviour. A sharp enhancement in magnetization at very low temperatures (< 20 K) supplements the observation that the interactions are dipolar in nature. At very low temperatures, dipolar interactions outweigh thermal energy which facilitates ordering of moments resulting in increased magnetization. Pristine MnTe shows antiferromagnetic ground state with an observed anomalous behaviour below 87 K (see ***figure 5.8b***). This sharp hike in magnetization around 87K, both in FC and ZFC curves signifies a ferromagnetic ordering. Such an abrupt change of slope in FC-ZFC curve is believed to be due to strong inter-planar ferromagnetic interactions as a result of magnetoelastic coupling which dominates antiferromagnetic interactions.[34]

5.3.3 Optical absorption studies

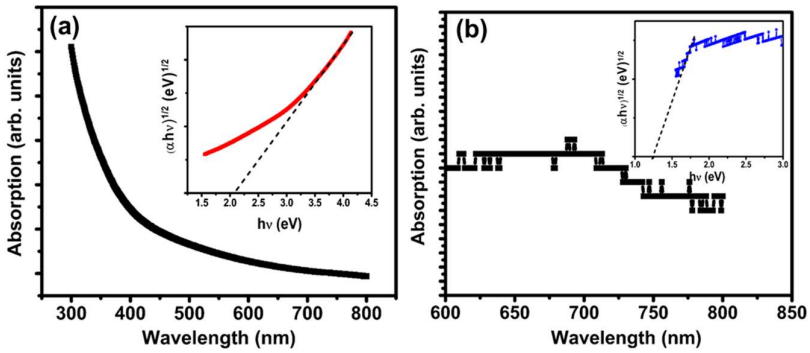

Figure. 5.9. Optical Bandgap: The optical bandgap measurements of ***(a)*** 2D MnTe and ***(b)*** Pristine MnTe with their corresponding Tauc plot in the inset.

Figure 5.9a shows the absorbance spectrum of the exfoliated 2D MnTe dispersed in DMF. The Tauc plot (Figure 5a inset) showed a fundamental band gap of ~ 2.1 eV. The band tails, however, extend further so as to have light absorption till about 1.8 eV (~700 nm). The bandgap of bulk MnTe is also determined and is found to be around 1.3 eV (***Figure 5.9b***). Such an enhancement in visible light absorption property of 2D MnTe could be exploited in photocatalytic applications.[35]

5.4 Conclusion

2D MnTe is successfully exfoliated from commercially available bulk precursors. The exfoliated sheets are found to be crystalline and pure with traces of $MnTe_2$. MnTe, being an antiferromagnetic material in its pristine form transforms to paramagnetic on exfoliation and could be due to the vanishing of strong exchange interactions at two dimensions and the magnetic order is characterized by weak dipolar interactions. Modified

optical band gap make 2D MnTe a suitable choice for photocatalytic applications.

5.5 References

1. H. Franzen and C. Sterner, *Journal of Solid State Chemistry*, 1978, **25**, 227-230.
2. C. F. Squire, *Physical Review*, 1939, **56**, 922-925.
3. J. Allen, G. Lucovsky and J. Mikkelsen, *Solid State Communications*, 1977, **24**, 367-370.
4. D. L. Decker and R. L. Wild, *Physical Review B*, 1971, **4**, 3425-3437.
5. T. Oguchi, K. Terakura and A. R. Williams, *Physical Review B*, 1983, **28**, 6443-6452.
6. U. Neitzel and K. Bärner, *physica status solidi (b)*, 1985, **129**, 707-715.
7. Y. Liu, J. Xing, H. Fu, Y. Li, L. Sun and Z. Lv, *Physics Letters A*, 2017, **381**, 2648-2657.
8. B. Aronsson, T. Lundström and S. Rundqvist, *Borides, silicides, and phosphides: a critical review of their preparation, properties and crystal chemistry*, Taylor & Francis, 1965.
9. S. J. Youn, B. I. Min and A. J. Freeman, *physica status solidi (b)*, 2004, **241**, 1411-1414.
10. K. K. Kelley, *Journal of the American Chemical Society*, 1939, **61**, 203-207.
11. T. Komatsubara, M. Murakami and E. Hirahara, *Journal of the Physical Society of Japan*, 1963, **18**, 356-364.
12. N. Kunitomi, Y. Hamaguchi and S. Anzai, *Journal de Physique*, 1964, **25**, 568-574.
13. J. Furdyna, *Journal of Applied Physics*, 1982, **53**, 7637-7643.
14. T. Dietl, H. Ohno, F. Matsukura, J. Cibert and D. Ferrand, *Science*, 2000, **287**, 1019-1022.
15. K. Ozawa, S. Anzai and Y. Hamaguchi, *Physics Letters*, 1966, **20**, 132-133.
16. D. Kriegner, K. Výborný, K. Olejník, H. Reichlová, V. Novák, X. Marti, J. Gazquez, V. Saidl, P. Němec and V. Volobuev, *Nature Communications*, 2016, **7**.
17. L. Hao, D. Meyers, H. Suwa, J. Yang, C. Frederick, T. R. Dasa, G. Fabbris, L. Horak, D. Kriegner, Y. Choi, J.-W. Kim, D. Haskel, P. J. Ryan, H. Xu, C. D. Batista, M. P. M. Dean and J. Liu, *Nature Physics*, 2018, **14**, 806-810.

18. K. S. Novoselov, A. K. Geim, S. V. Morozov, D. Jiang, Y. Zhang, S. V. Dubonos, I. V. Grigorieva and A. A. Firsov, *Science*, 2004, **306**, 666-669.
19. N. D. Mermin and H. Wagner, *Physical Review Letters*, 1966, **17**, 1133.
20. A. N. Andriotis and M. Menon, *Physical Review B*, 2014, **90**, 7.
21. R. R. Nair, M. Sepioni, I. L. Tsai, O. Lehtinen, J. Keinonen, A. V. Krasheninnikov, T. Thomson, A. K. Geim and I. V. Grigorieva, *Nat Phys*, 2012, **8**, 199-202.
22. Z. Zhang, X. Zou, V. H. Crespi and B. I. Yakobson, *ACS Nano*, 2013, **7**, 10475-10481.
23. B. Huang, G. Clark, E. Navarro-Moratalla, D. R. Klein, R. Cheng, K. L. Seyler, D. Zhong, E. Schmidgall, M. A. McGuire, D. H. Cobden, W. Yao, D. Xiao, P. Jarillo-Herrero and X. Xu, *Nature*, 2017, **546**, 270.
24. A. Puthirath Balan, S. Radhakrishnan, C. F. Woellner, S. K. Sinha, L. Deng, C. d. l. Reyes, B. M. Rao, M. Paulose, R. Neupane, A. Apte, V. Kochat, R. Vajtai, A. R. Harutyunyan, C.-W. Chu, G. Costin, D. S. Galvao, A. A. Martí, P. A. van Aken, O. K. Varghese, C. S. Tiwary, A. Malie Madom Ramaswamy Iyer and P. M. Ajayan, *Nature Nanotechnology*, 2018, **13**, 602-609.
25. A. Puthirath Balan, S. Radhakrishnan, R. Kumar, R. Neupane, S. K. Sinha, L. Deng, C. A. de los Reyes, A. Apte, B. M. Rao, M. Paulose, R. Vajtai, C. W. Chu, G. Costin, A. A. Martí, O. K. Varghese, A. K. Singh, C. S. Tiwary, M. R. Anantharaman and P. M. Ajayan, *Chemistry of Materials*, 2018, **30**, 5923-5931.
26. B. Kim, I. Kim, B.-k. Min, M. Oh, S. Park and H. Lee, *Electronic Materials Letters*, 2013, **9**, 477-480.
27. L. Yang, Z. H. Wang and Z. D. Zhang, *Journal of Applied Physics*, 2016, **119**, 045304.
28. B. H. Torrie, *Solid State Communications*, 1970, **8**, 1899-1901.
29. E. Janik, E. Dynowska, J. Bąk-Misiuk, M. Leszczyński, W. Szuszkiewicz, T. Wojtowicz, G. Karczewski, A. K. Zakrzewski and J. Kossut, *Thin Solid Films*, 1995, **267**, 74-78.
30. L.-J. Li, T.-W. Lin, J. Doig, I. B. Mortimer, J. G. Wiltshire, R. A. Taylor, J. Sloan, M. L. H. Green and R. J. Nicholas, *Physical Review B*, 2006, **74**, 245418.
31. R. Iwanowski, M. Heinonen and E. Janik, *Chemical physics letters*, 2004, **387**, 110-115.

32. R. Iwanowski, M. Heinonen and B. Witkowska, *Journal of Alloys and Compounds*, 2010, **491**, 13-17.
33. K. Tsiberkin, *The European Physical Journal B*, 2016, **89**, 54.
34. J. B. C. Efrem D'Sa, P. A. Bhobe, K. R. Priolkar, A. Das, S. K. Paranjpe, R. B. Prabhu and P. R. Sarode, *Journal of Magnetism and Magnetic Materials*, 2005, **285**, 267-271.
35. A. Puthirath Balan, S. Radhakrishnan, R. Neupane, S. Yazdi, L. Deng, C. A. de los Reyes, A. Apte, A. B. Puthirath, B. M. Rao, M. Paulose, R. Vajtai, C.-W. Chu, A. A. Martí, O. K. Varghese, C. S. Tiwary, M. R. Anantharaman and P. M. Ajayan, *ACS Applied Nano Materials*, 2018, **1**, 6427-6434.

Chapter 6

Generation of Magnetic Vortices on Curved Surfaces and Studies on the Bistability of Magnetic States

This chapter deals with the generation of magnetic vortices using FePd soft-magnetic alloys coated on curved surfaces of closely packed polystyrene hemispheres and investigation on the vortices dynamics.

IOP Nanotechnology *30(40): 405705-405711*

6.1 Introduction

Magnetic vortices are of great interest as they are potential candidates for improving the fundamental understanding of magnetism. They also present very promising applications, for example, in information and communication technology.[1-4] Magnetization reversal in magnetic structures is interesting both from a fundamental and technological perspective. When the size of the magnetic structure becomes comparable to a critical length scale such as exchange length, the multidomain spin configuration becomes energetically unfavourable, and either a single domain or an inhomogeneous magnetic configuration is formed. Magnetic vortices, a hurricane like magnetic entities, are formed in micron-sized, nanometer thick, soft ferromagnetic (FM) disks or rectangles. As the magnetic field is reduced from saturation, the magnetization tends to curl up in the in-plane direction along the edges of the disks to minimize the magnetostatic energy. This leads to a flux closure state with in-plane (IP) circular magnetization around the centre of the disc in a clockwise (C+) or counter-clockwise (C-) direction, referred to as the chirality or circularity. At the centre of the disc the magnetization points out-of-plane (OOP), either up (P+) or down (P-), with a Gaussian-like core to minimize the exchange energy between neighbouring spins, known as the polarity.[2, 5, 6]

A magnetic vortex structure is characterized by a sudden drop in the in-plane magnetization $\boldsymbol{M}$ around a particular field known as nucleation field, H_n. And as the applied in-plane field is increased, the core of this vortex moves perpendicular to the field direction until it is expelled from the disk at a particular field called annihilation field H_{an}.[7] The characteristics of

magnetization reversal via vortex state have been extensively investigated both experimentally and theoretically in two-dimensional structures like cylindrical nanodots, spherically curved surfaces, and artificial ferrimagnets.[8-14] Magnetic vortices were also exchange coupled to an antiferromagnet for improving their field stability.[15-17]

For soft magnetic microdisks, in an applied magnetic field, the magnetization reversal from a uniform state to a vortex state or vice versa involves an energy barrier ($\Delta\varepsilon$) giving rise to distinct nucleation and annihilation field resulting in hysteretic side lobes in the *M-H* loop.[18] It has been reported recently that a hysteresis-free switching from the single domain state to a vortex state and vice-versa is possible with the control of temperature.[19] In this case, the thermal energy will be sufficient to overcome the energy barrier for the reversal. Therefore, a bistable region with the hysteresis-free transition between collinear and vortex states is obtained if $\Delta\varepsilon \ll k_B T_e$. Here, $\Delta\varepsilon$ is the transition energy barrier (the energy barriers for transitions from vortex to collinear states and vice versa), T_e is the critical temperature above which magnetic bistability is possible, and a hysteresis-free transition between collinear and vortex states is obtained. When $\Delta\varepsilon$ is larger than $k_B T_e$, the bi-stability will give rise to hysteresis, characteristic for the vortex annihilation and nucleation. Below T_e, the transition between the vortex and the collinear states exhibit hysteresis, and the switching is irreversible.

Though the influence of temperature and inter-particle interaction on magnetization reversal of magnetic vortices has been extensively investigated,[19-21] only limited work has been carried out so far on addressing the tunability of T_e with composition. In this work, we have

employed self-assembled particle arrays as a template for FePd film deposition forming a two-dimensional magnetic vortex lattice on top of the particles. Pd rich FePd alloy has an *A1* disordered phase and hence soft-magnetic in nature and could be employed for creating magnetic vortices.[22] FePd composition has been systematically varied to have a deeper understanding on the composition dependence of the reversal behaviour, in particular on the transition from the vortex to the collinear state (and vice versa) as a function of temperature. Investigations show that T_e varies almost linearly with Fe concentration in the FePd alloy. Micromagnetic simulations of FePd nanocaps considering material parameters at corresponding T_e's show that there is an increase in energy barrier for the transition from uniform state to vortex state with increasing Fe content in FePd which shifts T_e to higher temperatures.

6.2 Experimental

Monolayers of polystyrene (PS) spheres were prepared on Si(001) substrates using nanosphere lithography. Aqueous suspensions with monodisperse non-functionalized PS particles having an average diameter of (480±10) nm were purchased from MicroParticles GmbH Berlin. The suspension was applied to the surface of the water, where 2D crystallization was carried out leading to highly ordered hexagonal close-packed monolayer of the particles. Then, the monolayer was deposited on the Si substrate by slow water evaporation. Further details concerning the preparation of particle monolayers are described elsewhere.[23, 24] FePd magnetic cap structures were realized by depositing thin films of composition Ta(5 nm)/ Fe_xPd_{100-x} (20 nm)/ Ta(5 nm) onto dense arrays of self-assembled PS particles by co-sputter deposition of iron (Fe; 99.99%)

and palladium (Pd; 99.95%) targets using a Bestec Gmbh 8 target dc magnetron sputtering system. Different sets of films were prepared by varying the Fe_xPd_{100-x} composition (x=13, 15, 17, and 20). The Ar-pressure was kept constant at 5×10^{-3} mbar, while the base pressure of the deposition chamber was below 5 x 10^{-8}mbar. During film deposition, the thickness was monitored using a calibrated quartz microbalance. For reference, films were also deposited on thermally oxidized planar silicon substrates. During deposition, the sample stage was rotated at a constant rate for uniformity in film thickness, and the substrate was kept at room temperature. An added advantage of this self-assembly technique is that large area arrays (typically 10 mm × 10 mm) can be easily realized which is crucial as far as integral magnetic characterization is concerned. *M-H* hysteresis loops and the variation of *M* with temperature (*M-T* curve) were recorded in the temperature range from 5 up to 450 K by using a superconducting quantum interference device – vibrating sample magnetometer (SQUID-VSM). In addition, in order to investigate irreversible magnetization reversal processes, first-order reversal curve (FORC) measurements using a magneto-optical Kerr effect (MOKE) setup were carried out. All magnetic measurements were obtained by applying a magnetic field along the plane of the film and provide ensemble-averaged results.

6.3 Results and Discussions

Figure 6.1a shows a scanning electron microscope (SEM) plan-view image of a sample. ***Figure 6.1b*** depicts a transmission electron microscope cross-sectional image, showing the formation of a magnetic cap structure after film deposition. In the image, the PS particles do not

appear spherical, which is due to a melting process induced by ion bombardment needed during the TEM sample preparation; nevertheless, the magnetic cap structures remained stable during the TEM study.

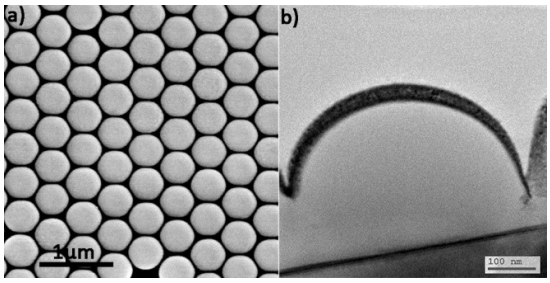

Figure. 6.1. ***a)*** SEM Planar view of self-assembled SiO_2 spheres with FePd deposited on the top ***b)*** cross-sectional TEM showing FePd cap formation on the surface of the spheres.

6.3.1 Magnetic measurements

Figure 6.2a shows *M-T* curves of planar Fe-Pd reference samples with various compositions, revealing clearly the magnetic order transition temperature (Curie temperature, T_C), which increases almost linearly with Fe content, as presented in ***Figure 6.2b***. Furthermore, the magnetization is larger for samples with higher Fe content and shows a pronounced temperature dependence towards the Curie temperature, as expected.[25]

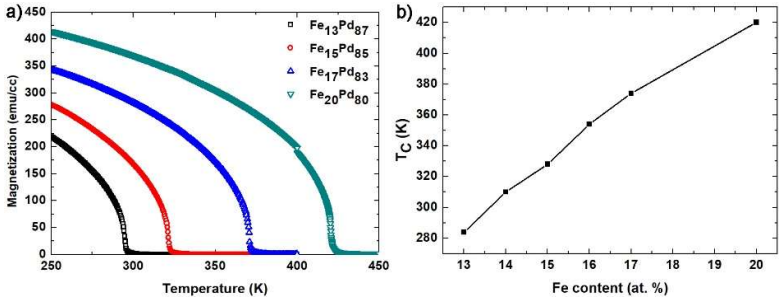

Figure. 6.2. ***a)*** M-T curve for Fe_xPd_{100-x} films deposited on thermally oxidized planar silicon substrates for various compositions. ***b)*** variation of Curie temperature with respect to Fe content.

In the same deposition run, these films were also deposited on particle templates. ***Figure 6.3a*** shows exemplarily the *M-H* hysteresis loops recorded for the $Fe_{20}Pd_{80}$cap array at different temperatures. At low temperatures for instance at 10 K, the reversal behaviour is characteristic for an in-plane easy axis loop of a soft magnetic material showing a coercive field of about 25 Oe. Furthermore, almost a full remanent magnetization is obtained at zero field indicating that the magnetic caps remain in a uniform single domain magnetic state. This uniform state was also verified from FORC measurements performed at 13 K (***Figure 6.3c***). For tracing out a FORC, after saturation, the magnetization M is measured starting from a reversal field H_R back to positive saturation. A family of FORC's is recorded at different H_R values with equal spacing. The FORC density ρ is defined as a mixed second order derivative $\rho\,(H_R, H) \equiv -\frac{1}{2}\frac{\partial^2 M(H_R,H)}{\partial H_R \partial H}$, which eliminates purely reversible components of the magnetization reversal.[26, 27]

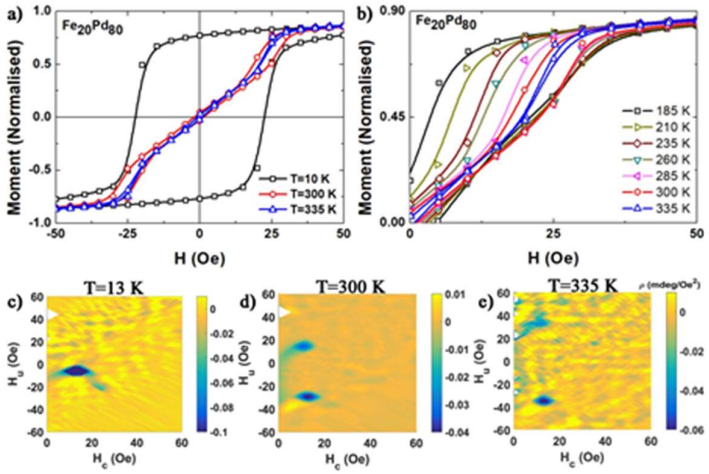

Figure. 6.3. ***a-b)*** *M-H* curves of the $Fe_{20}Pd_{80}$ cap array recorded at various temperatures. Lines are guides to the eye. ***c-e)*** FORC diagrams recorded at ***c)*** 13 K, ***d)*** 300 K, and ***e)*** 335 K.

Therefore, any non-zero ρ corresponds to irreversible switching processes. The presented FORC diagrams in figure 3c),d) are contour plots of ρ along the coercive (H_C) and interaction (H_u) field axis given by $H_u = (H + H_R)/2$ and $H_C = (H - H_R)/2$. For non-interacting single domain particles, the response on FORC diagram occurs at H_u= 0 and H_C=H_{sw} where H_{sw} is the intrinsic switching field. On the other hand, for interacting single domain systems, the response on the FORC diagram occurs at H_u=$-H_{int}$ and H_C=H_{sw}. Here H_{int} represents the strength of the interaction field. Looking at the FORC diagram taken at 13 K, a prominent feature located at H_C=17 Oe and H_u= -8 Oe is visible (***Figure 6.3c***). This feature indicates the presence of irreversible switching processes, which are typically observed for magnetically interacting single domain particles with narrow switching field distribution.[28] At this low temperature, a non-negligible magneto-crystalline anisotropy of Fe-Pd may prevent the nucleation of non-uniform states. However, as the temperature rises, the magneto-crystalline anisotropy decreases and thermal activation can induce nucleation events resulting in a non-uniform vortex state. For example, at 300 K, as the applied field is reduced from saturation to about 25 Oe, the nucleation field H_n is reached (see ***Figure 6.3a***). At this point, the formation of a magnetic vortex configuration is initiated till zero field. Increasing the field from zero will push the magnetic vortex core away from the center of the caps until it becomes annihilated at H_{an} and a collinear magnetic state is formed. Furthermore, it can be seen from the *M-H* loop that there is a steady decrease in magnetization below the nucleation field which means that a stable vortex state develops from the saturated state.[29] This behavior was also investigated by FORC

measurements performed at 300 K (***Figure 6.3d***). Since vortex nucleation and annihilation are irreversible processes, the FORC diagram consists of two prominent signatures, one in the upper and the other in the lowerhalf plane, which is due to nucleation and annihilation of vortex states.[8, 30] In a given cap structure, there are actually two paths for vortex annihilation; a vortex can exit the cap structure from the same side which it has been nucleated or from the opposite side. If the structure is irregular, these two paths will have two different annihilation fields and can give rise to a butterfly like feature along the central horizontal axis in the FORC diagram.[26]

However, in the present case, such a feature is absent in the FORC diagram indicating uniformity in the annihilation field over the cap array. The bifurcation temperature T_e for other concentrations of Fe (x=13, 15 and 17) was also determined in a similar fashion and are given in ***Figure 6.4.***

Typically, the hysteresis characterized by annihilation and nucleation field signifies an energy barrier for the transition between the vortex and collinear states. At high magnetic fields, the collinear state will be the energetically favourable state. On the other hand, the vortex state will be energetically favourable at zero field. At an intermediate field, both states will become energetically equal (bistability) but separated by an energy barrier. At elevated temperatures, the thermal energy will be sufficient to overcome this energy barrier, resulting in hysteresis-free switching between the two magnetic states.[19] This is in fact observed for $Fe_{20}Pd_{80}$ at 335 K, as revealed in the *M-H* loop of ***Figure 6.3a***.

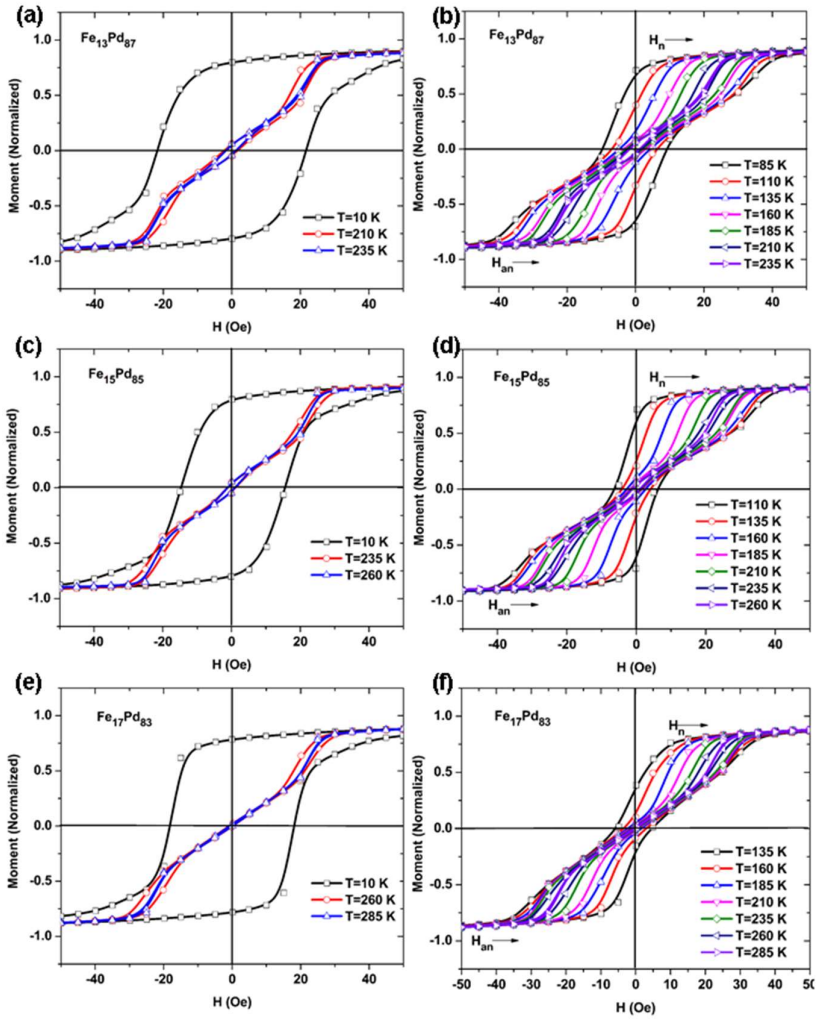

Figure. 6.4. (a) M-H curve for $Fe_{13}Pd_{87}$ nanocap arrays recorded at T=10 K, 210 K, 235 K ***(b)*** M-H curve for $Fe_{13}Pd_{87}$ nanocap arrays recorded at different temperatures ranging from T=85 K to 235 K ***(c)*** M-H curve for $Fe_{15}Pd_{85}$ nanocap arrays recorded at T=10 K, 235 K, 260 K ***(d)*** M-H curve for $Fe_{15}Pd_{85}$ nanocap arrays recorded at different temperatures ranging from T=110 K to 260 K ***(e)*** M-H curve for $Fe_{17}Pd_{83}$ nanocap arrays recorded at T=10 K, 260 K, 285 K (***f)*** M-H curve for $Fe_{17}Pd_{83}$

The onset temperature at which this hysteresis-free switching occurs is called bifurcation temperature (T_e). This temperature can be easily

extracted from the temperature dependent nucleation and annihilation fields at the temperature where they become equal, as shown in ***Figure 6.5a***. The nucleation field was measured by SQUID-VSM at the descending branch of the *M-H* loop and it represents the field at which the transition to a vortex state occurs. In this example, the nucleation field increases with increasing temperature, while the annihilation field remains almost unchanged. Both values become equal at about 335 K, the bifurcation temperature of this system. Please note that an increase in the nucleation field with increasing temperature is consistent with thermally activated vortex nucleation over an energy barrier.[19, 31, 32]

The dependence of the bifurcation temperature on the Fe-Pd composition is summarised in ***Figure 6.5b***, revealing an almost linear increase with Fe content.

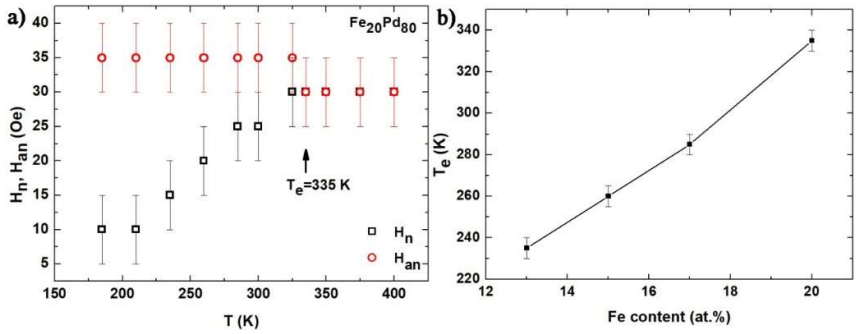

Figure 6.5. (a) Temperature dependence of the nucleation and annihilation field for $Fe_{20}Pd_{80}$ caps, ***(b)*** Bifurcation temperature T_e as a function of Fe-Pd composition.

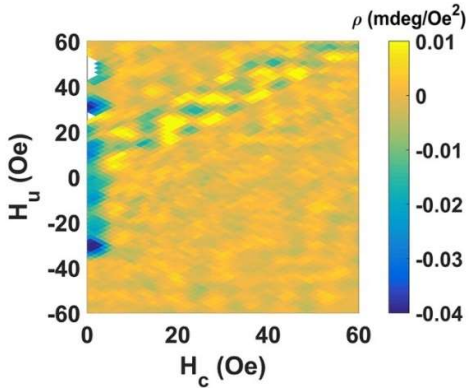

Figure 6.6. FORC diagram for sample $Fe_{17}Pd_{83}$ recorded at 335 K

Moreover, FORC measurements were carried out for the $Fe_{20}Pd_{80}$ sample at 335 K, the onset temperature of bifurcation. Please note that this is the maximal temperature that could be achieved in the MOKE setup employed. The FORC diagram presented in ***Figure 6.3e*** still reveals two distinct features at around 10 Oe, indicating a somewhat higher bifurcation temperature than observed for SQUID-VSM. We believe that the different time scale of measurement, seconds vs. minutes, is responsible for this discrepancy, as T_e can be also considered as the temperature at which the single domain-vortex state transition time equals the measurement time. Therefore, we performed a further FORC measurement at 335 K on sample $Fe_{17}Pd_{83}$, which exhibits a lower temperature of bifurcation of about 285 K. In this case, we observed an almost hysteresis-free transition (less than 2 Oe, see ***Figure 6.6***). It might be still discussable if a small amount of energy cost to rearrange the spin texture from uniform to vortex-like curling structure is present.

6.3.2 Micromagnetic simulation

As T_e can be associated with the present energy barrier, it can be concluded that this energy barrier increases linearly with Fe content as well. In order to get a better understanding of the underlying mechanism, the energy barrier ($\Delta\varepsilon$) for switching from a collinear to a vortex state at

the bifurcation temperature was calculated for three samples (Fe_xPd_{100-x} with x=13, 17, and 20) using the hybrid finite element micromagnetic simulation program (NMAG, University of Southampton), which is based on the Landau-Lifshitz-Gilbert (LLG) equation.[33] The following material parameters were used: saturation magnetization, M_s=2x10^{5}A/m, exchange stiffness constant, A=0.84x10^{-12} J/m for $Fe_{13}Pd_{87}$, M_s=3.04x10^{5}A/m, A=1.63x10^{-12} J/m for $Fe_{17}Pd_{83}$, and M_s=3.25x10^{5}A/m, A=1.86x10^{-12} J/m for $Fe_{20}Pd_{80}$. M_s values at different temperatures were derived from SQUID-VSM measurements. Negligible magneto-crystalline anisotropy was assumed in all cases. We chose a damping constant of 0.5. The magnetic structure is formed by tetrahedral elements for mesh generation. The mesh size of the element is chosen to be 5 nm by taking into account the exchange length of the Fe-Pd alloys. Simulations were carried out for hemishells of outer radius 240 nm and a thickness of 20 nm. From the simulations, the energy barrier $\Delta\varepsilon$ was extracted. As expected, with increasing Fe content from 13, 17, and 20 at.% increasing values for the energy barrier were obtained from 4.88x10^{-21} J, 1.04x10^{-20} J to 1.16x10^{-20}J, respectively, which agrees at least qualitatively with our experimental observations.

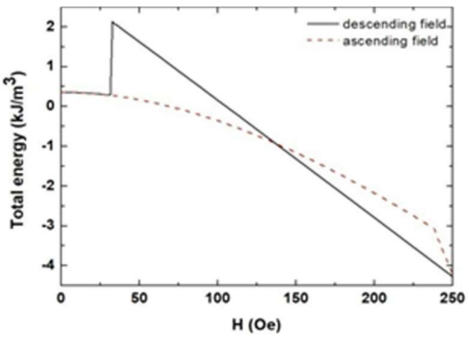

Figure 6.7. Simulated field dependence of the total magnetic energy for a $Fe_{20}Pd_{80}$ hemishell with a diameter of 480 nm and a thickness of 20 nm.

In the event of negligible magneto-crystalline anisotropy, the field dependence of the total energy of FePd magnetic caps is mainly

determined by the competition between Zeeman and magnetostatic energy. The field variation of the Zeeman energy mainly determines the field dependence of the total energy of the collinear state.[34] As we decrease the field from positive saturation (i.e., from the collinear state) to the vortex nucleation field, the Zeeman energy increases, causing a linear increase in the total energy of the collinear state as shown in ***Figure 6.7***. On the other hand, starting from the vortex state at zero field and increasing the field to positive saturation, the field dependence of the total energy is now mainly given by two competing contributions, magnetostatic and Zeeman energy.[35] The Zeeman energy will decrease with increasing external field while the magnetostatic energy will increase due to the emerging stray field present at the circumference of the caps as the vortex core is pushed more and more out of the centre. Due to this competition, the total energy of the vortex state now gradually decreases from its value at zero field as the field is increased towards positive saturation. Please note that, as the simulations were carried out at zero temperature, the vortex nucleation and annihilation events (at around 30 and 250 Oe, respectively) are distinct in ***Figure 6.7***. At an intermediate field, the energies of both vortex and collinear state become equal but are separated by an energy barrier $\Delta\varepsilon$ whose absolute value is determined by the sum of the magnetostatic energy, exchange energy, and Zeeman energy. When $\Delta\varepsilon$ is larger than $k_B T_e$, the bistability will give rise to hysteresis, characteristic for the vortex annihilation and nucleation. However, when $\Delta\varepsilon$ is smaller than $k_B T_e$, the switching will occur without hysteresis. Therefore, a bistable region with the hysteresis-free transition

between collinear and vortex states is obtained in the temperature range $T_c > T > T_e$.

6.4 Conclusion

Magnetic vortex structures were created on FePd films deposited onto self-assembled particles arrays. We demonstrated that in FePd cap structures the energy barrier associated with the transition between vortex and collinear state (or vice versa) can be tuned by varying the Fe content in the alloy. At elevated temperatures, the thermal energy will be sufficient to overcome this energy barrier, resulting in a hysteresis-free switching between the two magnetic states. It was found that the bifurcation temperature, where a hysteresis-free switching occurs, increases with Fe content, thereby allowing the control of bistability of magnetic states even at room temperature.

6.5 References

1. M. S. Wolf, R. Badea and J. Berezovsky, *Nature Communications*, 2016, **7**, 11584.
2. J. F. Pulecio, P. Warnicke, S. D. Pollard, D. A. Arena and Y. Zhu, *Nature Communications*, 2014, **5**, 3760.
3. S. Bohlens, B. Krüger, A. Drews, M. Bolte, G. Meier and D. Pfannkuche, *Applied Physics Letters*, 2008, **93**, 142508.
4. S. Wintz, V. Tiberkevich, M. Weigand, J. Raabe, J. Lindner, A. Erbe, A. Slavin and J. Fassbender, *Nature Nanotechnology*, 2016, **11**, 948.
5. R. P. Cowburn, D. K. Koltsov, A. O. Adeyeye, M. E. Welland and D. M. Tricker, *Physical Review Letters*, 1999, **83**, 1042-1045.
6. T. Shinjo, T. Okuno, R. Hassdorf, K. Shigeto and T. Ono, *Science*, 2000, **289**, 930-932.
7. V. Novosad, K. Y. Guslienko, H. Shima, Y. Otani, K. Fukamichi, N. Kikuchi, O. Kitakami and Y. Shimada, *IEEE Transactions on Magnetics*, 2001, **37**, 2088-2090.
8. R. K. Dumas, K. Liu, C.-P. Li, I. V. Roshchin and I. K. Schuller, *Applied Physics Letters*, 2007, **91**, 202501.
9. P. N. Lapa, J. Ding, C. Phatak, J. E. Pearson, J. S. Jiang, A. Hoffmann and V. Novosad, *Journal of Applied Physics*, 2017, **122**, 083903.
10. R. Streubel, D. Makarov, F. Kronast, V. Kravchuk, M. Albrecht and O. G. Schmidt, *Physical Review B*, 2012, **85**, 174429.
11. R. Streubel, V. P. Kravchuk, D. D. Sheka, D. Makarov, F. Kronast, O. G. Schmidt and Y. Gaididei, *Applied Physics Letters*, 2012, **101**, 132419.
12. R. Brandt, R. Rückriem, D. A. Gilbert, F. Ganss, T. Senn, K. Liu, M. Albrecht and H. Schmidt, *Journal of Applied Physics*, 2013, **113**, 203910.
13. D. Mitin, D. Nissen, P. Schädlich, S. S. P. K. Arekapudi and M. Albrecht, *Journal of Applied Physics*, 2014, **115**, 063906.
14. D. Nissen, D. Mitin, O. Klein, S. S. P. K. Arekapudi, S. Thomas, M. Y. Im, P. Fischer and M. Albrecht, *Nanotechnology*, 2015, **26**, 465706.
15. D. Nissen, O. Klein, P. Matthes and M. Albrecht, *Physical Review B*, 2016, **94**, 134422.

16. J. Sort, A. Hoffmann, S. H. Chung, K. S. Buchanan, M. Grimsditch, M. D. Baró, B. Dieny and J. Nogués, *Physical Review Letters*, 2005, **95**, 067201.
17. S. Thomas, D. Nissen and M. Albrecht, *Applied Physics Letters*, 2014, **105**, 022405.
18. H. F. Ding, A. K. Schmid, D. Li, K. Y. Guslienko and S. D. Bader, *Physical Review Letters*, 2005, **94**, 157202.
19. Ö. Erik, B. A. Unnar, M. Emil, K. Vassilios, K. P. Gunnar, Y. S. Alexander, A. V. Marc, K. Florian, P. Evangelos Th, S. F. Charles and H. Björgvin, *New Journal of Physics*, 2014, **16**, 053002.
20. K. Y. Guslienko, V. Novosad, Y. Otani, H. Shima and K. Fukamichi, *Physical Review B*, 2001, **65**, 024414.
21. V. Novosad, K. Y. Guslienko, H. Shima, Y. Otani, S. G. Kim, K. Fukamichi, N. Kikuchi, O. Kitakami and Y. Shimada, *Physical Review B*, 2002, **65**, 060402.
22. T. Liu, L. Ma, S. Q. Zhao, D. D. Ma, L. Li, G. Cheng and G. H. Rao, *Journal of Materials Science: Materials in Electronics*, 2017, **28**, 3616-3620.
23. M. Krupinski, D. Mitin, A. Zarzycki, A. Szkudlarek, M. Giersig, M. Albrecht and M. Marszałek, *Nanotechnology*, 2017, **28**, 085302.
24. M. Krupinski, M. Perzanowski, A. Maximenko, Y. Zabila and M. Marszałek, *Nanotechnology*, 2017, **28**, 194003.
25. *The Philosophical Magazine: A Journal of Theoretical Experimental and Applied Physics*, 1960, **5**, 335-342.
26. C. Pike and A. Fernandez, *Journal of Applied Physics*, 1999, **85**, 6668-6676.
27. S. Muralidhar, J. Gräfe, Y.-C. Chen, M. Etter, G. Gregori, S. Ener, S. Sawatzki, K. Hono, O. Gutfleisch, H. Kronmüller, G. Schütz and E. J. Goering, *Physical Review B*, 2017, **95**, 024413.
28. A. P. Roberts, D. Heslop, X. Zhao and C. R. Pike, *Reviews of Geophysics*, 2014, **52**, 557-602.
29. G. N. Kakazei, M. Ilyn, O. Chubykalo-Fesenko, J. Gonzalez, A. A. Serga, A. V. Chumak, P. A. Beck, B. Laegel, B. Hillebrands and K. Y. Guslienko, *Applied Physics Letters*, 2011, **99**, 052512.
30. R. K. Dumas, C.-P. Li, I. V. Roshchin, I. K. Schuller and K. Liu, *Physical Review B*, 2007, **75**, 134405.

31. R. Dittrich, T. Schrefl, M. Kirschner, D. Suess, G. Hrkac, F. Dorfbauer, O. Ertl and J. Fidler, *IEEE Transactions on Magnetics*, 2005, **41**, 3592-3594.
32. G. Mihajlović, M. S. Patrick, J. E. Pearson, V. Novosad, S. D. Bader, M. Field, G. J. Sullivan and A. Hoffmann, *Applied Physics Letters*, 2010, **96**, 112501.
33. T. Fischbacher, M. Franchin, G. Bordignon and H. Fangohr, *IEEE Transactions on Magnetics*, 2007, **43**, 2896-2898.
34. R. Moreno, R. F. L. Evans, S. Khmelevskyi, M. C. Muñoz, R. W. Chantrell and O. Chubykalo-Fesenko, *Physical Review B*, 2016, **94**, 104433.
35. W. Scholz, K. Y. Guslienko, V. Novosad, D. Suess, T. Schrefl, R. W. Chantrell and J. Fidler, *Journal of Magnetism and Magnetic Materials*, 2003, **266**, 155-163.

Chapter 7

Fabrication of an in-house fully automated Magneto-Optic Kerr Effect (MOKE) Magnetometer

This chapter deals with the fabrication of a fully automated indigenous magneto-optic Kerr effect (MOKE) set up from scratch including its standardization. Initial results on a few thin film samples are also provided in this chapter as a demonstrator to prove the validity of the measurements using the fabricated set-up.

Chapter 7

7.1 Introduction

Magneto-Optic Kerr effect is the rotation of plane polarized light when an incident plane polarized light is shone on a magnetized specimen.[1] A tabletop magnetic hysteresis plotting set up can be fabricated by using the principle of magneto-optic Kerr effect (MOKE).[2] Conventional magnetometers like vibrating sample magnetometer (VSM), superconducting quantum interface device (SQUID) magnetometer measure the bulk magnetic properties, and in a MOKE magnetometer, simply 'MOKE', one probes the surface magnetism since the laser probe can penetrate into a sample up to a depth of 20 nm. A MOKE can thus be employed for studying the surface magnetism of thin films, isolated multilayers or monolayers of a two-dimensional (2D) material which reflects the incident laser beam. A fully automated MOKE has several advantages over a conventional VSM or a SQUID magnetometer. Since the probe is a laser beam, one could measure the magnetization of a local area of a thin film/2D material by controlling the spot size.

Determination of the surface anisotropy and magnetization are very important for some applications such as magnetic storage and other sensing applications which makes MOKE a versatile technique. MOKE could be modified for acquiring images of the magnetic domains formed on a sample surface by employing a CCD camera. In this chapter, fabrication, automation and calibration of a MOKE is explained. Some initial results obtained using the in-house fabricated MOKE are also presented.

7.2 Principle

The microscopic origin of the Kerr effect is due to the spin-orbit interaction (Zeeman Effect) and relativistic effects.[3]

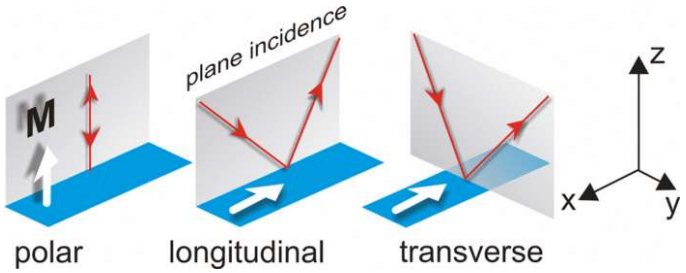

Figure. 7.1. Different geometries/modes of MOKE.

Depending upon the direction of magnetization M with respect to reflecting surface and plane of incidence, there are three types of MOKE geometries. They are polar, longitudinal and transverse ***(Figure 7.1***). In general, the Kerr Effect is the superposition of all the three modes, however, the effects are much more intense when occurred in a particular geometry.

Macroscopically, magneto-optic effects arise from the antisymmetric, off-diagonal elements in the dielectric tensor (equation 7.1).[2, 4]

$$\bar{\varepsilon} = \varepsilon \begin{pmatrix} 1 & iQ_Z & -iQ_y \\ -iQ_z & 1 & iQ_x \\ iQ_y & iQ_x & 1 \end{pmatrix} \qquad (7.1)$$

Where Q_x, Q_y *and* Q_z are the components of Voight vector, **Q** and ε is the isotropic part of the dielectric constant. The components of Voight vectors are proportional to the magnetization (**M**) of the material and are responsible for the magneto-optic effects.

Before going to the experimental part, it is necessary to briefly explain the working principle.

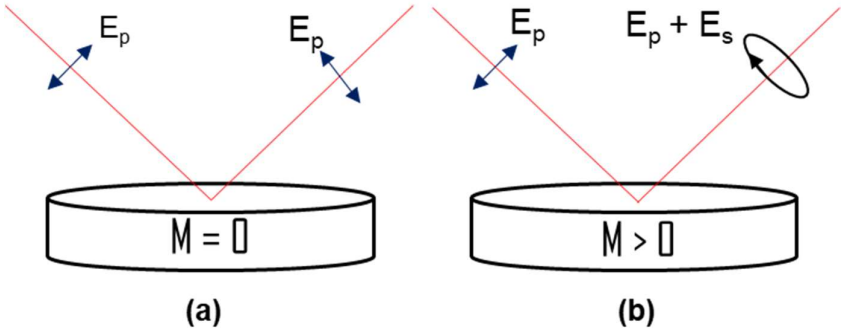

Figure. 7.2. Reflection of plane polarized light on a magnetic specimen when ***(a)*** M =0 and ***(b)*** M>0.

Consider a plane polarized (p-polarized) light incident on a reflecting sample surface as shown in ***Figure 7.2***. When the sample is nonmagnetic (M=0), the reflected beam is purely p-polarized (***Figure 7.2a***). If the sample is magnetized (***M***>0), the reflected beam is elliptically polarized (***Figure 7.2b***) and having an s component (*Es*) in addition to the predominant p component (*Ep*) and the Kerr rotation is given by '*Es/Ep'*. A linear polarizer is placed before the detector at a crossed position with a view to measuring the *s* component of the reflected beam by eliminating the predominant p component. The position of the linear polarizer is usually kept at a slight offset angle (δ) from the crossed position and the intensity at the detector is given by equation 7.2,

$$I = \left|E_p \sin\delta + E_s \cos\delta\right|^2 \approx \left|E_p\delta + E_s\right|^2 \qquad (7.2)$$

Kerr rotation φ' and Kerr ellipticity φ'' are given by the formula (equation 7.3),

$$\frac{E_s}{E_p} = \varphi' + i\varphi'' \qquad (7.3)$$

Intensity (***I***) could be written in terms of Kerr rotation (φ') and ellipticity (φ'') by equation 7.4,

$$I = \left|E_p\right|^2 |\delta + \varphi' + i\varphi''|^2$$

$$\approx \left|E_p\right|^2 (\delta^2 + 2\delta\varphi') = I_0\left(1 + \frac{2\varphi'}{\delta}\right) \qquad (7.4)$$

with I_0 being the intensity at zero Kerr rotation (equation 7.5),

$$I_0 = \left|E_p\right|^2 \delta^2 \qquad (7.5)$$

Since both Kerr rotation φ' and Kerr ellipticity φ'' are linearly proportional to the magnetization ***M***, the measured intensity versus the applied field ***H*** gives the hysteresis of the specimen under investigation.

7.3 Experimental Set Up

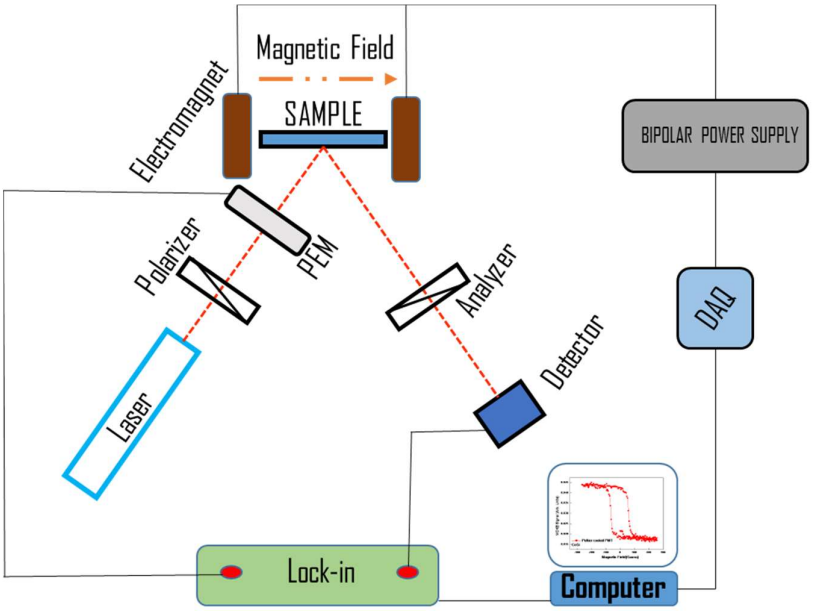

Figure. 7.3. Block Diagram of MOKE set up in the longitudinal configuration

A block diagram of the setup implemented for the measurement of the MOKE signal at the Magnetics Laboratory, CUSAT is depicted in ***Figure 7.3***. Longitudinal mode of MOKE is used for measuring the in-plane magnetization (***M***) of the sample. The polarizer is placed between a laser light source and the target sample and the analyzer is placed between the sample and the photodiode with its axis of polarization orthogonal to the polarizer impeding light from reaching the photodiode. When sample is not magnetized (***M***=0), no light is transmitted through the analyzer at crossed position and the signal reaching the photodiode is minimum (zero ideally). When the sample is magnetized by applying a suitable magnetic field in between the magnetic poles of the electromagnets, light reflected

from the sample experiences a rotation in its plane of polarization. This rotation allows more light to pass through the analyzer, striking the photodiode and producing an output signal (Kerr signal). A more intense signal from the photodiode denotes an increase in the rotation of the polarization and therefore a more magnetized sample. By observing the magnetic behaviour of a sample in this way, it is possible to get an insight into several important magnetic properties including remanence, coercive field, and saturation field of a ferromagnetic material.

This set up is also integrated with a closed cycle liquid helium cryostat (Cryo Industries Inc.) to perform low-temperature measurements (10 K to 300 K). A Lakeshore temperature controller precisely steers the temperature of the sample. The experimental set up is automated using programmable National Instruments (NI) LabVIEW graphical user interface (GUI) software with the help of a NI compact data acquisition system (c-DAQ) for interfacing. A large set of data points can be acquired in a short span of time.

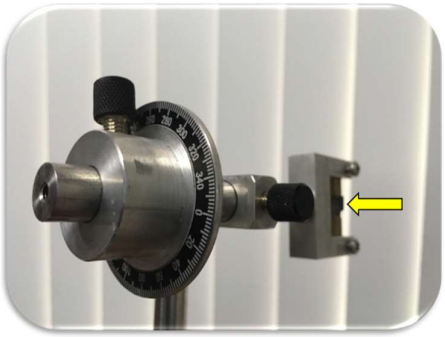

Figure. 7.4. Sample stage (indicated by yellow arrow) with provision to rotate through 360 degrees.

All the components are mounted on a locally fabricated vibration-free optical breadboard which minimizes unwanted variations in Kerr signal due to external vibrations. The sample mount is designed so as to keep the film sample in longitudinal configuration and provided with a facility to rotate the sample manually through 360 degrees and the

compatible sample dimension is ~ 1 cm^2 (***Figure 7.4)***. ***Figure 7.5*** shows a digital photograph of the MOKE set up.

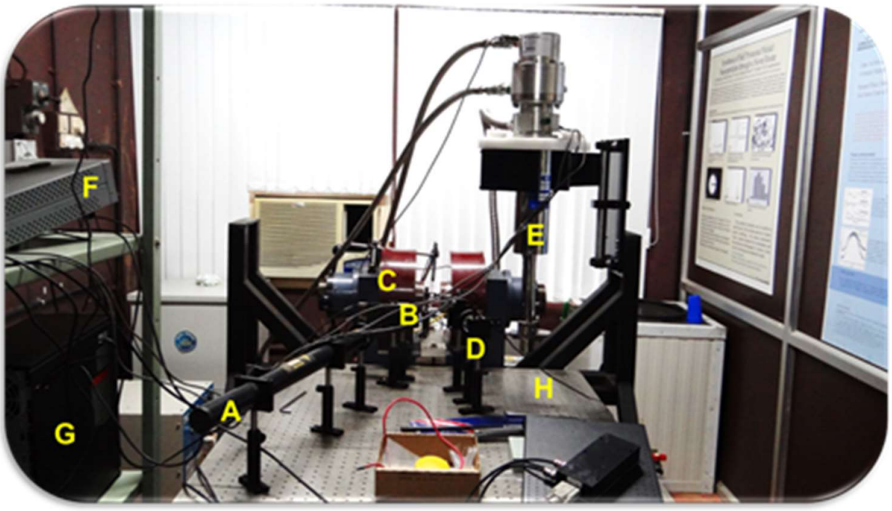

Figure. 7.5. Photograph of the MOKE set up fabricated. The components marked are **A.** He-Ne laser **B.** Photoelastic Modulator **C.** Electromagnet **D.** Photodetector **E.** Liquid Helium Closed Cycle Cryostat **F.** Lock-in amplifier **G.** Computer **H.** Vibration free table.

7.4 Instrumentation and Methods

As mentioned earlier, the MOKE setup mounted on a vibration-free optical breadboard. Sheet polarizers are used in conjunction with a red 20 mW HeNe laser (Melles Griot) to get a polarized light beam. An adjustable air-gap electromagnet capable of achieving a maximum field of 1T is employed to magnetize thin film samples (with 5 cm pole gap, it can achieve up to 3500 mT). Before striking the sample, the laser beam passes through a photoelastic modulator (PEM, Hinds Instruments) which modulates the input signal in its characteristic frequency (50 kHz) making use of Faraday Effect. The lock-in amplifier (Advancetech 7265) is used to lock the signal at the characteristic frequency of the PEM with a view

to having a noise-free detection of the signal striking the photodiode (Hinds Instruments) after reflection at the sample surface. The electromagnet is powered using a KEPCO BOP-36-12DL model bipolar power supply. The current fed is controlled synchronously via a National Instruments data acquisition system (NI cDAQ)[5] module equipped with both digital to analogue (NI9263) and an analogue to digital conversion (NI9215) modules (***Figure 7.6***)

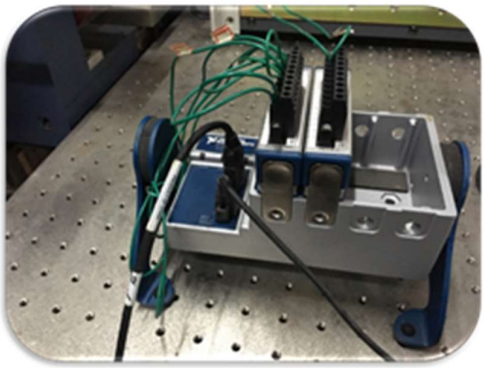

Figure. 7.6. NI c-DAQ provided with NI9215 & NI9263

Before recording the MOKE the electromagnet is calibrated by noting the strength of the current and the corresponding magnetic field measured using a Gauss meter. A graph depicting the current versus magnetic field strength is plotted. A linear regression is used to correlate the current reading of the power supply and magnetic field strength of the electromagnet (***Figure 7.7***).

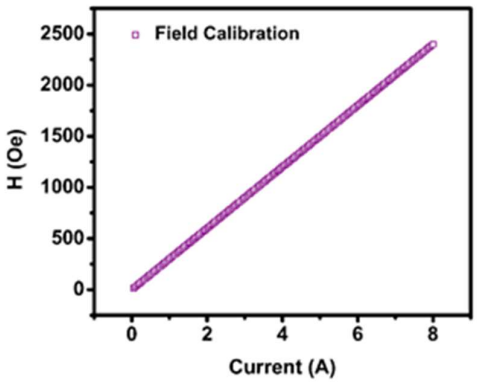

Figure 7.7. Current-Magnetic Field Calibration plot showing a perfectly linear behaviour.

A corresponding conversion factor is then incorporated into the computer programme in order to have accurate control over the field strength since the electromagnet is being controlled through NI c-DAQ. Thin film magnetic samples were mounted on an adjustable sample stage within the field of

the electromagnet and aligned precisely to reflect the incident beam directly onto the photodiode. An incident angle of 20 degrees (45 degree is appropriate in order to have maximum Kerr rotation and is limited due to the geometry of magnet) is used in order to get adequate Kerr rotation. A graphical user interface designed in LabVIEW was used to control the experiment.

Experimental parameters are defined through the LabVIEW user interface before beginning the measurement process. Upon program initiation, the magnetic field strength is incremented in steps; starting from a zero field, until reaching a user-defined peak. After reaching its maximum value, the magnetic field is stepped back to a zero field and then to an equal negative peak field. Lock-in amplifier assisted noise-free photodiode readings are taken in synchronization with the sweeping current (field) so that each current (field) has a corresponding diode reading. The maximum strength of the magnetic field is dependent on the saturation magnetization of the sample with a maximum possible value of 3500 mT. The step size in field strength is dependent on user specifications. The current value is plotted against the diode readings in order to visualize the results of each measurement. The current value could be replaced by corresponding field strength using the current field calibration data which is already defined. By plotting each individual point it is possible to observe and quantify the magnetic hysteresis of a given magnetic specimen. The instrumentation proved successful in providing reliable data consistent with prior results.

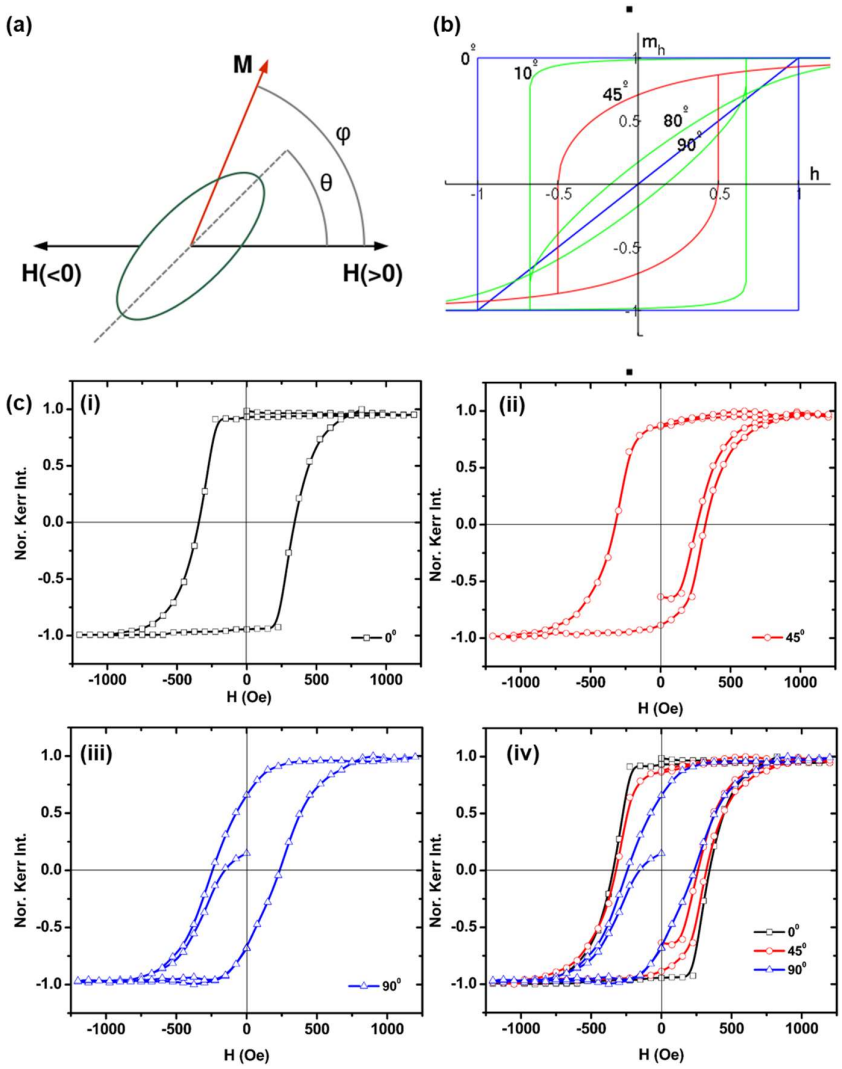

Figure 7.8 (a) Relationship between direction of applied field H, magnetization M, and easy axis (indicated by dashed line), ***(b)*** Hysteresis loop predicted by Stoner-Wohlfarth model for different ϕ values, ***(c)*** (i) – (iii) MOKE hysteresis plots of FeCo thin films measured using the fabricated MOKE setup, having a uniaxial anisotropy for three different ϕ values (0,45 and 90) and exhibiting behavior predicted by Stoner-Wohlfarth model, (iv) combined view of all the angles.

Thin films of FeCo were deposited on silicon substrates (1 cm x 1 cm) by thermal evaporation, using Fe and Co wire as the targets. The substrates

were cleaned with acetone, ethanol and trichloroethylene and were immediately loaded into the vacuum chamber. Film deposition was carried out at room temperature at a pressure of 2 x 10^{-5} mbar and current of 50A with a source to substrate distance of 15cm. Films with a thickness of 50 nm were deposited at incident angles 35^0. Deposited films were passivated by a thin layer of Au to avoid oxidation.

These thin-film samples are subjected to MOKE hysteresis measurement using our in-house fabricated MOKE magnetometer. These loops are compared with a standard FeCo loop. The correlation is excellent. Magnetic materials exhibit different hysteresis based on the direction in which the external field is applied. There exists an "easy axis" of magnetization along which all the moments of a ferromagnetic material prefers to align by itself. Here, in the as deposited FeCo thn film, there is an in plane uniaxial anisotropy due to the presence of crystalline cobalt. By analyzing samples in directions both parallel and perpendicular to the easy axis of magnetization we could confirm the effectiveness of our device using the Stoner-Wohlfarth model. The Stoner-Wohlfarth (SW) model, developed in 1948, describes the rotation of magnetization in single domain magnetic structures.[6] The SW model states that the energy associated with a single domain particle with magnetization $\boldsymbol{M}$, volume V, and magnetic anisotropy factor K in a magnetic field of strength H, is given by equation 7.6.

$$E = KV \sin 2\Theta - MVH \cos \phi - \Theta \qquad (7.6)$$

where ϕ is the angle between the applied field and the easy axis and Θ is the angle between the magnetization of the sample and the easy axis (see ***Figure 7.8a***).

The shape of the hysteresis loop depends on the orientation ϕ of the external field relative to the easy axis. The hysteresis loop is the magnetization component of the sample ***M*** plotted against the external field H.[7] The SW model predicts that when the applied field is parallel to the easy axis of magnetization (ϕ =0°) that the hysteresis loops will be a square, exhibiting an abrupt switch in alignment as the external field reaches the value of the coercive (or switching) field.

As ϕ is increased to 90° hysteresis will diminish and ***M*** will move gradually from one direction of magnetization to the other as its preferred direction of magnetization lies perpendicular to the applied field. ***Figure 7.8b*** denotes the hysteresis loops predicted by the SW model for values of ϕ between 0 and 90°. ***Figure 7.8c*** represents data collected from the FeCo sample. As can be clearly seen, experimental results agree with the Stoner-Wohlfarth model. As the sample was rotated from position (i) to position (iii) the square nature of the hysteresis loop diminished. The dependence of the hysteresis loop on ϕ provides confirmation that the device is suitable for accurately measuring the MOKE hysteresis with precision acceptable for the purposes intended.

7.5 Conclusion

Magnetic memory and other magnetic devices are at the forefront of today's advancing technological society. New developments in the field are largely dependent on synchrotron X-ray methods to enhance

understanding of atomic-scale interactions and structures. However, MOKE studies remain a useful tool for sample analysis due to its simplicity and relatively low cost. A device for measuring magnetic hysteresis of thin-films making use of magneto-optic Kerr effect was successfully fabricated at the Magnetics Laboratory, Cochin University of Science and Technology. The setup consists of advanced tools and techniques such as vibration-free table and lock-in detection for minimizing unwanted ambient vibrations and noise. The set-up is integrated with a cryostat for low temperature measurements. The device is completely automated for data collection using National Instruments LabVIEW GUI assisted by National Instruments cDAQ. The validity of the setup is confirmed by plotting hysteresis loop of a FeCo ferromagnetic thin films having a uniaxial anisotropy and comparing the same with standard Stoner-Wohlfarth behaviour. Fabrication and initial measurements of this device have been successful, encouraging further upgradation of the MOKE magnetometer for better sensitivity and imaging capabilities.

7.6 References

1. *The London, Edinburgh, and Dublin Philosophical Magazine and Journal of Science*, 1877, **3**, 321-343.
2. Z. Q. Qiu and S. D. Bader, *Review of Scientific Instruments*, 2000, **71**, 1243-1255.
3. É. d. T. de Lacheisserie, *Magnétisme*, Edp Sciences, 2012.
4. L. D. Landau, J. Bell, M. Kearsley, L. Pitaevskii, E. Lifshitz and J. Sykes, *Electrodynamics of Continuous Media*, Elsevier, 2013.
5. N. Instruments, 2017.
6. C. Tannous and J. Gieraltowski, *European Journal of Physics*, 2008, **29**, 475.
7. E. Della Torre, *Magnetic Hysteresis*, Wiley, 2000.

Chapter 8

Conclusion and Future Prospects

This chapter is on the conclusions drawn out of this study and also looks at some of the lacunae in the present investigation. The prospects for further studies are also dealt with in this chapter.

It is only natural that at the end of a long, tiring and laborious journey, one tends to reflect! Especially, on the path which lies ahead as far as this voyage is concerned and also on the lacunae that have been identified by the author – or in general terms 'what could have been done?' or 'what can be done?', to sustain momentum by someone else in the laboratory. It is mostly a stock-taking exercise and more importantly a self-criticism and also to make sure that some thoughts about future outlook with reference to this piece of investigation are also shared with. This is what is being presented in this chapter on 'Conclusion and Future Prospects'.

In hindsight, I feel that I was very fortunate to have trodden a path less trod by others. To quote Robert Frost,

> *"Two roads diverged in a wood, and I—*
> *I took the one less travelled by,*
> *And that has made all the difference."*

We were successful in opening up new trails in the jungle of research on 2D materials where others can create new trails for their successors. This journey too was replete with ups and downs, anxieties and uncertainties.

We too followed the trails cut opened by giants like Andre Geim and Konstantin Novoselov and were successful in realizing new and novel two-dimensional entities which are not layered in nature and at the same time easier to exfoliate by mechanical means. The very idea of focusing on non-layered oxides was that precursors were pure minerals and are well studied and understood. Hence the choice of material precursors is hematite and ilmenite for extracting 'hematene' and 'ilmenene' respectively. Hematite is a well-known pigment, a catalyst and an

electrode material for electrocatalysis while ilmenite is a primary ore of titanium and a starting material for the manufacture of titania (TiO_2) – a well-known photocatalyst and pigment.

The last decade witnessed a flurry of research activities in the area of 2D materials which has resulted in new paradigms namely 'beyond graphene' and van der Waals (vdW) solids. The emergence of vdW solids has given birth to a new area called valleytronics. The characteristic feature of vdW solids is that they are laterally linked together by covalent bonding within a plane while on the other plane they are bonded by van der Waals forces of attraction. Most of the existing devices are based on van der Waals solids which are layered. It is felt that the consequences of this investigation especially on non-layered 2D materials, namely hematene, ilmenene and 2D manganese telluride (MnTe) unlike 'beyond graphene' materials, are going to be groundbreaking as well as trailblazers.

The highpoint of this investigation is the successful exfoliation of three new 2D materials namely hematene, ilmenene and 2D MnTe for the first time. The characteristic feature is that they are non-layered and are exfoliated from their bulk counterparts though it was thought to be extremely difficult to achieve. We succeeded in isolating a 3 atom thick (~0.8 nm; 2 layers) 2D non-layered material 'hematene' from hematite. A plausible mechanism for exfoliation could be propounded according to which the highest broken-bond density and dipole moment along the c-axis induces an instability, effecting exfoliation of [001] hematene sheets. It is found that hematene sheets obtained are of a sub-nanometer thickness and in addition to [001] oriented hematene, another orientation [010] is

also observed experimentally. The stability of hematene was established by molecular dynamic simulations and it could be inferred that [001] oriented hematene planes are of lesser energy and hence energetically favourable. The stability of ilmenene, 2D analogue of ilmenite, is confirmed by employing phonon dispersion studies as well.

Contrary to the belief that magnetism could not exist in 2D, we proved beyond doubt that ferromagnetic ordering takes place in 2D systems such as hematene and ilmenene. These experimental findings were also substantiated by ab initio density functional theory (DFT) calculations. As far as practical applications are concerned, we demonstrated that both hematene and ilmenene are good photocatalytic materials when used as a sensitizer in a heterojunction along with titania nanotube array electrodes. Heterojunctions of titania with hematene and titania with ilmenene obtained an incident photon conversion efficiency (IPCE) of 12% and 8% with an IPCE integrated photocurrent of 0.93 mA/cm^2 and 0.48 mA/cm^2 respectively which are reasonably good numbers in their respective configurations. It was also possible to demonstrate that the heterojunction of ilmenene with titania produced hydrogen (H_2) and the evolved hydrogen was quantified.

Few layered 2D MnTe could be extracted successfully from semiconducting binary telluride of manganese having an antiferromagnetic ground state in pristine form. However, exfoliation of MnTe to its 2D form resulted in the total destruction of magnetic order and 2D MnTe became paramagnetic, unlike hematene and ilmenene. This unfolds yet another possibility of tuning magnetism at two-dimensions.

Magnetic vortices are spiral kind of entities formed on 2D magnetic nanostructures having a circular or rectangular geometry. Vortices have so many technological applications, especially in magnetic storage and spin wave generators. Understanding the dynamics of moments in a magnetic vortices is so important in order to tune them for technological applications. In an external magnetic field, a vortex state may switch to a single domain state and vice versa and the two states are separated by an energy barrier. So, at elevated temperatures, for a particular composition, a slight thermal fluctuation could enable the switching between vortex state and co-linear state resulting in lossless switching. The temperature at which lossless switching occurs is known as bifurcation temperature (T_e). Our investigations established the relationship between the concentrations of Fe (x) in Fe_xPd_{100-x} alloy and the bifurcation temperature of the vortices formed on 2D nanocaps of Fe_xPd_{100-x} alloy on closely packed polystyrene hemispheres.

Magneto-optic Kerr effect (MOKE) magnetometers have been effective magnetic characterization technique especially in probing surface magnetism of a local area which could be particularly useful in the case of magnetic thin films and 2D materials. MOKE measurements are performed by probing the change in polarization of the reflected laser beam against the applied magnetic field. Since the magnitude of change in polarization is directly proportional to the magnetization of reflecting surface, one can obtain the hysteresis loop of the specimen and thereby determining the loop characteristics like squareness and coercivity. Since the laser penetration depth is only up to 20 nm from the surface, MOKE set up could be sensitive even up to a monolayer of atoms which would

be really effective in probing magnetism in 2D materials. Such a MOKE set up is fabricated in-house by acquiring all the components and automating the entire set up using National Instruments LabVIEW package. Calibration and initial measurements have been successful and will be modified to improve the sensitivity for ultrathin samples.

From a physics point of view, though some fundamental calculations were performed by employing molecular dynamics, density functional theory (DFT) and phonon dispersion, they all remain supplementary in nature. This is one of the drawbacks of the study. A proper understanding of the preferential exposure of crystallographic planes could be carried out by extending similar studies using molecular dynamics, density functional theory (DFT) and phonon dispersion by taking the cue from lattice energy considerations. Such calculations along with surface studies using sophisticated techniques like low energy ion scattering (LEIS) could be a futuristic proposition. The advantage of using new generation LEIS spectrometers with imaging capabilities could come handy in observing the surface atoms on a particular plane. Such studies could impart credibility to the predictions by molecular dynamics, DFT and phonon dispersion studies.

Though evidence for ferromagnetic ordering has been obtained in this particular study, the representative data have been collected by using bulk characterization technique SQUID. More conclusive experiments needed to be carried out on these 2D materials to understand the 2D magnetism either by using scanning nitrogen vacancy magnetometer or by using the

already fabricated indigenous MOKE set up. Such investigations could not be carried out because of the scarcity of time.

In the literature, magnetism at two-dimension is ruled out theoretically by Mermin-Wagner theorem in which the destruction of magnetic ordering at very low temperatures is attributed to magnon excitations. Contrary to this belief, we observed magnetic ordering in the case of hematene and ilmenene and this phenomena warrant a thorough investigation, especially, with respect to magnon excitations if any, at two-dimensions. It will be worthwhile to undertake a detailed study on the behaviour of magnons at low temperatures in these 2D non-layered structures. This is going to be a new area which will enrich the existing knowledge on 2D magnetism.

Though considerable improvement in the photocatalytic activity of the hematene and ilmenene could be achieved, this was all based on heterojunction with titania nanotubes. Scope exists to employ these materials as standalone electrodes for water splitting applications. This is an unfinished task and could be carried out later by the incoming PhD students. Pure iron oxides are good gas sensors and hence the validity of hematene, having a huge surface area, as a potential gas sensor could also need to be established. This is also an unfinished task. Similarly, both hematene and ilmenene could serve as pigments with improved optical characteristics. This is yet another area which can be explored.

The method of liquid exfoliation is low yielding, laborious and time-consuming. Sophisticated techniques are required for depositing them in the form of thin-films. Chemical vapour deposition (CVD) will be

advantageous for depositing high-quality hematene and ilmenene on suitable substrates and could be ideal to fabricate devices and also for studies in 2D magnetism using scanning nitrogen vacancy magnetometer or MOKE.

As far as studies on magnetic vortices are concerned, stable vortices could be created by using various available soft magnetic alloys such as FePt and FeNi to extend the validity of the variation of bifurcation temperature (Te) with the composition to other materials as well. Time-resolved magneto-optic Kerr effect (MOKE) measurements are essential to unfold more details about the hysteresis-free switching and is one of the future propositions of our investigations on magnetic vortices.

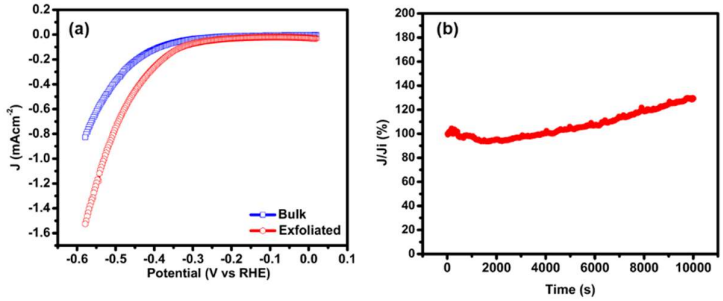

Figure 8.1. (a) LSV of bulk and 2D MnTe on drop dried on glassy carbon electrode - showing the decrease in onset potential with enhanced current density, and ***(b)*** Chronoamperometric study of 2D MnTe on glassy carbon showing stability over a large time period.

Another study which could not be completed because of lack of time is the study on electrocatalytic activity of these exfoliated non-layered 2D materials. However, some initial results of MnTe as a promising electrocatalyst are presented in ***Figure 8.1***. This studies could be pursued as a continuation of the present work.

The indigenously developed MOKE set up could be upgraded to an imaging MOKE. Moreover, the MOKE set up could be modified by using a stabilized laser and high-quality polarizers such that the sensitivity of the equipment can be improved and is sufficient enough to measure the magnetism of monolayers of 2D materials. The same set up could be employed for measuring Faraday rotation, dichroism and birefringence of fluid and thin film samples.

Hence the future perspectives of the present investigations can be summarized as follows-:

1. Chemical vapour deposition of non-layered 2D materials for device applications.
2. Understanding the basic physics underlying the magnetism in hematene and ilmenene.
3. Photocatalytic activity of standalone electrodes of hematene and ilmenene.
4. Exfoliation of new non-layered materials with energetically favourable planes/directions of exposure/cleavage.
5. Hematene as a pigment material
6. Suitable methods for large scale synthesis of 2D non-layered materials.
7. Electrocatalytic activity of hematene, ilmenene and 2D MnTe.
8. Vortex bifurcation temperature of various alloys.
9. Improving the sensitivity of MOKE and updating the system with imaging capabilities.

Having discussed the lacunae in the present study and having brought out possible futuristic propositions as a continuation of this particular investigation, I conclude this thesis on a philosophical note.

The journey leading to PhD is often riddled with uncertainties and unexpected U-turns. It is in this context that I am reminded of one of the road signs "In a journey, you expect the unexpected". During my journey too, I have come across such unexpected U-turns. As in any journey, there were excitements and boredom, depressions and distractions, conflicts and collaborations, patience and impatience. On one hand, the patience to wait for the results, sometimes, superseded the impatience to know the new. Alongside, I also learnt what to discard and what not to throw away. This journey also taught me the value of grit and resilience. It is said that 'travel broadens one's horizon', and in my case too this has been true as it broadened my knowledge and I learnt a lot on materials physics.

No journey is complete and to quote Robert Frost:

"The woods are lovely, dark and deep,
But I have promises to keep,
And miles to go before I sleep,
And miles to go before I sleep."

I conclude my thesis with this poem with the fond belief that this journey will be the beginning of another journey where I presume the future is bright.

"Whatever happened, happened for the good. Whatever is happening, is happening for the good. Whatever will happen, will also happen for the good."

~ Bhagavat Gita